Master's thesis

2020

Dirk Willem van Binsbergen

NTNU
Norwegian University of
Science and Technology
Faculty of Engineering
Department of Marine Technology

Dirk Willem van Binsbergen

Effects of Induction and Wake Steering Control on Drivetrain Fatigue and Wind Farm Power Production

July 2020

NTNU
Norwegian University of
Science and Technology

NTNU
Norwegian University of
Science and Technology

NTNU

Norwegian University of
Science and Technology

Effects of Induction and Wake Steering Control on Drivetrain Fatigue and Wind Farm Power Production

Dirk Willem van Binsbergen

European Wind Energy Master
Submission date: July 2020
Supervisor: A. R. Nejad
Co-supervisor: S. J. Watson, P. van der Male

Norwegian University of Science and Technology
Department of Marine Technology

MASTER OF SCIENCE THESIS

EFFECTS OF INDUCTION AND WAKE STEERING CONTROL ON DRIVETRAIN FATIGUE AND WIND FARM POWER PRODUCTION

by

Diederik van Binsbergen BSc

In partial fulfillment of the requirements for the degrees of

Master of Science

Technology - Wind Energy

NTNU

Department of Marine Technology

Master of Science

Offshore Engineering

TU Delft

Faculty of 3mE

June 28, 2020

Student number:

517528 4380126

Supervisor:

A.R. Nejad

S.J. Watson
P. van der Male

Thesis Committee:

A.R. Nejad
Z. Gao

S.J. Watson
P. van der Male

An electronic version of this thesis is available at http://repository.tudelft.nl/

Preface

For the last half year, in a time where lots of unpredictable events happened, I worked on the thesis finalizing the graduation process for obtaining a master's degree in Offshore Engineering from Delft University of Technology and a master's in Technology - Wind Energy from the Norwegian University of Science and Technology as part of the European Wind Energy program. For this thesis I would like to thank Irena Rivera, Adrian Yague and Adam Wise for helping me with the OpenFAST and FAST.Farm software and I would like to thank Jason Jonkman for providing me with an early version of FAST.Farm. I would like to thank Erin Bachynski and Adam Wise for providing me with useful data regarding the OpenFAST and FAST.Farm models.

I would like to thank both Shuai Wang and Amir Nejad for giving me an opportunity to release a paper for the Torque conference. Further more I would like to thank Shuai for providing me results of his model which I could use in my thesis and I would like to thank Shuai for his general support during the whole master thesis. I would like to thank Amir for providing me this thesis opportunity, helping me develop the beginning of the methodology, being there to discuss results and always radiating lots of positivity. Further more the input of Simon Watson and Pim van der Male was very much appreciated, providing important structured criticism, which helped me significantly increase the quality of the thesis.

I would like to thank my roommates at NTNU, especially Maarten van der Drift, for the great time I had in the beginning of the semester and I would like to thank Jiao Harmsen for making the corona time a lot more enjoyable.

I would like to thank Maaike Sickler for the continuous support during the last six months of thesis work.

Finally, I would like to thank fellow students I met during my time at DTU, TU Delft and NTNU during the last two years of my master's for being part of my life and maybe most important I would like to thank my close friends and family in the Netherlands for being there for me when it was needed.

Diederik van Binsbergen
Ochten, July 2020

Abstract

Power optimization through wake steering and axial induction control is a well investigated topic in wind energy, which is generally proven to work. The influence of control manoeuvres on the fatigue of static components is generally discussed, but drivetrain fatigue due to wake steering and axial induction control is rarely discussed, while it is known that the drivetrain is a highly vulnerable part of the wind turbine and its downtime can result in a significant increase in cost.

Having a better understanding of turbine wake interaction and wind farm power optimization and its influence on drivetrain dynamic behaviour serves as a reference for future wind farm cost optimization and predictive maintenance. The main research question answered in the thesis is as follows:

To what extent does wind farm power optimization increase profit when wind farm power production and drivetrain bearing fatigue damage is considered?

With the following sub-questions being answered:

To what extent does power production change for different wind farm power optimization manoeuvres?

What is the influence of wind farm power optimization on local drivetrain damage of the considered wind turbines?

Multiple test cases for wake steering and axial induction control are considered, where different yaw angles, γ, and blade pitch angles, β, are chosen for the upwind turbine. For each test case, power production and bearing damage is studied. A cost estimation is made and for a range of energy prices the most profitable test case is found. For verification, a two and four wind turbine case in an uniform wind field is considered. Power production results for this low turbulent case are studied and compared to literature.

Turbulent wind field results show that both wake steering and induction control result in a limited power production increase of 0.78% for $\gamma = 7^\circ$ and 0.17% for $\beta = 1^\circ$. The power production increase for the two and four wind turbine case in the uniform wind field for wake steering and induction control are 4.78% for $\gamma = 15^\circ$, 16.6% for $\gamma = 20^\circ$, 0.19% for $\beta = 1^\circ$ and 10.3% for $\beta = 3^\circ$ respectively.

Overall bearing damage of WT_1 and WT_2 increases with increased yaw angles for WT_1 and the overall bearing damage of WT_1 and WT_2 decreases with increased blade pitch angles for WT_1. INP-A and PLC-B bearing damage significantly increases for the downwind turbine.

In the high turbulent wind field ($TI = 0.2$), when considering two wind turbines, wake steering can result in a profit increase ranging from -€3,70 to €4,-, while axial induction control can result in a profit increase ranging from €3,- to €40,-. In the low turbulent wind field ($TI = 0$), when considering four wind turbines, the power production increase for wake steering can result in a profit increase ranging from €30,- to €130,-, while axial induction control can result in a profit increase ranging from €15,- to €60,-.

Both wake steering and axial induction control can result in increased profit. The desired control manoeuvre is highly dependent on the ambient wind, wake overlap of the downwind turbine and the wind farm arrangement.

Contents

List of Abbreviations

3D	3 Dimensional
ABL	Atmospheric Boundary Layer
AL-LES	Actuator Line Large Eddy Simulation
AWAE	Ambient Wind and Array Effects
BP	Blade pitch
CFD	Computational Fluid Dynamics
DWM	Dynamic Wake Meandering
EOM	Equations Of Motion
FAST	Fatigue, Aerodynamics, Structures and Turbulence
FEM	Finite Element Method
FFT	fast Fourier Transform
FSV	Field Support Vessel
FWT	Floating Wind Turbine
GB	Great Britain
HAWT	Horizontal Axis Wind Turbine
HLV	Heavy Lifting Vessel
HSS	High speed shaft
ISS	Intermediate speed shaft
JONSWAP	Joint North Sea Wave Observation Project
LCOE	Levelized Cost Of Energy
LDD	Load Duration Distribution
LSS	Low speed shaft
MBS	Multibody Simulation
MoorDyn	MooringDynamics
NREL	National Renewable Energy Laboratory
OM	Operation Maintenance

OF	OpenFAST
PM	Palmgren-Miner
PM	Pierson-Moskowitz
R&D	Research &Development
RPM	Rotations per minute
SC	Super Controller
SOWFA	Simulator fOr Wind Farm Applications
SWL	Still water level
TI	Turbulence Intensity
TLP	Tension Leg Platform
TSR	Tip speed ratio
VM	Vortex Method
VTK	Visualisation Toolkit
WD	Wake-Dynamics
WT	Wind Turbine

Nomenclature

α	Power law exponent [-]
β	Blade pitch angle [$^\circ$]
γ	Yaw misalignment angle [rad]
$\hat{\eta}(\omega)$	Fourier coefficient [-]
$\hat{\mathbf{X}}(\omega)$	Wave diffraction forces [N]
λ	Tip speed ratio [-]
$\mathbf{A}(\omega)$	Hydrodynamic added mass matrix [kg]
$\mathbf{B}(\omega)$	Radiation damping matrix [kgs^{-1}]
$\mathbf{C}_{hst}$	Hydrostatic restoring matrix [Nm^{-1}]
$\mathbf{M}$	Inertia matrix [kg]
ω	Angular velocity [rad s^{-1}]
ω_i	Rotational speed of the gear in bin i [rpm]
ω_{hs}	High speed shaft angular velocity [rads$^-$1]
ω_{ls}	Low speed shaft angular velocity [rads$^-$1]
ρ	air density [$\frac{kg}{m^3}$]

σ_1	Standard deviation of the main wind speed [ms^{-1}]
σ_u	Standard deviation of the main wind speed [ms^{-1}]
τ	Torque [Nm]
A	Cross-sectional Area [m^2]
A	Rotor blade area [m^2]
a	Axial interference coefficient [-]
a	Bearing constant [-]
a_n	Axial interference coefficient [-]
C	Basic load rating [N]
C_P	Power coefficient [-]
D	Outer diameter [m]
d	Inner diameter [m]
dU/dZ	Wind shear [s^{-1}]
F_a	Axial load [N]
F_r	Radial load [N]
f_{grid}	Grid frequency [Hz]
I	Second Moment of Area [m^4]
I_{ref}	Reference turbulence intensity [-]
K	Torsional Stiffness constant [m^4]
L	Bearing life [s]
L_{10}	Characteristic basic rating life [s]
m	Mass [kgm^{-1}]
n	Angular velocity [rpm]
N_i	Total amount of cycles causing failure for stress range σ_i [-]
n_i	Number of cycles in bin i[-]
n_i	Number of cycles that occur for a stress range σ_i [-]
n_p	Number of poles [-]
P	Dynamic equivalent radial load [N]
P	Power [W]
R	Rotor radius [m]
r_g	Radius of Gyration [m]
t_i	Time duration of bin i [s]
T_{hs}	High speed shaft torque [Nm]

T_{ls}	Low speed shaft torque [Nm]
TI	Turbulence intensity [-]
U	Main wind speed [ms^{-1}]
u_*	Surface friction [-]
u_∞	Ambient wind field [ms^{-1}]
V	Wind speed [ms^{-1}]
V_{hub}	Main wind speed [ms^{-1}]
V_{ref}	Reference wind speed [ms^{-1}]
X	constant from ISO 281 [-]
Y	constant from ISO 281 [-]
z_0	roughness length [m]
z_r	Reference height [m]
$\alpha\varepsilon^{\frac{2}{3}}$	Energy dissipationrate
α	3D Kolmogorov constant [-]
ε	Viscous dissipation rate
Γ	Shear parameter quantifying anisotropy [-]
γ	Yaw angle [$^\circ$]
a	Axial induction factor [-]
$a_t^{'}$	Tangential induction factor [-]
C_T	Thrust coefficient [-]
dt	Time step [s]
du	step size in U direction [m]
dv	step size in V direction [m]
dw	step size in W direction [m]
H_s	Significant wave height [m]
L	Length scale of the spectral velocity tensor [m]
n_u	number of steps in U direction [-]
n_v	number of steps in V direction [-]
n_w	number of steps in W direction [-]
T	Thrust [N]
T_p	Peak spectral period [s]
T_z	Zero up-crossing period [s]
t_{sim}	Simulation time [s]

u_{mid}	Mid grid wind speed [ms^{-1}]
X	Grid length in X direction [m]
Y	Grid length in Y direction [m]
Z	Grid length in Z direction [m]
z	Grid height [m]
z_{mid}	Mid grid height [m]
D	Total accumulated damage [-]

List of Figures

List of Tables

1 | Introduction

Wind energy has been used by humans for different purposes for centuries. It was mainly used to propel boats, grind grain or pump water [1]. Nowadays wind energy is mainly used to produce electrical energy to support the electrical grid. The first known wind turbine (WT) was built in 1887 and was made to produce energy in Scotland. Eventually many turbines followed aiming to produce more energy per turbine resulting in larger multi-MW turbines. Companies saw the potential to power the grid through wind energy which resulted in the first offshore wind turbines in Denmark [2]. Multiple wind turbines were placed close together due to the large amount of space offshore creating the first wind farms.

The main driver behind most research and development (R&D) for wind turbines and wind farms is the levelized cost of energy (LCOE), which is given as the sum of costs over lifetime divided by the sum of electrical energy produced over lifetime. The LCOE has significantly decreased over time, which can be seen in Figure 1.1. The major drivers that contribute in a reduction of LCOE are innovations in wind turbine technology, installation and logistics and economy of scale; improved wind resource due to higher hub heights and increased power production due to larger rotor diameters [3], which can be seen in Figure 1.2.

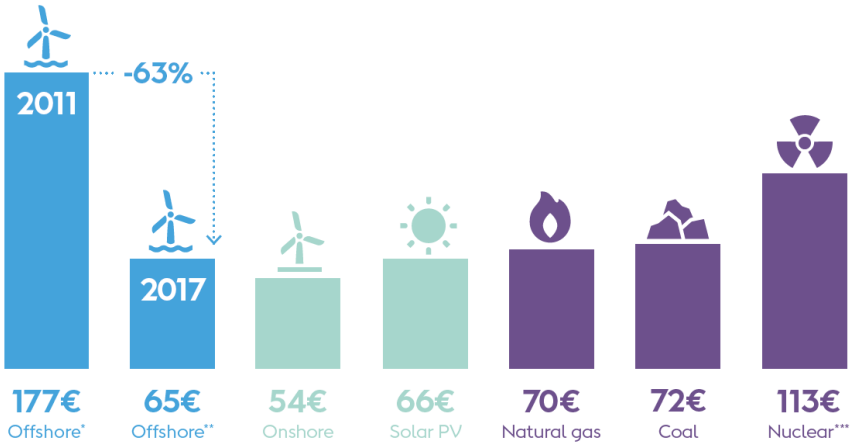

Figure 1.1: Cost of offshore wind energy compared with other sources (EUR per MWh, 2016 prices) [4].

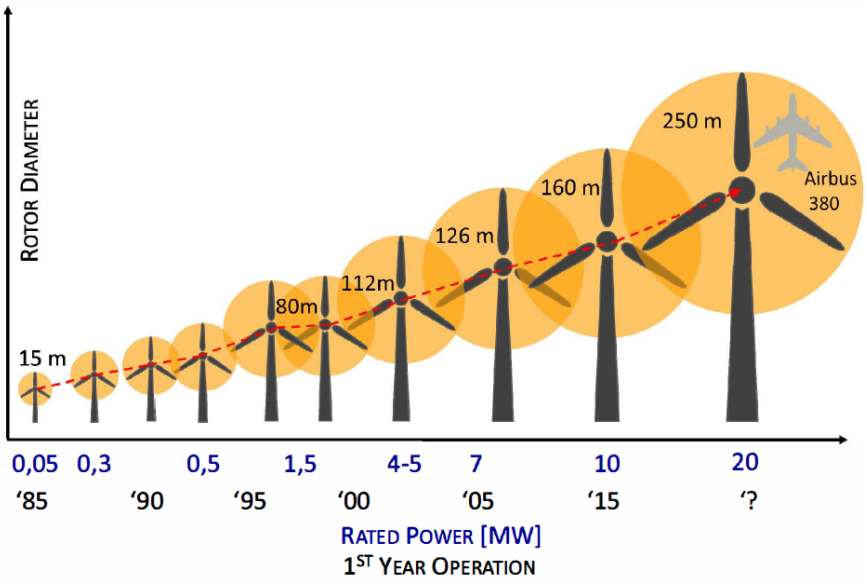

Figure 1.2: Increment of WT rated power and blade radius [5].

Due to increased wind farm size and the increased amount of wind farms world wide, research regarding wind farm control has received a great deal of attention. Wind turbine wakes, characterized by a velocity deficit and added turbulence, could significantly affect the total power output and fatigue life of turbines within a wind farm. More specifically, the velocity deficit behind the upstream turbine results in a power loss of downstream turbines, whereas the added turbulence causes the increase in structural loads of downstream turbines leading to the increase in fatigue damage [6].

1.1 Problem Statement

Many studies have been conducted to investigate the dynamic behaviour of wakes or wake effects on wind turbines and many studies have been carried out on wind farm control: Total farm power output can be optimized through wake steering control [7, 8, 9, 10, 11, 12, 13, 14, 15, 16], axial induction control [9, 14, 17, 18, 19, 20, 21, 22, 23, 24, 25, 26] or a combination of both [27] and is generally proven to work.

The resulting influence of fatigue on static components has been discussed [28, 29, 30, 31, 32, 33, 34], but drivetrain fatigue damage due to wake steering or axial induction control is rarely discussed [30]. Especially the amount of studies that have been conducted on the load effect analysis of the drivetrains in wind farms is limited, while it is known that the drivetrain is one of the most vulnerable parts of the wind turbine and its downtime can result in increased cost [35]. Being able to reduce the drivetrain loads and increasing the working life while maintaining optimal power production will result in a reduction of LCOE for wind turbines in a wind farm setup.

1.2 Research Objective

From the problem statement a main research objective can be defined:

To create and apply a methodology to determine hourly profit taking into account wind farm power production and drivetrain bearing damage.

1.3 Research Questions

From the problem statement and the research objective the main research question can be derived, which is formulated as follows:

To what extent does wind farm power optimization increase profit when wind farm power production and drivetrain bearing fatigue damage is considered?

In addition to the main research question, a set of sub-questions is formulated which help to support the main research question.

- *What is the influence of wind farm power optimization on the global loads of the considered wind turbines?*
- *What is the influence of wind farm power optimization on local drivetrain damage of the considered wind turbines?*
- *To what extent does power production change for different wind farm power optimization manoeuvres?*
- *To what extent does the turbulence intensity influence the applicability of wind farm power optimization?*
- *How does wind farm size influence the power optimization results?*
- *To what extent are results applicable for different sea states?*
- *How can drivetrain fatigue damage be correlated to decrease in profit?*
- *To what extent are results found for floating substructures also applicable for bottom-founded structures?*

1.4 State of the Art

First, a literature review is carried out to :

- Create a methodology to determine wind farm power production, wind turbine drivetrain fatigue damage and give an overall cost estimation for different wake steering and axial induction test cases.
- Find the state of the art literature regarding wake steering and axial induction control.
- Find the state of the art literature regarding wind turbine drivetrains and dynamic fatigue.
- Find useful modeling tools on wind farm level, able to calculate power production and global loads.
- Find useful modeling tools for wind turbine drivetrains.
- Find literature to estimate power production profit and cost of failure.

The state of the art research is discussed below and will serve as starting point for the master thesis work regarding relevant models and relevant theory. The resulting methodology is discussed in chapter 3.

1.4.1 Axial induction and Wake Steering Control

As stated in the beginning of chapter 1, wind turbine wakes have added turbulence and a velocity deficit which causes increased fatigue loads [36] and decreased power production of downwind turbines [37]. Literature suggests that by steering the wake into a certain direction by yawing the upwind turbines or by changing the upwind blade pitch angle an increase in power output can be found [7]-[27].

1.4.2 Modeling Tools

Modeling tools should be selected that are able to calculate the loads and motions on the wind turbine and drivetrain while taking into account the wind farm dynamics. The wind turbine and wind farm model could be considered in a decoupled manner from the drivetrain model.

Multiple simulation tools are available on wind farm level. The National Renewable Energy Laboratory ,NREL, provides tools like SOWFA and FAST.Farm [38, 39]. SOWFA is a high-fidelity simulation tool especially useful for farm applications where the fluid physics are calculated using computational fluid dynamics (CFD) and FAST.Farm is a mid-fidelity simulation tool able to connect individual OpenFAST [40] modules, which solve the aero-hydro-servo-elastic dynamics of distinct turbines, and also considers the ambient wind physics on wind farm level by using the dynamic wake meandering model [41].

IEC61400-1(2005) [42] states that either the Kaimal [43] or Mann [44, 45] turbulence model could be used as turbulent wind field.

A high-fidelity drivetrain model is developed by NTNU [46, 47]. This model is established using SIMPACK [48], a general multibody simulation software (MBS) able to calculate loads and load variations on flexible (using the finite element method (FEM)) and rigid bodies.

1.4.3 Dynamic Component Fatigue

Damage calculations differ for static and dynamic components. Damage on static components, like the wind turbine tower, is usually calculated using the rainflow counting algorithm [34], the SN-curve [49] and the Palmgren-Miner (PM) rule [50, 51]. Damage on dynamic components, like bearings and gears, is calculated using the Load Duration Distribution (LDD) method [52] which creates damage bins. these bins are then summed by using the palmgren miner rule, similar to static component damage.

The bearing axial and radial force time series are determined by the drivetrain model and are used to determine the dynamic equivalent radial load, which is then used with the Lundberg-Palmgren formulation to determine the total lifetime.

1.5 General Approach

The aim is to create and apply a methodology to determine hourly profit taking into account wind farm power production and drivetrain bearing damage. The methodology is applied on the two turbine wind farm case in turbulent wind. For the four wind turbine case in an uniform wind field the profit due to increased power production is found.

A relevant farm layout is created for wake steering, which is done by changing the yaw angle of the upwind turbine, and axial induction, which is done by changing the blade pitch angle of the upwind turbine. For both wake steering and axial induction different test cases and turbine arrangements are considered based on literature found [7, 14, 53].

The turbine considered is the DTU 10MW turbine [53, 54] supported by the nautilus floater [55, 56]. An ambient wind speed of 8 m/s is used with a representative sea state and the Mann turbulence model is used as turbulence model. Power production results are compared to power production results in a steady wind field of 8 m/s, which are also compared to literature mentioned in section 1.1. Due to limited available floater literature, floater results are compared to a fixed turbine set-up, where the floater is assumed to be fixed.

Global responses, consisting of the rotor thrust, rotor torque and yaw bearing overturning moment, obtained from FAST.Farm are analyzed and used as input for the 10MW wind turbine drivetrain model created using SIMPACK resulting in responses in X, Y and Z direction on main bearings of the low, intermediate and high speed shaft. These responses are analysed and the Lundberg-Palmgren formulation and the LDD method combined with the PM rule are used to find the total damage on the main bearings. For the two turbine case a methodology is created to determine cost of drivetrain failure and is combined with the profit made by power production to determine whether wake steering and axial induction is desirable and profitable.

1.5.1 Variables

The yaw angle, γ and the blade pitch angle, β are altered to change wind farm power production. The blade pitch angle will result in a different axial induction factor, a, while a yaw missalignment will steer the wake in a direction different than the ambient wind direction. The turbulence intensity, TI, will be chosen based on IEC-standards and is compared to non-turbulent simulation cases with the same values for γ and β.

For the profit calculations the price of energy is a highly variable parameter, thus the profit is determined for a range of energy prices.

1.5.2 Restrictions

The wind farm super-controller is not fully functioning yet in FAST.Farm. Thus the yaw and blade pitch angles are determined from literature and iteration.

FAST.Farm is not as accurate as SOWFA, but since FAST.Farm is significantly faster than SOWFA, FAST.Farm is used to calculate wind farm power production and wind turbine global loads.

The 10MW drivetrain model is based on real bearings and gears. The INP-A bearing of the model does not reach the desired criteria yet, but since no other bearing is available that does meet these criteria, the most suitable bearing is used.

Gear and shaft damage is not taken into account in the present work due to limited time. Further more the most relevant bearings are chosen, instead of choosing each available bearing in the drivetrain.

Limited knowledge is available on downtime due to drivetrain failure. Especially for large offshore floating wind turbines. When creating the profit methodology, assump-

tions regarding downtime, cost of downtime and cost of failure are made based on literature found for smaller bottom-founded wind turbines.

For the profit calculation only profit due to power production and decrease in profit due to bearing fatigue damage is considered, not taking into account fatigue damage of other components of the wind turbines.

2 | Theoretical Background

In the following Chapter the theoretical background behind the used models and methodologies created is explained. The created methodology is covered further in chapter 3.

First, turbulence theory and turbulence models are discussed in section 2.1 and 2.2. In section 2.3 theory on sea states is explained and in section 2.4 and 2.5 wake theory and the FAST.Farm wake model is explained.

In section 2.6, 2.7, 2.8 and 2.9 general power production, power production in steady yaw and wake steering and axial induction control for increased power production is discussed.

In section 2.10 a wind turbine is chosen, which model is explained in section 2.11.

Drivetrain theory is explained in section 2.12 and the drivetrain model is discussed in section 2.13. In section 2.14 downtime due to failure of the drivetrain is discussed and in section 2.15 drivetrain repair options are considered.

Section 2.16 discusses the fatigue theory and models used to determine drivetrain component damage.

In section 2.17 the price of energy and the wind farm power calculation to find the farm profit is noted.

Finally, model verification and model validation are discussed in section 2.18 and 2.19.

2.1 Turbulence Theory

To be able to efficiently produce energy from wind, one should first be able to understand the wind characteristics. A wind turbine is positioned in the atmospheric boundary layer (ABL). The wind in the ABL tends to be dominated by turbulent structures generated through the transfer of momentum and heat with the Earth's surface, as well as interaction with the free atmosphere above governed by large-scale motion [57] and friction with the earths surface. This turbulence is characterized by chaotic changes in pressure and flow velocity [58]. These changes in flow velocity cause significant fatigue damage to the wind turbine. Modeling and quantifying the atmospheric turbulence the right way is thus of significant importance for credible results.

The wind vector, $\mathbf{V}$, is composed of 3 components: $\tilde{u}$, $\tilde{v}$ and $\tilde{w}$. One can consider wind to consist of a mean wind speed, U, with superimposed turbulent fluctuations, u, v and w, having a mean value of zero, which is usually averaged over ten minutes [59]. The mathematical expression can be seen below in Equation 2.1. The ten minute averaging period is routinely used in wind energy. These periods mainly depend on the integral time scale which measures the the correlation distance over time or distance [60].

$$\begin{aligned} \tilde{u}(x,y,z,t) &= U(z) + u(x,y,z,t) \\ \tilde{v}(x,y,z,t) &= v(x,y,z,t) \\ \tilde{w}(x,y,z,t) &= w(x,y,z,t) \end{aligned} \tag{2.1}$$

Turbulence is usually quantified by using the turbulence intensity (TI). It is defined as the standard deviation divided by the main wind speed U, which represents the intensity of wind velocity fluctuation [61] and can be seen in Equation 2.2. The TI is highly related to the wind shear profile and the boundary layer stability and has a significant influence on wake restoring and ambient wind mixing. A value for the TI can be calculated using IEC-61400-1 (2005) [42].

$$TI = \frac{\sigma_u}{U} \tag{2.2}$$

Where

- σ_u is the standard deviation of the wind fluctuations in the main wind direction in $\frac{m}{s}$ also defined as σ_1 in IEC61400-1(2005).
- U is the main wind speed in $\frac{m}{s}$, also defined as V_{hub} in IEC61400-1(2005).

A turbine class can be chosen dependent on the turbulence characteristics of the area where it is supposed to be placed.

Wind turbine class		I	II	III	S
V_{ref}	(m/s)	50	42,5	37,5	Values
A	I_{ref} (-)	0,16			specified
B	I_{ref} (-)	0,14			by the
C	I_{ref} (-)	0,12			designer

Figure 2.1: Reference wind speed and reference turbulence intensity for wind turbine classes [42].

The resulting parameter I_{ref} is the expected value of the turbulence intensity at a wind speed of 15 m/s. To calculate the TI at different wind speeds, Equation 2.3 can be used to calculate the standard deviation of the wind speed. By then using Equation 2.2, the TI at a specified wind speed can be found and used.

$$\sigma_1 = I_{\text{ref}}\,(0.75 V_{\text{hub}} + b)\,; \quad b = 5{,}6\text{m/s} \tag{2.3}$$

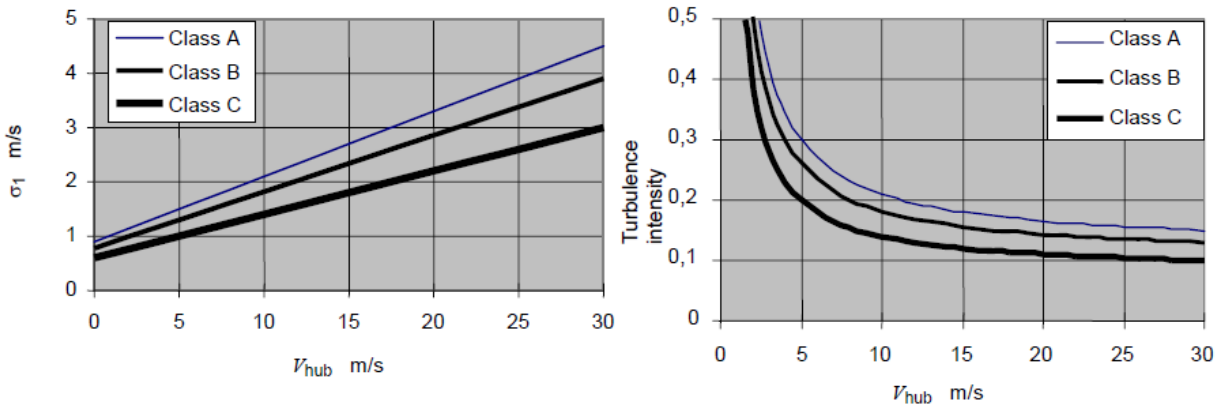

Figure 2.2: Turbulence intensity for different IEC classes: IEC class A, B and C [42].

3 turbulence models are stated in IEC61400-1(2005):

- Von Karman turbulence model [62]
- Kaimal turbulence model [43]
- Mann turbulence model [44, 45]

Each turbulence model has its own applications. The von Karman spectrum gives a good description for turbulence in wind tunnels [63], while the Kaimal spectrum may give a better fit to empirical observations of atmospheric turbulence. Both these turbulence models utilize a 1D fast Fourier transform (FFT) where each component, u, v and w is created separately. The Mann Turbulence Model uses a 3D FFT to create all components simultaneously [59] and is, together with the Kaimal spectrum, recommended by IEC61400-1(2005) [42]. The modeling procedure will be further elaborated in section 2.2.

As already stated, the ABL has a significant influence on the turbulence characteristics of the ambient wind field. It is thus important to model the ABL properly.

The shear profile of the ABL is dependent on the terrain. An example of different wind shear profiles can be seen in Figure 2.3. Two ways to calculate the ABL velocity profile are the Power Law in Equation 2.4 and the Log Law in Equation 2.5. The parameter that takes the terrain properties into account is either the power law exponent, α, in the Power Law Equation or the roughness length, z_0, in the Log Law Equation. Both have its advantages and disadvantages and are both used in different circumstances.

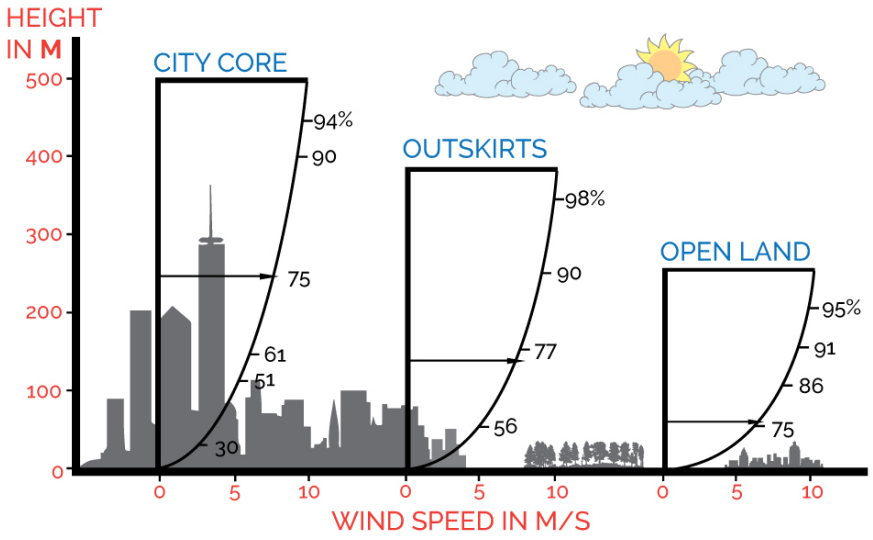

Figure 2.3: Wind shear profile of areas with a different roughness length. [1]

$$V(z) = V_{\text{ref}} \ln\left(\frac{z}{z_0}\right) / \ln\left(\frac{z_r}{z_0}\right) \tag{2.4}$$

$$V(z) = V_{\text{ref}} \left(\frac{z}{z_r}\right)^{\alpha} \tag{2.5}$$

Where

[1] https://sinovoltaics.com/learning-center/basics/location-factor-for-wind-and-solar/ [Visited on the 11th of January 2020]

- V_{ref} is the reference wind speed in $\frac{m}{s}$.
- z_r is the reference height in m.
- z_0 is the roughness length in m.
- α is the power law exponent.
- z is the height in m.
- $V(z)$ is the wind speed in $\frac{m}{s}$ related to the height z.

2.2 Turbulence Model

An uniform ambient wind field, which is defined as a wind field that does not vary over space, can be generated using the InflowWind module of FAST.Farm. A turbulent wind field, however, can not be created using the InflowWind modulde of FAST.Farm and should be created in advance.

Due to the recommendation stated in IEC61400-1(2005) [42], page 25, The Mann turbulence model will be used and described. The Mann turbulence model can be created by using a turbulence generator or by using WAsP Engineering [64]. A turbulence generator that can be used is the pre-processor tool which is part of HAWC2, an aeroelastic code intended for calculating wind turbine response in time domain [65]. TurbSim [66] by NREL is capable of creating a Kaimal turbulence model, but will not be used. Each of these models create their own synthetic turbulent wind data.

The interface of the Mann Turbulence generator can be seen in Figure 2.4.

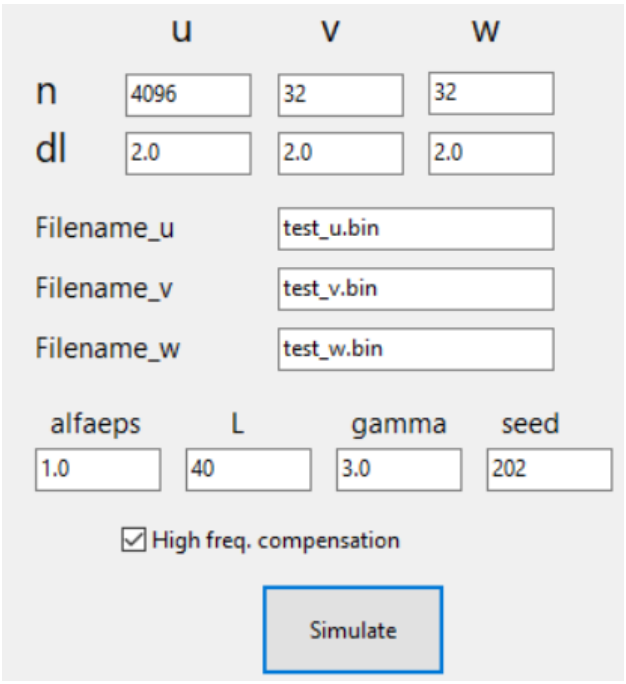

Figure 2.4: Interface of the Mann Turbulence generator. [2]

[2] http://www.hawc2.dk/Download/Pre-processing-tools/Mann-64bit-turbulence-generator [Downloaded on the 15th of January 2020]

IEC-61400-1(2005) [42] gives the following equations and values for the parameters, L and Γ. σ_{iso} can be calculated using σ_1 from Equation 2.3. Further more values for dv and dw are chosen with guidance from the Wind Energy Handbook [59]. Dependent on the wind field size the number of points in v and w direction can be found under the condition that the number is in the form of 2^n, where n should be an integer. the value for du is calculated using Equation 2.7. the number of points in u direction, nu, can be calculated using Equation 2.8. $\alpha\varepsilon^{\frac{2}{3}}$, also shown as alfaeps in Figure 2.4, is calculated using Equation 2.9. $\alpha\varepsilon^{\frac{2}{3}}$ is a measure of the energy dissipation, where ε is the rate of viscous dissipation of turbulent kinetic energy and α is the three-dimensional Kolmogorov constant equal to 1.7. L is the length scale of the spectral velocity tensor and Γ is the shear parameter that quantifies the anisotropy of the spectral tensor [67]. A seed is a pseudorandom number and thus any value can be chosen. Having all data needed for the simulation, a last check can be done to see whether the simulation has the right size. This can be done using Equation 2.10.

$$\begin{aligned} \Gamma &= 3,9 \\ \sigma_{iso} &= 0,55\sigma_1 \\ L &= 0,8\Lambda_1 \end{aligned} \tag{2.6}$$

$$\begin{aligned} z_{mid} &= \frac{z}{2} \\ u_{mid} &= u_{hub}\left(\frac{z_{mid}}{z_{hub}}\right)^{\alpha} \\ du &= u_{mid}dt \end{aligned} \tag{2.7}$$

$$n_u = u_{mid}t_{sim} \tag{2.8}$$

$$\alpha\varepsilon^{\frac{2}{3}} = \frac{55}{18}0.4754\sigma_{iso}^2 L^{-\frac{2}{3}} \tag{2.9}$$

$$\begin{aligned} X &= (n_u - 1)du \\ Y &= (n_v - 1)dv \\ Z &= (n_w - 1)dw \end{aligned} \tag{2.10}$$

A further in depth formulation of the Mann Turbulence model set of Equations can be found in Annex B of IEC61400-1(2005) [42] and the Wind Energy Handbook [59].

2.3 Sea State Determination

A sea state is generally characterized by two parameters :

- The significant wave height, H_s.
- The peak spectral period, T_p.

A sea state can be empirically related to the mean wind speed using the Beaufort scale [68]. IEC 61400-3 (2014) [69] is used to determinte the T_p which can be determined from the H_s found from using the Beaufort scale. The Equation for T_p is different depending

on the wave spectrum model used. The wave spectrum is usually modelled using JONSWAP or Pierson-Moskowitz (PM). Both spectra can be seen in Figure 2.5. The JONSWAP spectra is created for the north sea. The north sea is a small sea where the waves cannot fully develop. A specific spectrum for this sea was thus developed [70, 71]. The main frequency is usually in the order of 10^{-1} and can interfere with the 1P frequency of the wind turbine.

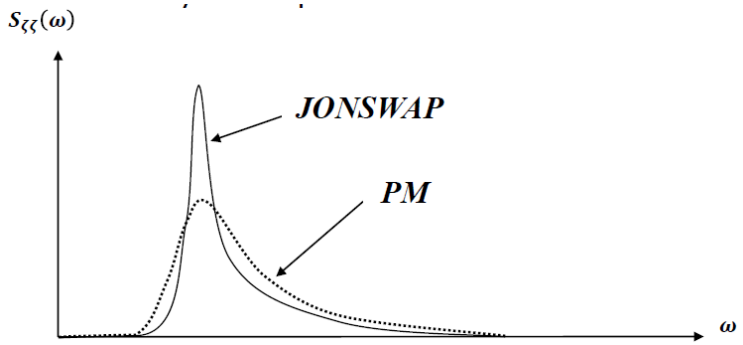

Figure 2.5: JONSWAP and Pierson-Moskowitz wave spectra [72].

Directional wave data can be found in Boukhanovsky et al. (2007) [73]. The spectrum shows that most wave spectra consist of both swell waves and wind waves. The JONSWAP spectrum is not able to account for both swell and wind waves. The spectrum used in FAST.Farm will be unidirectional. T_z can be related to H_s using Equation 2.11 found in IEC 61400-3 (2014) [69]. Then, dependent on the spectrum that is used, the T_p can be calculated. When using the JONSWAP spectrum, T_p can be calculated from Equation 2.12.

$$T_z \approx 12.7\sqrt{H_s/g} \tag{2.11}$$

$$Tp_{JS} = 1.2859Tz \tag{2.12}$$

2.4 Wake Theory

Wakes are defined as the area behind the wind turbine which occurs to have added turbulence [36] and a velocity deficit [37]. Both added turbulence and the velocity deficit are due to the extraction of energy from the wind field.

Before going into detail of the wake properties, some wake terminology should be mentioned:

Wake advection: Wake advection is the spatial change of wind speed in the wake of the turbine [74].

Wake deflection: Wake deflection is the deflection of the wake in a different direction than the main wind field direction due to a yaw misalignment [75].

Wake meandering: Wake meandering is the spatial change in turbulence in the wake of the turbine [74].

Wake expansion: Wake expansion is the radial expansion of the wake, increasing with the distance behind the upwind turbine [74].

Wake merging: Wake merging is wake interaction either occurring in an arrayed wind farm or due to wake deflection [75].

Wake deficits: A wake deficit is the velocity deficit behind the turbine due to the energy subtraction from the wind field. This velocity deficit is spatially dependent [41].

A wake is generally subdivided in two areas : The near and far wake region [76]. The near wake region is the region just behind the rotor and is highly dependent on the geometry of the blades and the number of blades [76, 77]. The tip and root vortices of the blades are very present in this region, which can be seen in Figure 2.6. The far wake region is characterized by turbulence dominant flow, where rotor induced wake properties, like tip and root vortices, are close to non existing [76, 77].

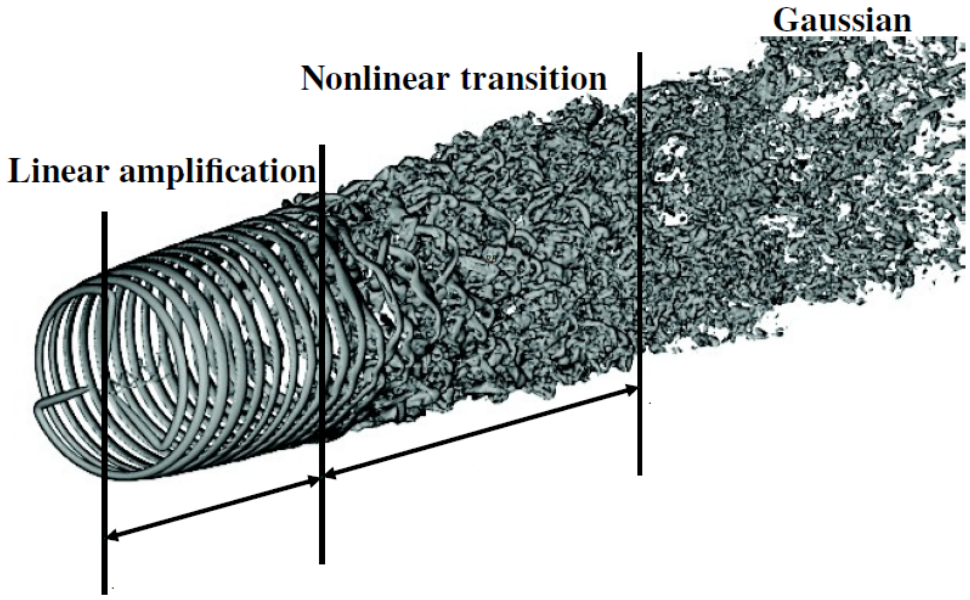

Figure 2.6: Near wake (left) to far wake (right) flow transition [17].

The size and evolution of the wake is highly dependent on the

- Turbine specifications.
- Wake added turbulence.
- Atmospheric boundary-layer structure.

Turbine specifications: The momentum reduction behind the turbine is directly related to the thrust force of the turbine. The velocity deficit will thus increase more with increased momentum reduction.

Wake added turbulence: With wake added turbulence the turbulence added to the stream due to tip vortices is considered. These tip vortices are circular patterns of rotating air left behind a wing as it generates lift [78]. These tip vortices are usually highly turbulent and cause an increase in drag, also called induced drag, which is drag due to lift [79]. This wake added turbulence for turbines is not only caused by the blades, but also by the nacelle and tower [59]. The wake added turbulence frequency is relatively high and

decays quickly which is described in a model of Bossanyi [80] where he describes that turbulent energy increases in frequency and eventually dissipating as heat.

Atmospheric boundary-layer structure: Bossanyi [80] states in the same paper that the dissipation rate of the eddies is highly dependent on the turbulence intensity of the ambient wind field. A high TI and low wind speed will cause a faster rate of decay of the wake added turbulence. Another additional source of turbulence originates from shear-generated turbulence, which comes from the speed gradient between the free flow outside of the wake and the wake [81]. This turbulence results in wake mixing, inwards and outwards, causing the wake to become shallow and broad until the wake has fully recovered. The rate of recovery is highly dependent on the TI of the ABL. Further more it is found that the TI is highly correlated to the the ABL structure [82]. A stable ABL occurs when a downward heat flux is considered, while an unstable ABL occurs when an upward heat flux is considered. A neutral ABL occurs when thermal exchange is absent, which occurs at very high wind speeds. A stable ABL is normally less turbulent than an unstable boundary layer and will thus recover in a slower rate than an unstable ABL [82, 83]. ABL stability is thus important to consider due to its influence on wake propagation.

Figure 2.7 shows the near wake and far wake velocity and turbulence profile, where at the near wake it could clearly be noticed that the turbulence around the blade tip is dominant, while the velocity deficit at the centre shows the nacelle influence on the velocity profile. At the far wake it could be seen that the velocity profile has become shallow and broad, as stated in [81], while the turbulence intensity has increased due to the shear-generated turbulence, which is also what Figure 2.6 shows.

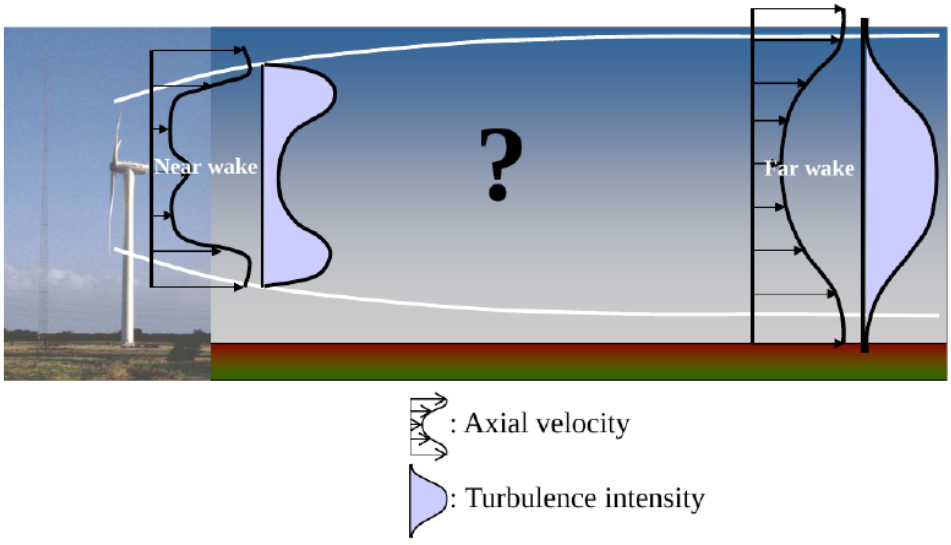

Figure 2.7: Near wake and far wake axial velocity and turbulence intensity [17].

2.5 Wake Model

FAST.Farm is a new wind farm multiphysics modeling tool developed by NREL [39]. FAST.Farm is based on the principles of the Dynamic Wake Meandering (DWM) model. [41]. The DWM model is a wake model used for fast prediction of wind farm power and loads and is considered a mid-fidelity tool. The DWM model is verified by Risø by comparing model predictions with extensive full-scale measurements. The DWM model

is later improved by including atmospheric shear effects on the wake turbulence and by incorporating turbulence build-up in aligned rows of wind turbines [84]. The DWM model has been compared to the high-fidelity vortex method (VM) and the actuator line large eddy simulation (AL-LES) [85]. FAST.Farm has been calibrated using SOWFA [38, 75], a high-fidelity modeling tool.

FAST.Farm consists of four modules, each having their own physics domain and implementation :

The super controller (SC) : The SC module of FAST.Farm can solve wind plant super controller dynamics.

OpenFAST (OF) : OpenFAST [40] is a wrapper that is able to model the dynamics, environmental excitations and coupled system responses for each individual wind turbine. OpenFAST will be discussed in section 2.11.

The Wake-Dynamics model (WD) : The WD module is able to calculate the wake advection, deflection and expansion for each separate WT. It further more takes the wake-velocity deficit into account close behind the rotor disk by creating a near-wake correction model. Each WT has a WD module

The Ambient Wind and Array Effects (AWAE) : The AWAE module processes the ambient wind and wake interaction across the wind farm in FAST.Farm. It also takes the connection between the OpenFAST inflow sub model and the ambient wind field into account.

2.5.1 Wake-Dynamics in FAST.Farm

Wake deflection in FAST.Farm is taken into account by creating a deflected wake centerline which is dependent on the yaw error and the generated thrust. Wake advection is taken into account by accelerating the wake from near wake to far wake and by having a transversal change in velocity due to the ambient wind field which results in an elliptical wake. Furthermore, the wake will spatially expand, which resembles the real life wake evolution. The wake evolution is modeled using the thin shear-layer approximation of the Reynolds-averaged Navier-Stokes equations under quasi-steady-state conditions in axisymmetric coordinates with turbulence closure capturing using an eddy-viscosity formulation dependent on small turbulent eddies [75, 86].

The near-wake correction submodel in the WD module calculates the velocity deficit behind the rotor disk and is mainly used to improve the far-wake solution and the wake radial expansion.

Figure 2.8 shows the wake deflection due to skewed inflow including the horizontal wake deflection correction, which is represented by the lower undashed blue line. The Figure also shows the wake expansion and wake advection, where both the axial (advection) and radial (expansion) components of the wake increase in length [75].

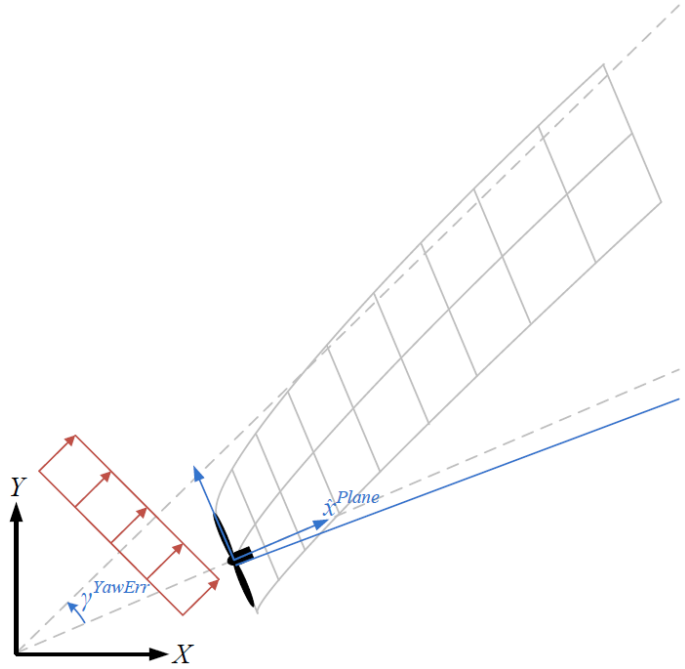

Figure 2.8: Spatial wake deflection, wake advection and wake expansion for one moment in time in FAST.Farm [75].

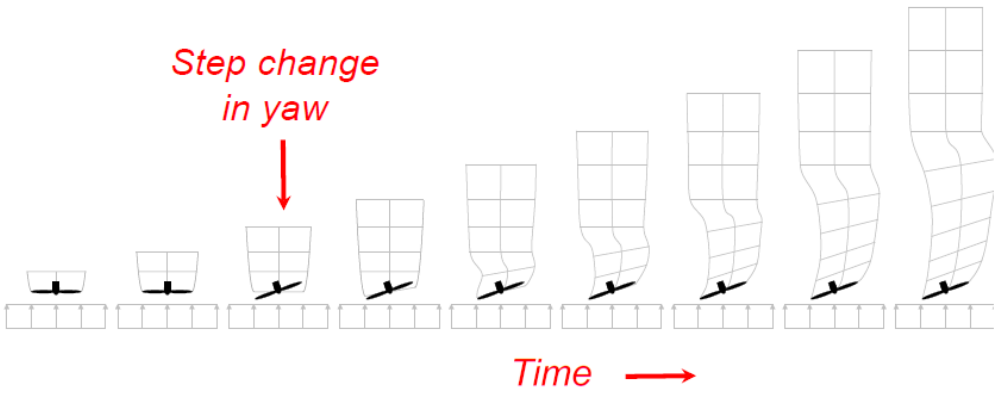

Figure 2.9: Spatial wake deflection, wake advection and wake expansion over time in FAST.Farm [75].

2.5.2 Ambient Wind Array Effects in FAST.Farm

THE AWAE module processes the preprocessed ambient wind generated from the Mann Turbulence generator [87] to the OpenFAST InflowWind module and the wake-merging submodel. The wake-merging submodel identifies overlapping wake zones across the wind field and merges the deficit results. Overlapping wake zones are identified through overlap of discrete wake volumes, represented by the cylindrical area between two wake planes, which have the same alignment as its associated wind turbine.

Figure 2.10 shows the discrete wake merging for a two turbine case in the low-resolution (yellow) and high-resolution (green) wind field [75].

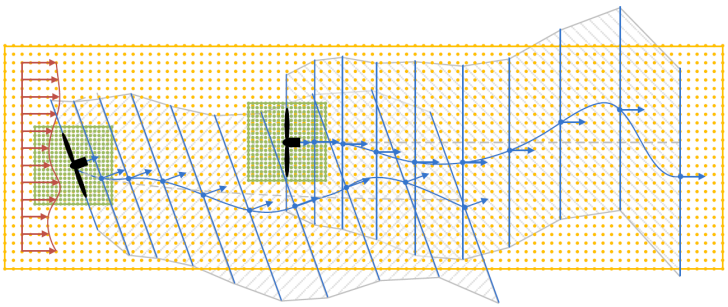

Figure 2.10: Wake interaction between two turbines in FAST.Farm [75].

2.6 Power Production

Cost reduction by increasing captured energy from the wind has been studied for a long time. For farm power optimization, first the power production of single wind turbines should be determined. Theoretical power production of an unyawed single wind turbine below rated wind speed can be calculated using Equation 2.13.

$$P = C_P(\lambda, \beta)\frac{1}{2}\rho A V^3 \tag{2.13}$$

Where

- P is the total power produced in W.
- C_P is the power coefficient.
- ρ is the air density in $\frac{kg}{m^3}$.
- A is the rotor blade area in m^2.
- V is the wind speed in $\frac{m}{s}$.

The power coefficient, C_P, is the ratio of actual power produced by a wind turbine divided by the total wind power potential flowing through the turbine blade area at a specific wind speed. In order to maximize single wind turbine power production, C_P should be maximized. A theoretical maximum C_P value has been determined by Betz and is called the Betz limit. This limit is 59.3 % [88]. This value is in reality never reached. The optimal C_P value is a function of the tip speed ratio (TSR), λ, and the blade pitch angle (BP), β. Below rated both the TSR and BP angle should be optimized to have maximum power production. Figure 2.11 shows the relation between the power coefficient on the y-axis and the TSR on the x-axis.

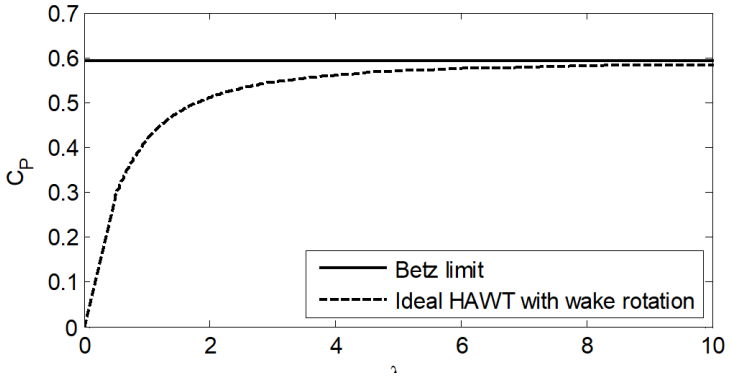

Figure 2.11: Power coefficient [-] as function of the TSR [-] of an ideal HAWT wind turbine [89].

The TSR can be calculated using Equation 2.14.

$$\lambda = \frac{\omega R}{V} \tag{2.14}$$

Where

- λ is the TSR.
- ω is the angular velocity in $\frac{rad}{s}$.
- R is the rotor radius in m.

The wind turbine power that can be extracted from the wind field is highly dependent on the incoming wind speed, as Equation 2.13 shows. A power curve with optimal C_P is shown in Figure 2.12.

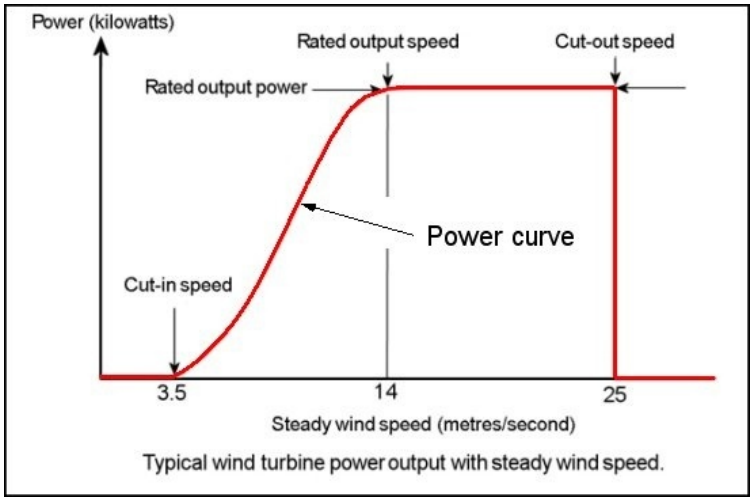

Figure 2.12: Example of a typical wind turbine power curve. [3]

3 transition points can be seen in the power curve of Figure 2.12 at:

- Cut-in speed

[3] quora.com/What-is-a-power-curve-and-how-do-we-draw-one [Visited on the 9th of January 2020]

- Rated wind speed
- Cut-out speed

Below cut-in no power is produced by the wind turbine.

Between cut-in and rated wind speed power is produced with the aim to produce maximum power and thus aiming for a maximum power coefficient. The power produced here is dependent on the cubed wind speed ($P \approx cV^3$, where c is a constant).

Between rated and cut-out wind speed power is produced with the focus to keep the power production at a constant value, which is predetermined in the design of a wind turbine. Equation 2.13 is used to determine the value for C_P which is needed to create a constant power production for different wind speeds between rated and cut-out. A BP angle is found corresponding to the C_P giving rated power and is used by the wind turbine controller to pitch the wind turbine blades.

Above cut-out the turbine will not produce any energy.

An effective and simple method to predict wind turbine performance is the Blade Element Momentum (BEM) method. The BEM method starts with the actuator disk concept and momentum theory where the axial induction factor, a, is induced to describe C_P. BEM can be expanded by adding rotor disk theory, which will take torque on the rotor blades into account using angular momentum theory, where the tangential induction factor, $a_t^{'}$, describes C_P.

$$P = C_P \frac{1}{2} \rho A V^3 \tag{2.15}$$

$$C_P = 4a(1-a)^2 = 4a_t^{'}(1-a)\lambda^2 \tag{2.16}$$

$$T = C_T \frac{1}{2} \rho A V^2 \tag{2.17}$$

$$C_T = 4a(1-a) \tag{2.18}$$

Where

- λ is the TSR, shown in Equation 2.14.
- T is the WT thrust in N.
- C_T is the thrust coefficient.

BEM will divide the blade in segments. Every segment has its own corresponding drag and lift coefficient. Using trigonometry, the normal and tangential coefficient can be calculated for different pitch angles. Integrating over the length of the turbine blades, the thrust and torque can be calculated. Using Equation 2.19, the power produced can be calculated, where T is the torque and ω is the angular velocity.

A tip and hub loss correction can be added to take losses at the hub and the tip into account [90, 91].

$$P = T\omega \tag{2.19}$$

2.7 Power Production in Steady Yaw

Yawing of turbines can be used to steer the wake to optimize total power production of the wind farm. This yawed condition will cause increased fatigue damage on the blades and an increased moment about the yaw axis [59]. A yawed turbine will also be less efficient than a non-yawed turbine. Similar assumptions are made to calculate forces, moments and power production as to the non-yawed turbine. Calculations regarding the yawed turbine are however more complex. Rotor thrust and power production can be calculated with the same Equations (2.15 and 2.17), having a different power and thrust coefficient, which are shown in Equation 2.20 and Equation 2.21 which is derived from setting up axial momentum and mass flow Equations using Figure 2.13.

$$C_P = 4a(cos\gamma - a)^2 \tag{2.20}$$

$$C_T = 4a(cos\gamma - a) \tag{2.21}$$

Where γ is the yaw angle.

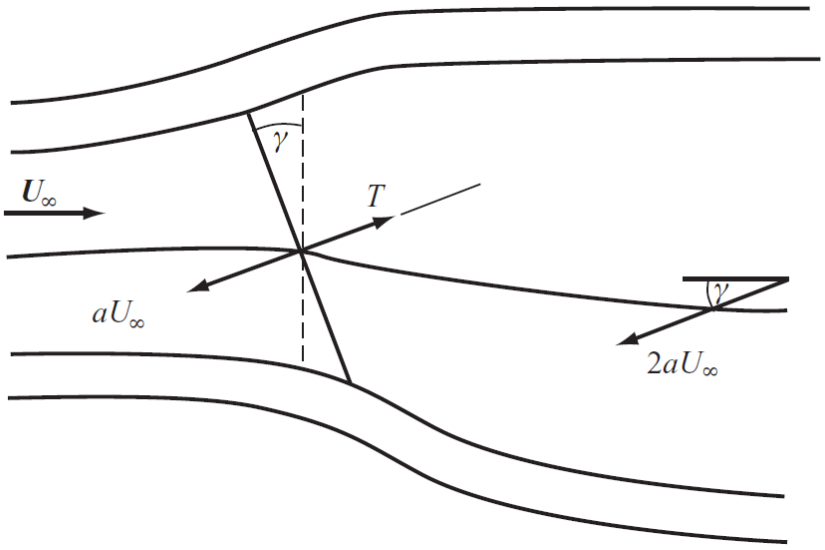

Figure 2.13: Deflected wake of a yawed turbine and induced velocities [92].

The maximum power coefficient can be found by differentiating Equation 2.20 with respect to the axial induction factor and setting it to zero, resulting in Equation 2.22 and Equation 2.23 where both the maximum value for C_P and the axial induction factor$a$ are different for different yaw angles, which is also seen in Figure 2.14.

$$C_{Pmax} = \frac{16}{27} cos^3\gamma \tag{2.22}$$

$$a_{max} = \frac{cos\gamma}{3} \tag{2.23}$$

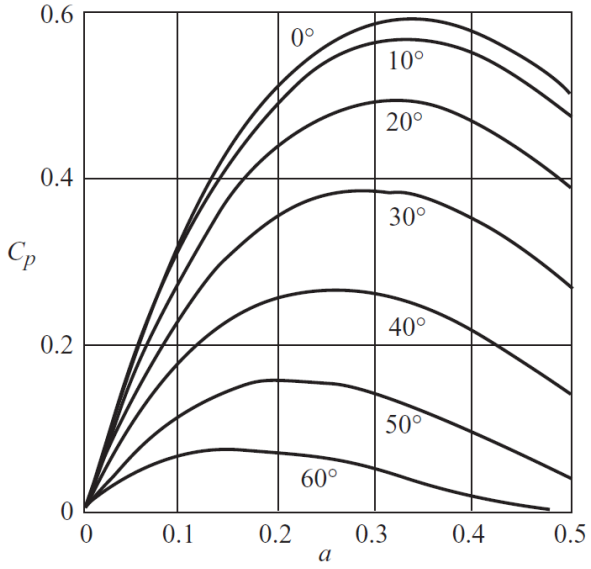

Figure 2.14: Power coefficient variation with yaw angle and axial flow factor [93].

FAST.Farm uses the Pitt-Peters linear theory, which relates the axial induction factor to thrust and moment coefficients. This theory is iterative and can be used with blade element theory [94].

$$(a) = [L](C) \tag{2.24}$$

$$(a) = \begin{bmatrix} a_0 \\ a_c \\ a_s \end{bmatrix}, (C) = \begin{bmatrix} C_T \\ C_{my} \\ C_{mz} \end{bmatrix} \tag{2.25}$$

$$[L] = \begin{bmatrix} \frac{1}{4A(a_0)} & 0 & -\frac{15}{128}\pi \tan\frac{\chi}{2} \\ 0 & -\sec^2\frac{\chi}{2} & 0 \\ \frac{15}{128A(a_0)}\pi \tan\frac{\chi}{2} & 0 & -\left(1-\tan^2\frac{\chi}{2}\right) \end{bmatrix} \tag{2.26}$$

The value for $A(a_0)$ is dependent on the momentum theory used (Glauert's momentum theory or Coleman theory) and χ is the wake skew angle, which is of similar magnitude as the yaw angle, γ.

2.8 Wake Steering For Power Production Optimization

Wind farm power production can be optimized by optimizing single wind turbine power production or by optimizing total wind farm power production through changing control settings. A sensor input measures the wind speed and wind direction. For single wind turbine power optimization the turbine will be yawed if a yaw error occurs, which is when the turbine is not aligned to the wind.

The turbine only yaws when a yaw error threshold is exceeded. This is decided by a controller that receives the wind vane position several times per second. A fast response time for turbine yawing is less of importance due to its cosine relationship with power production, which Equation 2.20 shows. Usually dead band control is used to prevent repeated activation-deactivation cycles. Both when the turbine is being yawed or not yawed, the use of a yaw break can be considered for increased damping. Compared to blades, the response time of a yaw system is also slow due to tower top and blade inertia around its rotating axis. The yaw timestep is highly dependent on two factors. When a very small yaw timestep is used, the power production can be maximized and controlled to a high extent. The drawback is however that the yaw actuator loads increase with decreased timestep size. A good balance should be found between yaw actuator loads and power production.

Wake steering control has been studied in several occasions. Wind tunnel tests [9, 10], field tests [11, 12] and CFD simulations [13] are done to study wake steering in the past.

Pieter Gebraad (2014) [14] looked into the effects of wake steering control with the aim of optimizing wind farm power production using a two turbine set-up of the NREL-5MW [95] turbine with 7 rotor diameters of distance. Results show an increase in power production for the two wind turbine case. This is however under perfect conditions for wake steering: A small turbulence intensity of 6% is considered to limit wake mixing, a neutral ABL is considered and the best wake overlap situation is taken as baseline.

In 2016 and 2017 similar software is used as in [14] for the Princess Amalia Wind Park in the Netherlands where again a significant increase of power production is found for a wind farm consisting of 60 2MW Wind Turbines where different wind speeds and turbulence intensities are considered [15, 16].

Generally the yaw misalignment for optimization is taken from a lookup table where the lookup table contains the optimal yaw angle for single wind turbines in wind farm arrangement for each different wind speed and wind direction.

Stoyan Kanev (2020) [7] looked at the development of a dynamic wake steering algorithm and also looked at the yaw misalignment of an individual turbine and its influence on wind farm static power gain, which can be seen in Figure 2.15 for a 3 x 3 wind farm with its main alignment directions from North to South (5D) and East to West (7D). This simulation was done as baseline simulation and gives information regarding the optimal wake steering angle and the optimal wind direction.

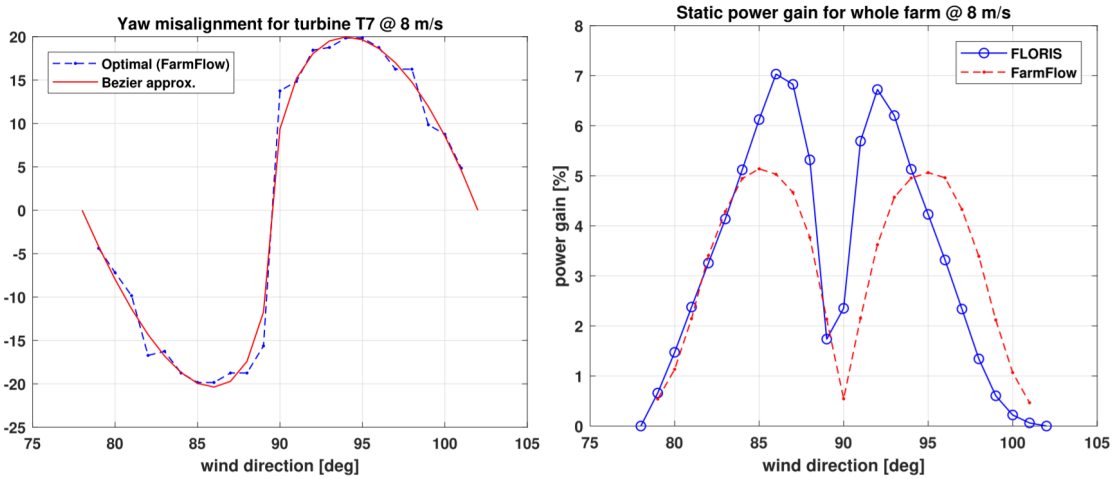

Figure 2.15: Yaw misalignment angles for turbine T7 (left), and static power production gain for the whole farm (right) as function of the wind direction [7].

Stoyan Kanev (2020) concluded that the gain from wake redirection is about 20% lower than based on static analysis due to its stochastic turbulent nature .

FAST.Farm uses a programmed pitch rate of 2 rad/s, whereas the the control timestep, DT, is constant for every controller and is set to default, which is 0.025s. This value is chosen as follows : $DT = \frac{1}{10NF_{max}}$, where the Natural Frequency is in Hz.

For farm power production optimization complex software and controllers can be developed. Tools like SOWFA [38], FAST.Farm [39], FLORIS [96] and WindFarmer [97] are all tools made to optimize power production and cost on wind farm level. Each software needs a wake model and some models are validated using a high-fidelity tool : Both FLORIS and FAST.Farm are validated against SOWFA, a high-fidelity large-eddy simulation (LES) tool.

FAST.Farm has a super controller option, a controller able to control the wind farm on a multi-turbine level. The super controller is highly comparable to the super controller used in SOWFA, but is however not fully developed yet.

2.9 Axial Induction Control For Power Production Optimization

Similar to wake steering control, total wind farm power production can be optimized by changing control settings of the BP angle of the upwind turbine. Figure 2.16 shows the velocity deficit dependent on the axial induction factor. Due to mixing with the ambient wind field the velocity deficit decreases over distance.

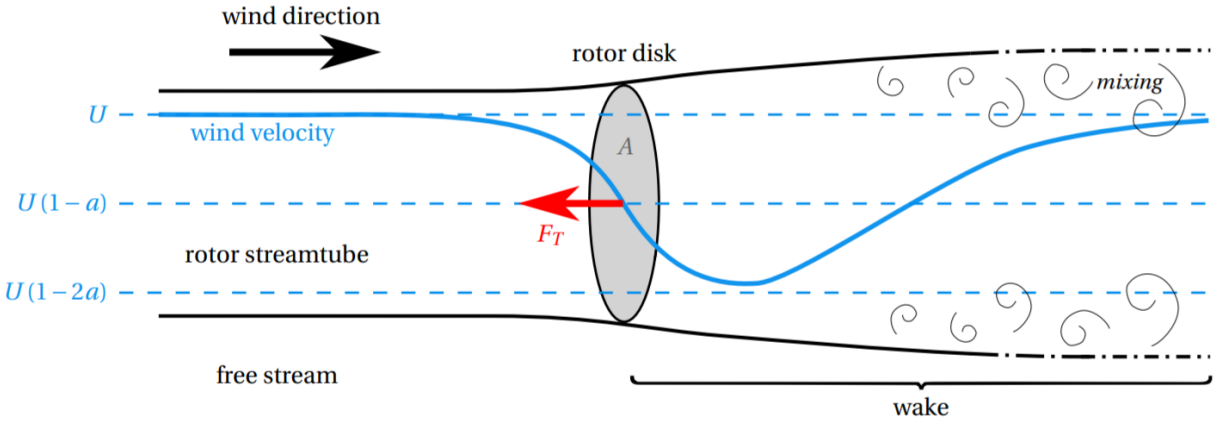

Figure 2.16: Wake axial velocity dependent on the magnitude of the axial induction factor [98].

Both power production and the thrust force on the turbine are dependent on the axial induction factor (Equation 2.15-2.18). Figure 2.17 shows its dependency. When an axial induction factor of 0.5 or higher is reached, Betz theory becomes invalid. The maximum value for C_P is found at $a = 0.33$. The corresponding value for C_T can then be found. The thrust force from the rotor on the wind field will determine the flow velocity reduction. $\frac{dC_T}{da}$ is larger than $\frac{dC_P}{da}$ around a = 0.33, since $\frac{dC_P}{da}$ is close to 0, which means that the flow velocity reduction will decrease faster than the power reduction. The decreased velocity deficit behind the upwind turbine results in an increase in power production of the downwind wind turbine.

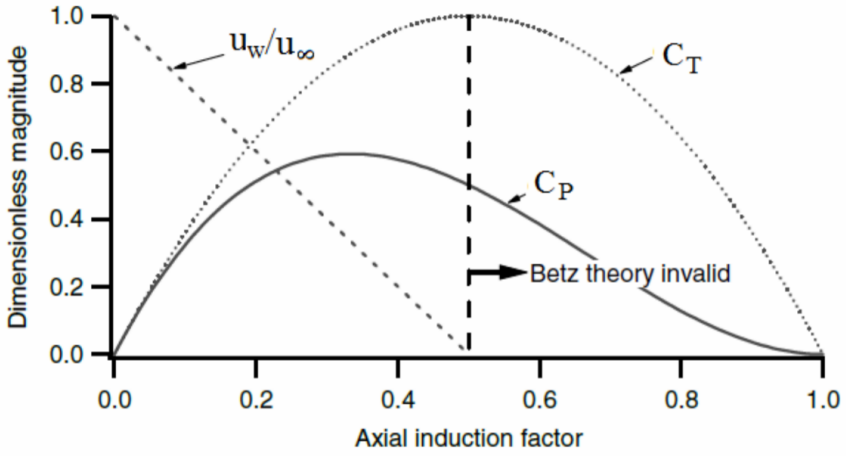

Figure 2.17: Power and thrust coefficient for changing axial induction factor with optimized TSR [99].

.

Using 1D momentum theory, a mathematical explanation can be given of the fundamentals of axial induction control [17].

A sketch of two wind turbines is shown in Figure 2.18. The combined power coefficient of the two wind turbines should be optimized in order to maximize the total power production of the wind farm. By introducing an axial interference coefficient, which can be seen in Equation 2.27, the Equation can be rewritten in a way that the power coefficient is only dependent on the axial induction coefficients.

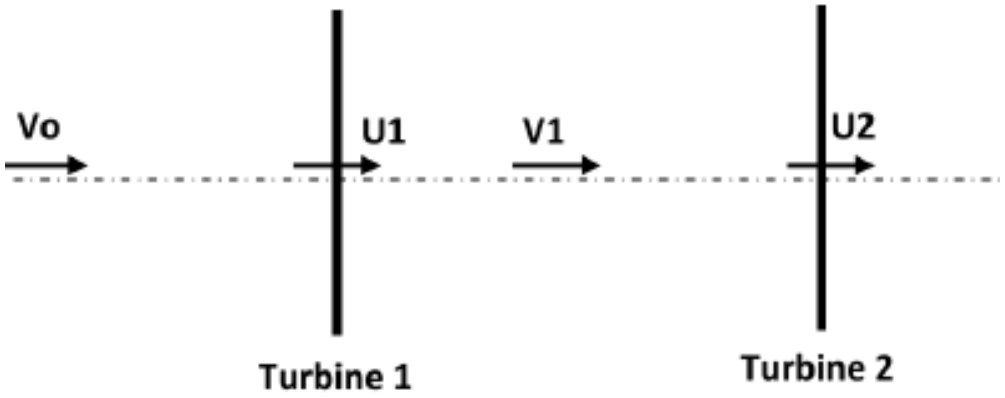

Figure 2.18: Configuration of two wind turbines [17].

$$a_n = 1 - \frac{u_n}{V_{n-1}} \tag{2.27}$$

$$\begin{aligned} C_P(a_1, a_2) &= \frac{P_{tot}}{P_{available}} \\ &= \frac{\frac{1}{2}\rho A V_0^3 C_{P_1} + \frac{1}{2}\rho A V_1^3 C_{P_2}}{\frac{1}{2}\rho A V_0^3} \\ &= C_{P_1} + \frac{V_1^3}{V_0^3} C_{P_2} = C_{P_1} + (1-2a_1)^3 C_{P_2} \\ &= 4a_1(1-a_1)^2 + 4a_2(1-a_2)^2(1-2a_1)^3 \end{aligned} \tag{2.28}$$

By partially differentiating to both a_1 and a_2 and setting those equations to zero, the optimal values for a_1 and a_2 can be found, where a_1 = 0.2 and a_2 = 0.33. Comparing this to the optimal value for a single wind turbine, which can be found by differentiating Equation 2.16, resulting in a = 0.33, it can be concluded that the optimal C_P for a single wind turbine is higher than the optimal C_P for the upstream wind turbine in an arrayed situation. This does have a significant deviation from reality due to the assumption that the downwind wind speed is only dependent on Equation 2.27 and does not consider wake advection and expansion. However, it does show the potential possibility of wind farm power production increase due to axial induction control of the upwind turbine.

Overall different results are found for axial induction control. Pieter Gebraad (2014) [100] also looked into the effects of axial induction control on the same two turbine set-up as discussed in section 2.8. For the two turbine set-up in SOWFA no power production increase was found. Further LES Simulations by Nilsson et al. (2014) [19] and Bartl et al. (2016) [18] did neither find an increase in power production.

However, lots of research is done where an increase of power production is found. Wake models show an increase in total wind farm power production [20, 21, 22] and high-fidelity tools also show an increase in wind farm power production [23, 24, 25]. Wind tunnel test with experimental data show an increase as well [9, 26].

What causes this significant difference in results is not known, although increased wake mixing can cause the downstream wake to increase in speed resulting in a decreased benefit of axial induction control.

2.10 Turbine Selection

2.10.1 DTU 10MW reference turbine

The main condition on choosing a WT for the research is whether a reliable model is available of it which can be implemented in OpenFAST [40] and FAST.Farm [39]. A model is available for the NREL 5MW RWT [95] and the DTU 10MW RWT [101]. For the simulation, the DTU 10MW reference turbine is considered [101], since it is more relevant for recent and future work. Everything of the DTU 10MW RWT, except the blades, is obtained by upscaling of the NREL 5MW reference turbine by making assumptions on geometrical similarities [102]. The turbine parameters can be found in Table 2.1.

Table 2.1: Key parameters of the DTU 10MW Reference Wind Turbine [101].

Parameter	**DTU 10MW RWT**
Wind Regime	IEC Class 1A
Rotor Orientation	Upwind
Rotor configuration	3 blades
Control	Variable Speed, Collective Pitch
Drivetrain	Medium Speed, Multiple Stage Gearbox
Rotor, rotor diameter	178.3 m, 5.6 m
Hub height	119.0 m
Cut-in, Rated, Cut-out wind speed	4 m/s, 11.4 m/s, 25 m/s
Rated power	10 MW
Cut-in, Cut-out rotor speed	6 rpm, 9.6 rpm
Rated tip speed	90 m/s
Maximum Generator Speed	480.0 rpm
Gearbox Ratio	50
Maximum Tip Speed	90 m/s
Hub Overhang	7.1 m
Shaft Tilt Angle	5.0 deg.
Rotor Precone Angle	-2.5 deg.
Blade Prebend	3.332 m
Rotor, Nacelle, Tower Mass	229 tons, 446 tons, 605 tons

Rotor design is based on the direct upscaling of the NREL 5MW rotor [95], with dimension changes using a computational tool based on BEM theory and numerical optimization. Constraints for blade radius were made by upscaling of the NREL 5MW rotor, constraints for blade thickness were made for stiffness considerations and constraints for blade chord were made to reduce thrust in operation and stand still. Different TSRs were considered to optimize the power coefficient. The resulting power, thrust and coefficient curves can be found in Figure 2.19.

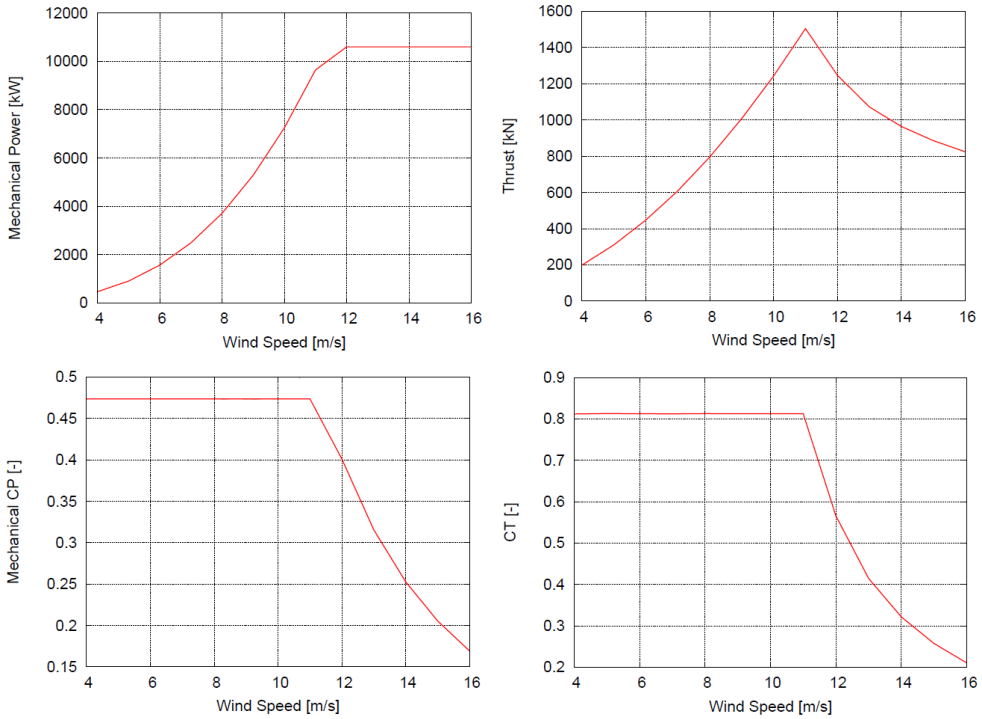

Figure 2.19: Mechanical power curve (top left), thrust curve (top right), mechanical power coefficient curve (bottom left) and thrust coefficient curve(bottom right) of the DTU 10MW turbine using HAWTOPT [101].

Furthermore, Aero-Servo-Elastic design is considered with the goal to avoid tower mode excitation from the 3P frequency at low wind speeds.

The tower outer diameter of the DTU 10MW turbine is 8.3m at the bottom and 5.5m at the top and is linearly tapered. 10 different sections are created for the turbine tower with each a different wall thickness. The stiffness and mass properties of the tower can be found in the DTU 10-MW Reference Wind Turbine report [101].

2.10.2 Floater concepts

A floating wind turbine (FWT) can be considered in regions with limited amount of shallow water (<45m). A FWT is mainly stabilized in the following three ways [89]:

- Ballast stabilized (spar).
- Buoyancy stabilized (semi-submersible).
- Mooring line stabilized (tension leg platform).

The type of stabilization will influence the dynamic performance of the floater. A spar usually has small motions, is easy to install but requires a large water depth.

A semi-submersible has relatively large motions, is easy to install and does not require a large water depth.

A TLP will have very small motions due to the cable tension and has a small footprint on the seabed. However, a TLP is hard to install. The motions of the TLP floater are in the same range as for bottom-founded turbines, due to the high stiffness caused by the cable tension.

Figure 2.20: 3 different floater concepts from left to right : spar - semi-submersible - TLP. [4]

Lifes50+ is a project focused on developing floaters capable of being installed in water depths ranging from 50m to 200m for 10MW WTs with a final goal to decrease the LCOE for floating wind energy. Four concepts are considered and from those four concepts two are chosen for further experimental and numerical investigation. The four concepts can be seen in Figure 2.21. The final two concepts further elaborated are the NAUTILUS-10 floating substructure and the OO-STAR floating substructure.

Figure 2.21: Lifes50plus concepts. [5]

[4] https://www.dnvgl.com/technology-innovation/broader-view/electrifying-the-future/third-generation-wind-power.html[Visited on the 9th of January 2020]

Both models have an existing OpenFAST model, but finally the Nautilus 10MW FWT model is chosen for further modeling due to issues with the OO-Star model.

2.10.3 Nautilus Floater

The Nautilus Floater, designed by Nautilus Floating Solutions, is further developed in the Lifes50+ project mentioned in subsection 2.10.2. The floater concept can be seen in Figure 2.22.

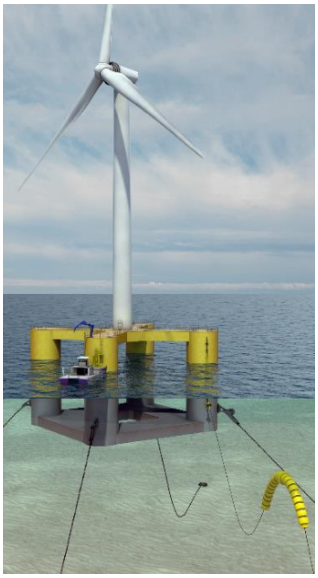

Figure 2.22: Nautilus Floater concept [103].

The semi-submersible floater is symmetric and consists of four columns, which connect the main frame by an X-shaped deck and a square-shaped ring pontoon on the top and the bottom, respectively. The floater is moored to the seabed using four catenary steel chain mooring lines.

Restoring forces are achieved by the four columns due to its large water plane area each providing buoyancy forces. The ring pontoon is filled with passive ballast to improve stability by lowering its centre of gravity. An active ballast system is designed to optimize efficiency by maintaining the vertical alignment of the tower. The ballast system is able to pump sea water into each column separately.

2.11 Turbine Model

OpenFAST models of the DTU 10MW WT, Nautilus Floater DTU 10MW WT and the OO-Star DTU 10MW WT are available at `https://rwt.windenergy.dtu.dk/dtu10mw/dtu-10mw-rwt`. [53, 56, 104, 105, 106].

2.11.1 Tower model

The tower model in FAST is modelled as a flexible beam for the Nautilus floater with a hub height, z_{hub}, of 119m above still water level (SWL).

[5] `https://lifes50plus.eu/`[Visited on the 9th of January 2020]

2.11.2 Mooring line model

Mooring lines can be modelled using MoorDyn [107]. MoorDyn is a lumped mass mooring line model able to simulate mooring line dynamics by discretizing the cable dynamics over the length of the mooring line. MoorDyn takes internal axial stiffness and damping into account, which can be changed to desired values. MoorDyn also takes weight, buoyancy and hydrodynamic forces into account, which can be seen in Figure 2.23.

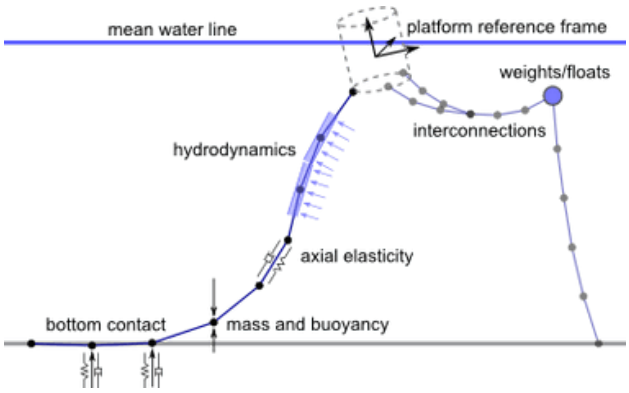

Figure 2.23: MoorDyn force modeling components [107].

The seabed contact is taken into account by using vertical spring damper forces. The hydrodynamic forces are taken into account by using Morison's equation [108] [109].

The mooring lines are modelled for a water depth of 130m and an unstretched length of 833.24m. On one side, the mooring lines connect to the columns and on the another side the mooring lines are fixed to the seabed by drag anchors for station keeping. Mooring line discretizetion can be chosen in OpenFAST and is chosen to be discretized in 100 segments with an internal damping ratio of 1, similar to the mentioned literature [110].

2.11.3 Hydrodynamics model

The hydrodynamic properties, which are based on linear potential theory, are calculated using the diffraction-radiation in WAMIT [111]. WAMIT consists of an advanced set of tools to analyze wave interaction for offshore platforms.

$$\left[-\omega^2(\mathbf{M}+\mathbf{A}(\omega))+i\omega\mathbf{B}(\omega)+\mathbf{C}_{hst}\right]\hat{\xi}(\omega)=\hat{\mathbf{X}}(\omega)\hat{\eta}(\omega) \tag{2.29}$$

Where WAMIT calculates:

- $\mathbf{C}_{hst}$: The hydrostatic restoring matrix.
- $\mathbf{A}(\omega)$: The hydrodynamic added mass matrix.
- $\mathbf{B}(\omega)$: The radiation damping matrix.
- $\hat{\mathbf{X}}(\omega)$: The wave diffraction forces.

Where ω is the angular frequency in $\frac{rad}{s}$, $\mathbf{M}$ is the inertia matrix and $\hat{\eta}(\omega)$ is the Fourier coefficient for the floater motion in 6 DOF. Equation 2.29 will define the equation of motion (EOM) of the unrestrained floater. The floater matrices can be further found online in Pegalajar et al. (2018) [56].

A potential-flow solver does not take viscous effects into account. Those effects are thus modeled within FAST using HydroDyn. These values are determined in earlier model scale experiments [112].

2.11.4 Nautilus Floater Natural Frequencies

A decay test is carried out for the Nautilus 10MW WT to find system natural frequencies and system coupling. A fourier analysis is carried out on the corresponding time series, resulting in the natural frequency results that can be found in Table 2.2.

Table 2.2: System natural frequencies and periods from decay simulations in FAST [104].

	Surge	**Heave**	**Pitch**	**Yaw**	**Tower**
Natural frequency [Hz]	0.0085	0.518	0.0340	0.0107	0.526

2.11.5 Controller

The controller for the DTU 10MW WT is designed for onshore turbines. The controller will cause negative damping for the offshore floating turbine and should thus be tuned to prevent negative damping to occur, mentioned in Larsen et al. (2007) [113].

2.11.6 Blades

The rotor diameter, D, is 178.3m, which is unchanged from the original DTU 10MW reference turbine, similar to the rest of the data found in Table 2.1. The rotor aerodynamics have been updated to AeroDyn v15 [114].

2.11.7 Model visualisation

Figure 2.24 shows the Nautilus 10MW WT model in OpenFAST.

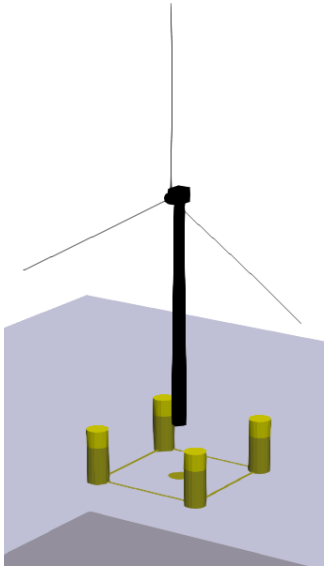

Figure 2.24: Computational model of the nautilus 10MW WT visualized in OpenFAST with lines representing the prebent blades. The tower and nacelle are colored black while the hydrodynamic members are colored yellow [110].

2.12 Drivetrain Theory

2.12.1 Drivetrain concepts

The drivetrain consists of the following main components:

- Hub
- Low speed shaft
- Gearbox
- High speed shaft
- Generator
- Four point support consisting of bearing and torque arm supports

The hub connects the rotor blades to the main shaft. The main shaft is then exposed to high torque loads and low angular velocity created by the rotor blades. A gear box can be implemented depending on design choices. When a gearbox is implemented, a high speed shaft will connect the gearbox to the generator. At the end of the high speed shaft a generator will convert rotational energy of the high speed shaft into electrical energy. For a drivetrain without a gearbox modifications to the generator should be made, which is considered below. The shafts and gear components are supported by bearings and torque arm supports.

The generator size of a WT is highly dependent on the angular velocity of the mechanical shaft. A low angular velocity results in a large generator diameter and a high angular velocity results in a small generator diameter, which can be explained with Equation 2.30. The size of the WT generator is directly dependent on the number of poles needed: More poles needed means that a larger generator should be used.

$$n = \frac{120f}{n_p} \tag{2.30}$$

Where

- n is the angular velocity in rpm.
- f is the grid frequency in Hz, which is 50 in Europe.
- n_p is the number of poles needed for the generator.

The following drivetrain layouts can be considered when designing a WT [115]:

- A direct drive drivetrain : A direct drive drivetrain uses a large generator without a gearbox. Due to the decrease in angular velocity, especially when upscaling the WT, the generator size will become significantly larger and will thus increase the generator mass. Also, generator cooling will cause turbine efficiency to go down when increasing the generator size [116].
- A high speed drivetrain model : Using a gearbox to change the angular velocity of the generator shaft results in a decreased generator size. Due to the implementation of the gearbox, the shaft length is longer than the shaft length of the direct drive drivetrain. The gearbox transmission ratio of a high speed gearbox is usually between 80 and 120.

- A hybrid drivetrain model : The hybrid drivetrain model consists of a medium sized generator with a small gearbox. This drivetrain is designed for larger (offshore) WTs, where a direct drive drivetrain does not work due to generator mass, but using a large generator causes increased fatigue loads leading to increased downtime [117]. A gearbox transmission ratio of a medium speed gearbox is usually between 10 and 20.

Figure 2.25 shows the difference between the direct drive drivetrain model (left) and the high speed drivetrain model (right), where a difference in generator size and shaft length can be seen.

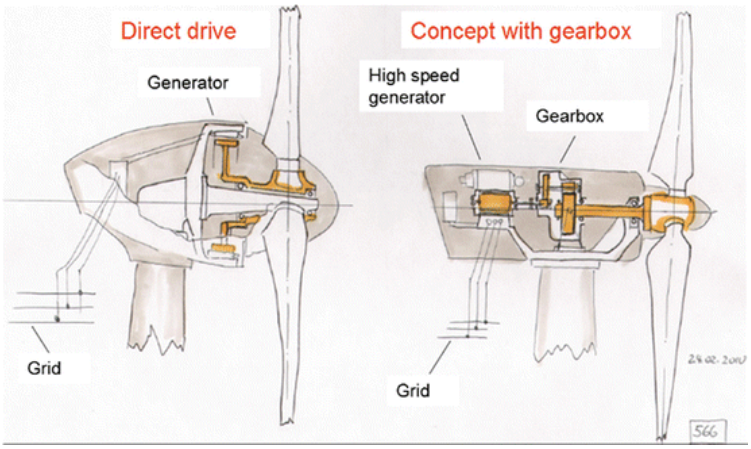

Figure 2.25: Inside of a Direct Drive drivetrain Nacelle (left) and a Gearbox drivetrain Nacelle (right) [118].

The torque loads and the angular velocity between the high and low speed shaft of a gearbox drivetrain can be described using Equation 2.31 and 2.33 for parallel gear stages or using Equation 2.32 and 2.33 for planetary gear stages [119]. A planetary gear stage is more compact an will create a higher torque density than parallel gear stages. A WT gearbox is usually designed with one planetary gear stage and two parallel gear stages or two planetary gear stages and one parallel gear stage to obtain the desired gear ratio.

Dependent on the angular velocity of the gear, a spur gear or helical gear can be chosen. Where a spur gear will not create any non torque loads, a helical gear will. A spur gear will however create more noise. For low angular velocities a spur gear is thus desired, while for high angular velocities a helical gear is desired. Generally planetary gear stages in WTs consist of spur gears, while parallel gear stages consist of helical gears. When helical gear stages are used the use of thrust bearings is advised, which is a bearing that takes axial loads. Using a double helical gear can also remove axial forces.

The low speed axis will have larger torque loads and should be designed with a larger shaft diameter.

$$\frac{\omega_{hs}}{\omega_{ls}} = R \tag{2.31}$$

$$\frac{hs}{ls} = 1 + \frac{D_{ring}}{D_{sun}} \tag{2.32}$$

$$P = T_{hs}\omega_{hs} = T_{ls}\omega_{ls} \tag{2.33}$$

where

- R is the gearbox ratio.
- T_{hs} is the high speed shaft torque in Nm.
- T_{ls} is the low speed shaft torque in Nm.
- ω_{hs} is the high speed shaft angular velocity in $\frac{rad}{s}$.
- ω_{ls} is the low speed shaft velocity in $\frac{rad}{s}$.

2.12.2 Drivetrain frequencies

Drivetrain frequencies are generally higher (>20 Hz) [115] than the frequency ranges of the wind, waves, rotor blade (1P and 3P) and the global natural frequencies of the wind turbine. The drivetrain main frequency is determined by the frequency at which the gear teeth mate together. This gear mesh frequency is equal to the shaft frequency multiplied by the number of teeth of the gear.

Due to the small simulation timestep of the drivetrain, coupling the simulation of the drivetrain and the rest of the wind turbine will cause an increased calculation time. By decoupling the drivetrain simulation and the FWT simulation, the calculation time will be shortened, without having a significant deviation from the coupled simulation, due to the large difference in frequency ranges.

2.13 Drivetrain Model

2.13.1 Drivetrain selection for a 10MW offshore floating wind turbine

As discussed in subsection 2.12.1, three possible drivetrain concepts can be used for the development of a wind turbine.

Due to the rapid increase of wind turbine size over the years, a light weight drivetrain model should be designed. Upscaling a direct drive drivetrain will lead to an undesired large tower top mass, while a high speed drivetrain is more likely to fail than a medium speed drivetrain due to the larger gear ratio. Choosing a medium speed (hybrid) drivetrain is therefore the best option.

2.13.2 10MW hybrid drivetrain model

For the calculation of the bearing fatigue the 10MW hybrid drivetrain model is considered developed by NTNU [46, 47] using SIMPACK [48]. The model is designed by upscaling the NREL 5MW offshore wind turbine [95] and is designed upon proposal of the Technical University of Denmark (DTU) in 2013 [101]. Key parameters proposed by DTU can be seen in Table 2.3. In Figure 2.26, 2.27 and 2.28 the hybrid drivetrain model, the schematic layout of the drivetrain model with relevant nomenclature and the drivetrain topology can be seen.

Table 2.3: Key parameters of the 10MW drivetrain provided by DTU. [101]

Parameter	DTU 10MW Drivetrain Properties
Rated rotor speed	9.6 rpm
Rated generator speed	480 rpm
Gearbox ratio	1:50
Generator inertia about the high-speed shaft	1500.5 kgm2
Equivalent drive-shaft torsional-spring constant	2317.0 MNm/rad
Equivalent drive-shaft torsional-damping constant	9241 MNm/(rad/s)
Electrical generator efficiency	94 %

The main shaft is supported by two main bearings, INP-A and INP-B. Both bearings are tapered roller (TRB) bearings, just as most other bearings, which provide support for axial forces. The HS-A and PLC-B are cylindrical roller (CRB) bearings, which will not provide any support for axial forces. The torque arm supports aim is to improve drivetrain reliability by taking the non-torque loads from the main shaft.

The INP-A and INP-B bearing will take most of the thrust loads and hub mass, where the HS-A and HS-B bearing will take most of the generator loads. Significant loads can occur due to misalignment or movement flexibility.

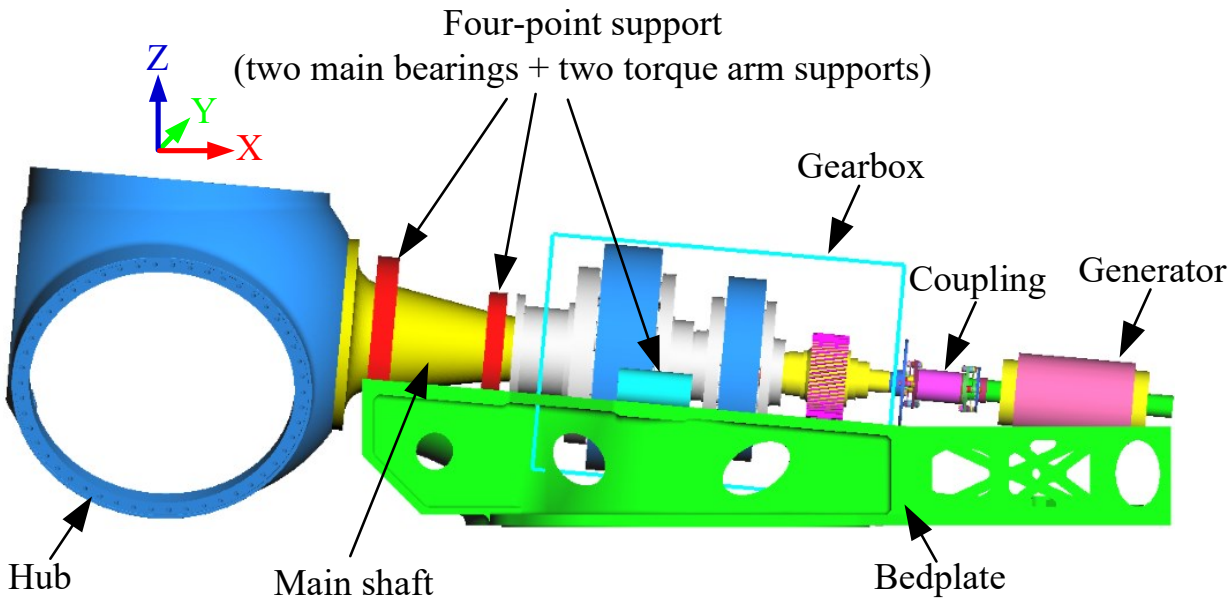

Figure 2.26: 10MW drivetrain MBS model [47].

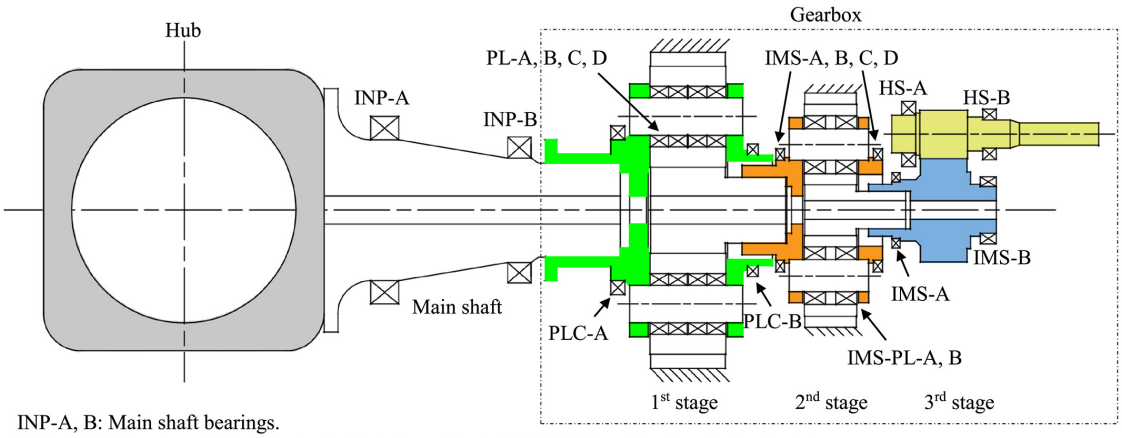

INP-A, B: Main shaft bearings.
PLC-A, B: Planet carrier bearing in the first stage; PL-A, B, C, D: Planet bearings in the first stage.
IMS-PLC-A, B: Planet carrier bearing in the second stage; IMS-PL-A, B: Planet bearings in the second stage.
IMS-A, B: Intermediate shaft bearings in the third stage; HS-A, B: High speed shaft bearings in the third stage.

Figure 2.27: 10MW drivetrain schematic layout [47].

The gearbox connects the low speed shaft to the high speed shaft. The gearbox consists of three main stages: two planetary stages and one parallel stage, which can be seen in Figure 2.28.

The first stage is a planetary stage consisting of five planet gears each supported by four bearings with a gear ratio of 1:4.423. The second stage is a planetary stage consisting of three planet gears with a gear ratio of 1:5.192. The third stage is the parallel stage with a gear ratio of 1:2.179.

The high speed shaft is connected with the third stage of the gearbox and is connected to the generator. The high speed shaft will rotate at 480 rpm at rated wind speed. Using Equation 2.30 the number of poles of the generator can be determined. and further development of the generator can be modelled.

The model is made using the multi-body system (MBS) approach, which is a good way to study the dynamic behaviour of interconnected rigid and flexible bodies.

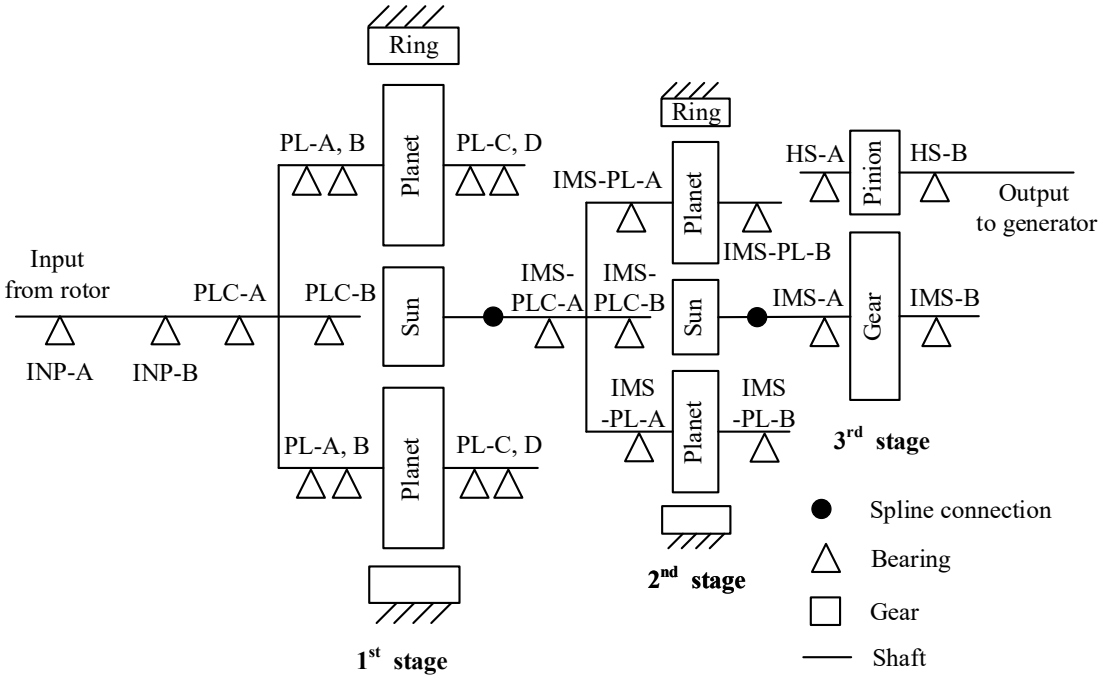

Figure 2.28: 10MW Drivetrain gear and bearing topology [46].

2.14 Drivetrain failure and its influence on Turbine Downtime

Operation and maintenance (O&M) costs constitute to a significant part of the total costs of offshore wind power. Figure 2.29 from Millan et al. (2008) shows that significant downtime for WTs is caused by the gearbox, bearings and the mainshaft, even for land based turbines. Faulstich et al. (2011) [117] also states that the annual downtime for wind farms close to the coast (< 12 km) increases. For wind farms planned at 50 km from shore, availability may decline even further.

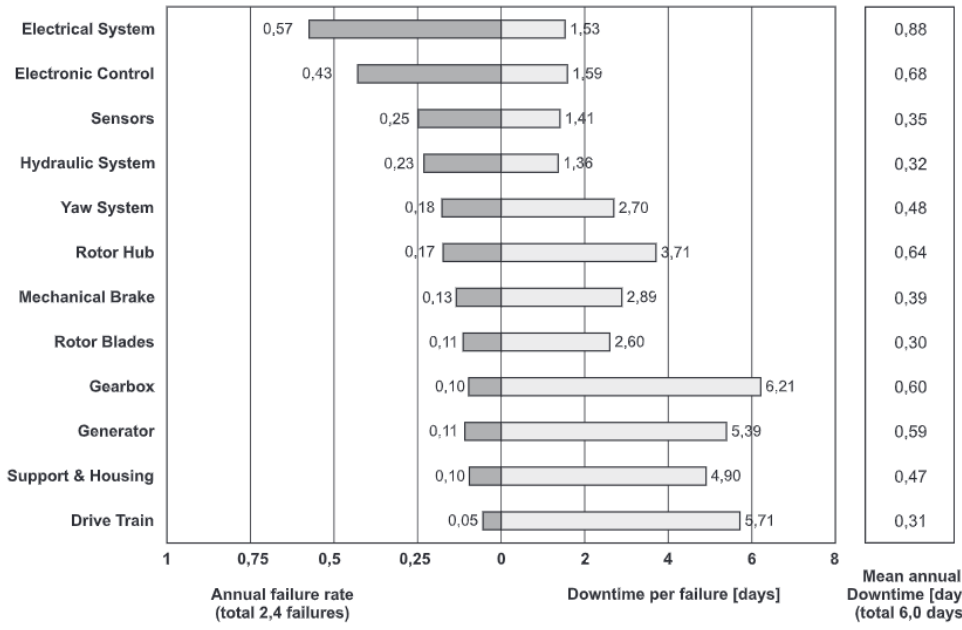

Figure 2.29: Annual failure rate and downtime per failure from the German land based wind turbine failures database [117].

O&M offshore is dependent on the weather window. Boats and helicopters can not perform maintenance work with high sea states and/or wind speeds. This may lead to longer wind turbine downtime [120].

Cuong et al. (2019) [121] presented a model where the LCOE is evaluated as function of WT failure rates and downtime from data shown in Figure 2.30 and Figure 2.31. Offshore and onshore failure rates are discussed in this paper and a clear difference in frequency of failure is found. When individual sub assembly data is combined, the offshore failure rate is roughly three times the weighted average of the onshore failure rate.

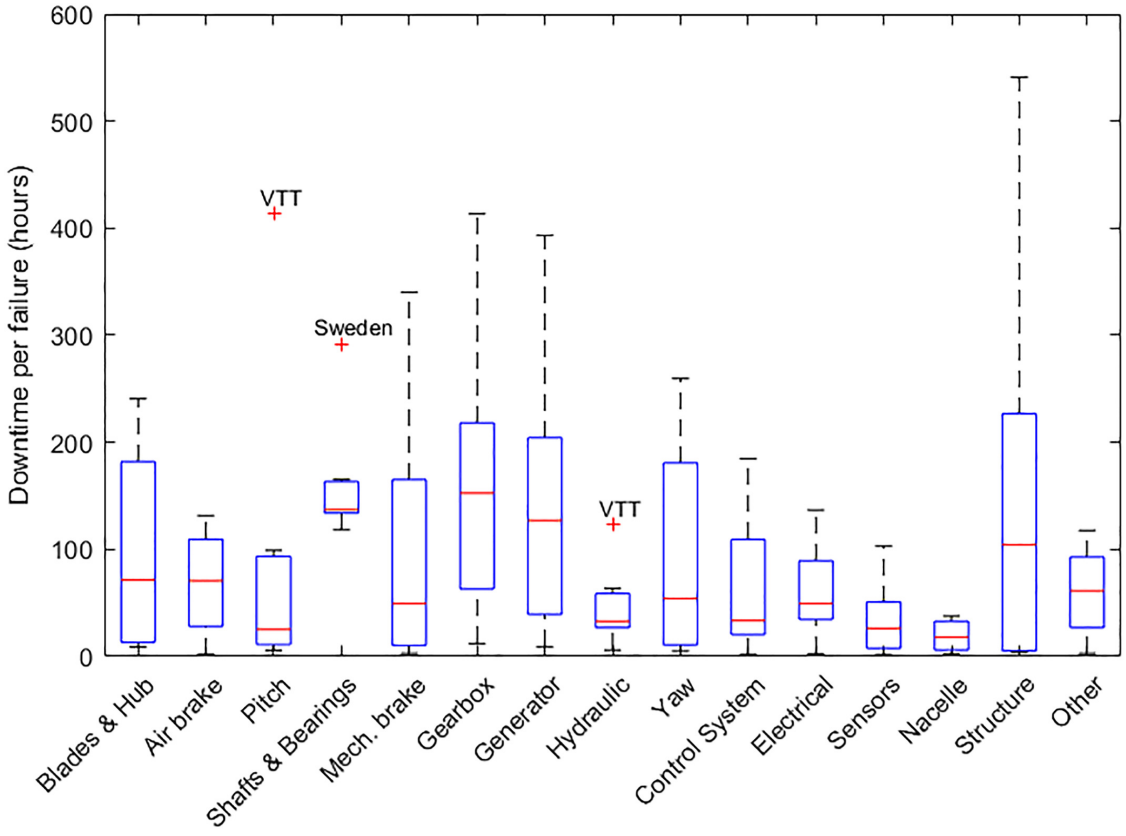

Figure 2.30: Box plot of subassembly failure rates [121].

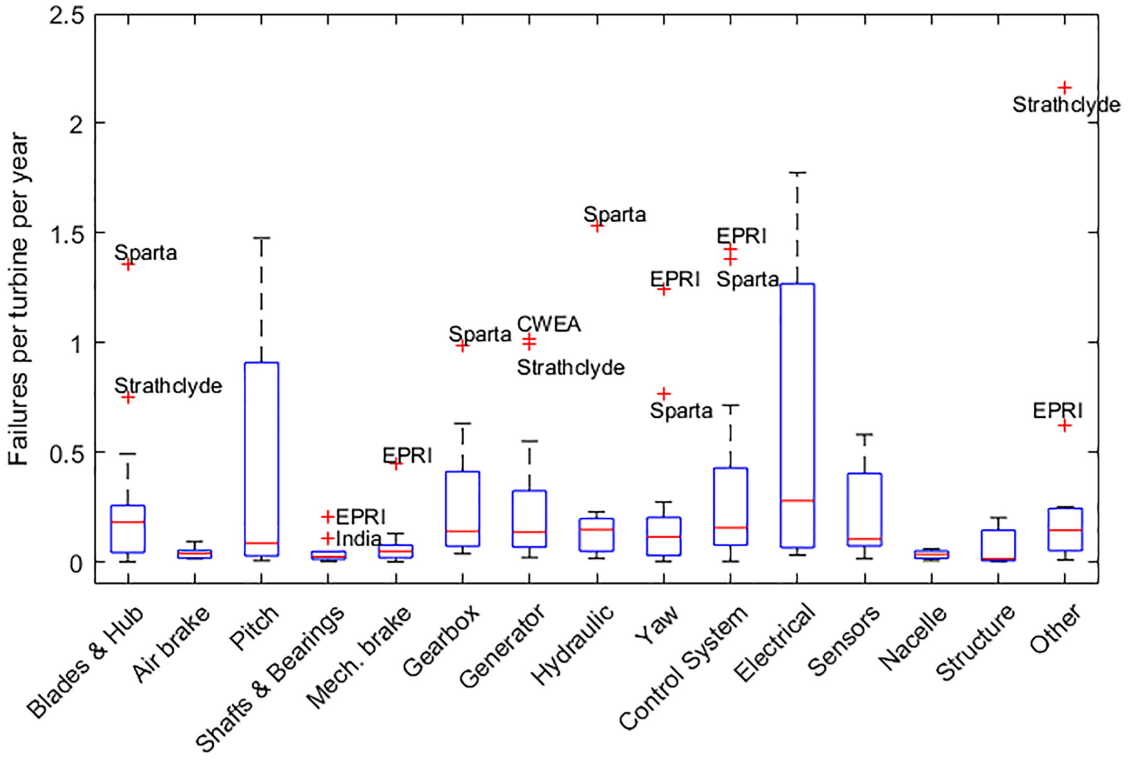

Figure 2.31: Box plot of subassembly downtime [121].

Offshore and onshore downtime can be subdivided into

- Repair time.
- Lead time.
- Logistic delay.

The offshore database (Strathclyde) shows the repair time of Offshore Wind Turbines, which can be seen in Figure 2.32 from [121] where onshore downtime was compared to offshore repair time. It should be noted that repair time and downtime are not the same. The Figure shows that repair time due to gearbox failure takes by far the longest time. Data shows that the average stop time onshore is around 3.9 hours, while average stop time offshore is around 7.7 hours.

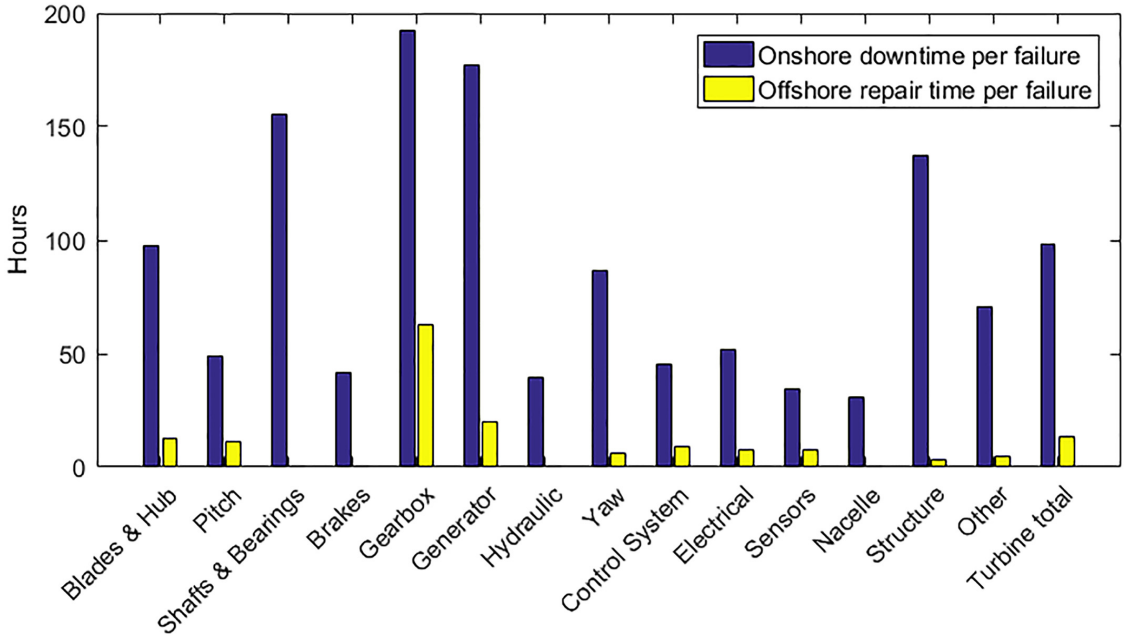

Figure 2.32: Downtime for onshore databases and repair time for offshore databases [121].

Figure 2.33, 2.34 and 2.35 show the failure per turbine per year , the stops per turbine per year and the stop time per event. The data from the Figures will be used to make a cost estimation due to component failure, further discussed in section 2.17.

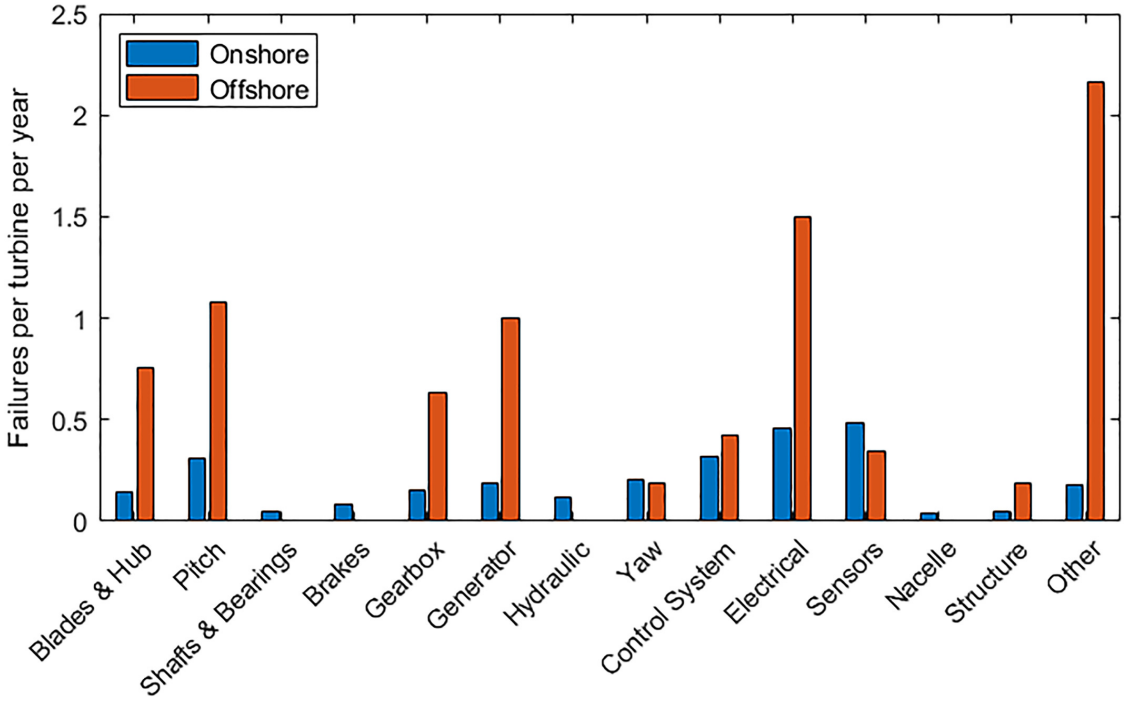

Figure 2.33: Comparison of weighted failure rates between onshore and offshore databases [121].

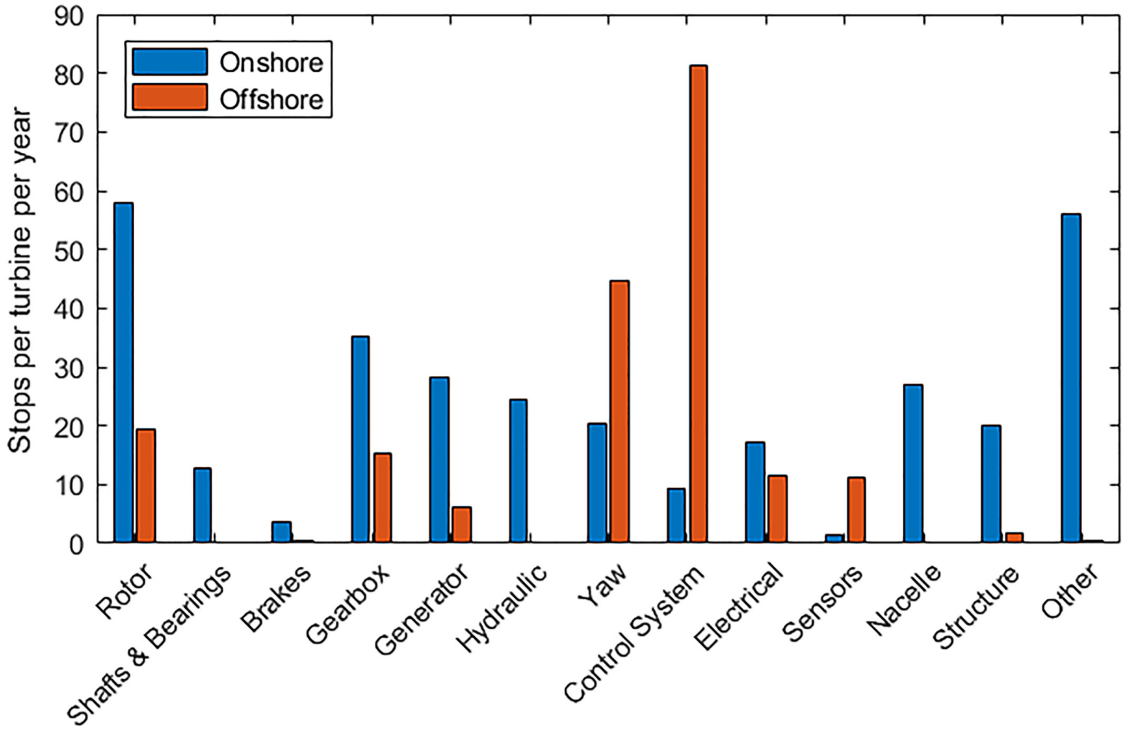

Figure 2.34: Comparison of weighted stop rates between onshore and offshore databases [121].

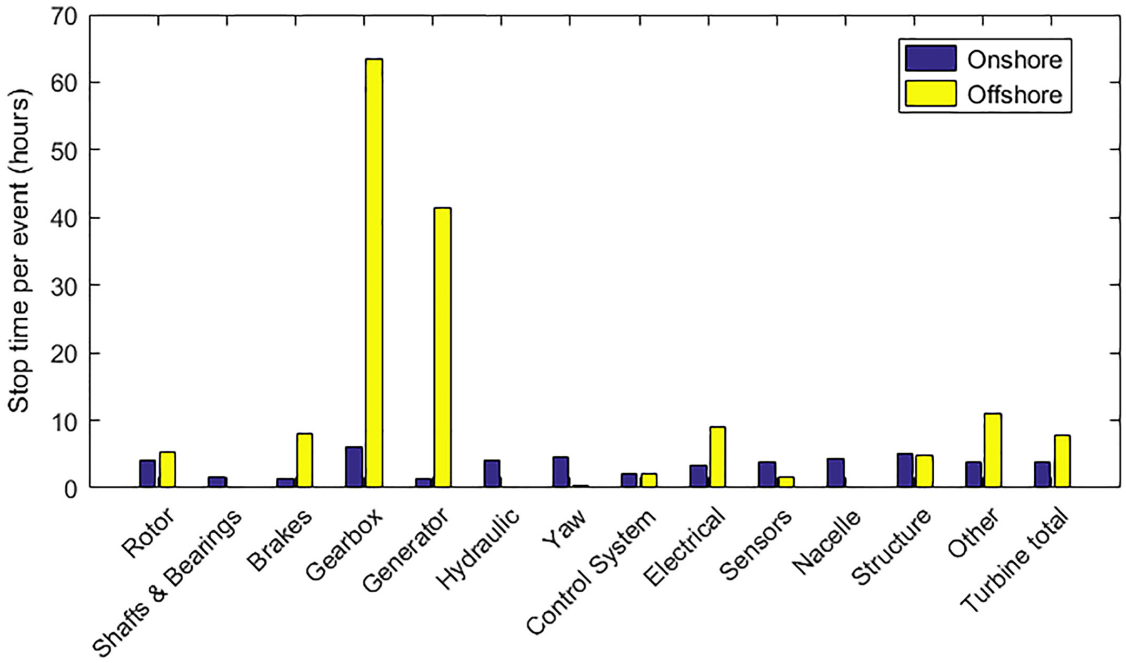

Figure 2.35: Stop time per event for onshore and offshore wind turbines [121].

2.15 Drivetrain Repair Cost and Options

Fischer et al. (2012) [122] states that any failure in the planetary stage requires removal of the gearbox from the nacelle for external repair, resulting in increased vessel and downtime cost. Damage to the bearing can either cause production loss due to friction, complete production loss due to failure, secondary component damage due to increased vibrations and risk of fire due to heat generation.

For certain drivetrain types it is possible to repair the HS shaft inside the turbine nacelle without the need of any external crane. Thus not needing a heavy lift vessel (HLV) [123]. Instead the use of a field support vessel (FSV) can be considered.

The main bearings are both not part of the gearbox, as seen in Figure 2.26 and Figure 2.27. Different downtime is thus considered for failure of the main bearings and failure of the gearbox. Due to the connection of the main shaft to the rotor hub, it is considered that a HLV is needed for repair.

The speed of a HLV and FSV are 12 and 11 knots [124]. Dinwoodie et al. (2015) uses a replacement cost of £334 500 with a repair time of 52 hours using a HLV. When using a FSV, a repair cost of £73 500 is used with a repair time of 26 hours. For further detail on value determination, Appendix A in Dinwoodie et al. (2015) [124] can be consulted.

It should be noted that the turbine used in Dinwoodie et al. (2015) [124] is the Vestas V90 3.0 MW turbines, which is significantly smaller than the Nautilus 10MW FWT. A big portion of the replacement and repair cost is due to the cost of the vessel and labour cost.

Also, the turbine considered in Igba et al. (2014) [123] is the Vestas V90 2.0MW turbine. The high speed shaft components of the 2.0MW WT are significantly smaller than the high speed shaft components of the Nautilus 10MW FWT. It is unknown whether the crane can be used to lift the high speed bearing and the high speed shaft, thus both the HLV and the FSV should be considered for reparation of the high speed shaft bearings.

2.16 Fatigue Calculation

The fatigue damage should be calculated from load time series, which will be explained in the following section. First the desired life and damage formulation for bearing is explained. Then, two stress counting methods are discussed. Further the use of SN-curve counting and the PM rule to calculate total accumulated fatigue damage is explained.

2.16.1 Desired Life and Damage Formulation

Bearing fatigue is calculated using the Lundberg-Palmgren formulation seen in Equation 2.34 and can be rewritten as Equation 2.35 [125, 126].

$$PL^{\frac{1}{a}} = \text{ const.} \tag{2.34}$$

$$LP^a = L_{10}C^a = \text{ const.} \tag{2.35}$$

where

- L is the bearing life.
- P is the dynamic equivalent radial load on the bearing over a given period.
- a is a constant and is 3 for ball bearings and $\frac{10}{3}$ for roller bearings.
- L_{10} is the characteristic basic rating life defined as the number of cycles that 90% of an identical group of bearings achieves, under a certain test conditions, before the fatigue damage appears, which is in this case for pitting damage.

- C is the basic load rating and constant for a given bearing.

The dynamic equivalent radial load P can be calculated using Equation 2.36

$$P = XF_r + YF_a \tag{2.36}$$

where

- X is a constant taken from ISO 281 [127].
- F_r is the radial load.
- Y is a constant taken from ISO 281 [127].
- F_a is the axial load.

Using the LDD counting method in subsection 2.16.2, the SN-curve in subsection 2.16.4 and the PM rule in subsection 2.16.5 the total bearing damage can be found.

2.16.2 Stress cycle counting method : Load Duration Distribution

A method to calculate fatigue damage on gears and bearings is by using the LDD method. The amount of cycles gears and bearings have to endure is significantly higher than that of the structural components of the wind turbine, since every tooth flank, ball or roller contact creates a cycle. The LDD method takes the contact time into account. This method is recommended by IEC 61400-4 [128] and is widely used in gearbox design [52].

Load bins are created using a load time series. These load bins are then converted to stress bins as shown in Figure 2.36.

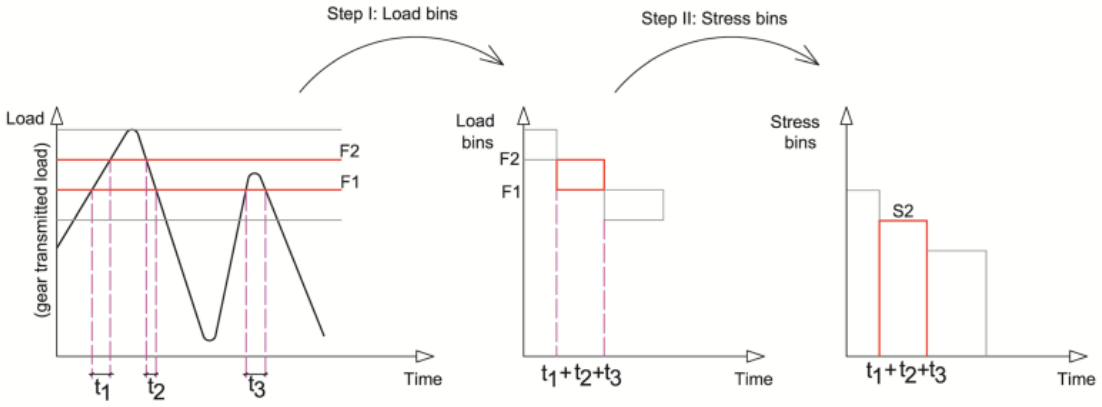

Figure 2.36: Stress and load bin creation from a load time series [52].

Then, the bearing stress cycles should be determined. These cycles are dependent on the external load and the bearing rotational speed, seen in Equation 2.37.

$$n_i = \frac{t_i}{60}\omega_i \tag{2.37}$$

where

- n_i is the number of cycles that occur for stress bin i.

- t_i is the time duration of bin i in seconds.
- ω_i is the rotational speed of the gear or bearing in rpm.

A further in depth explanation can be found in Niederstucke et al. (2003) [129].

Once all stress cycles and the amount of stress cycles for each particular bin are determined, the total damage can be calculated using the PM rule, discussed in subsection 2.16.5.

2.16.3 Stress cycle counting method : Rainflow Counting

The rainflow-counting algorithm is a method to count stress cycles and bin the stress cycles reducing the data from a time series into a stress range histogram, which is a good way to estimate the fatigue life of structural components. Figure 2.37 shows an example of the rainflow counting method on a time series of load fluctuations. The method is as follows:

1. Rainflow starts at the the inside of any peak and can flow until it reaches a maximum or a minimum. Once reaching a maximum or minimum, one cycle is finished.
2. When a rainflow meets a rainflow dropping from above, the rainflow will also be finished and count as one cycle.
3. This will be done for the inside of every peak , resulting in a list of cycle ranges.
4. Finally, binning the cycle ranges will make the cycle data ready for the next step: Calculating relative fatigue damage using the SN-curve and the PM rule [130].

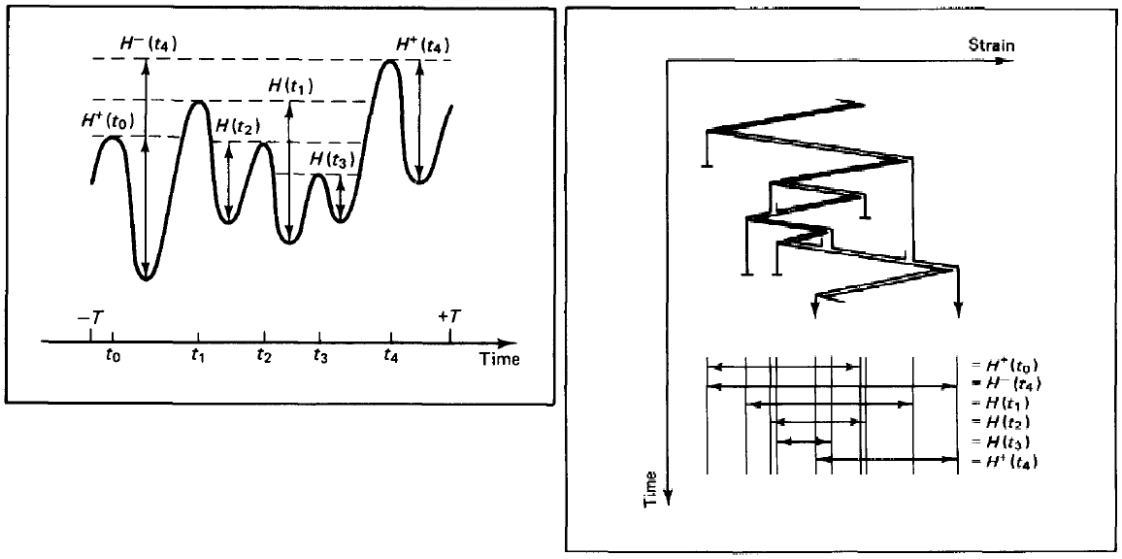

Figure 2.37: example of rainflow counting diagram (right) applied to a load history diagram (left)[130].

Rainflow counting is used in structural fatigue calculations. The drivetrain consists of components that mainly fail due to damage caused by dynamic fatigue, such as pitting. This means that rainflow counting is not considered for drivetrain fatigue calculations. Instead, the LDD method in subsection 2.16.2 should be considered.

2.16.4 Calculating relative fatigue damage using the SN-curve

Having the stress ranges binned from the LDD method or the rainflow counting method, a SN-curve should be used to calculate the relative fatigue per stress range. The properties of the SN-curve are dependent on the material, heat treatment, surface roughness and size of the gears and should be known.

The SN-curve shows the amount of cycles needed for a certain stress range to result into failure. Usually this limit is not reached and a fraction of failure comes out as result. In Figure 2.38 a typical SN-curve can be seen and in Figure 2.39 the corresponding points for the ultimate strength and yield strength in the Stress-strain curve can be seen.

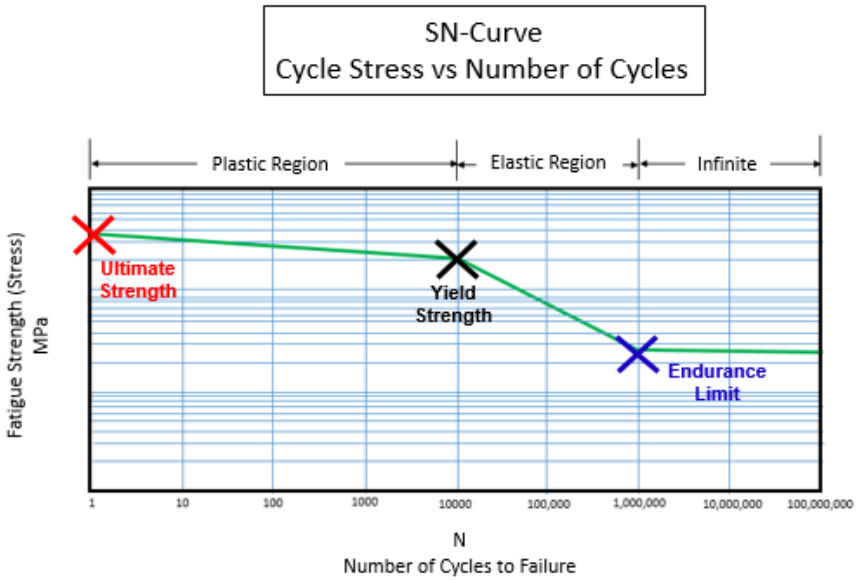

Figure 2.38: Typical SN curve for a steel alloy.[6]

[6] https://community.sw.siemens.com/s/article/what-is-a-sn-curve[Visited on the 9th of January 2020]

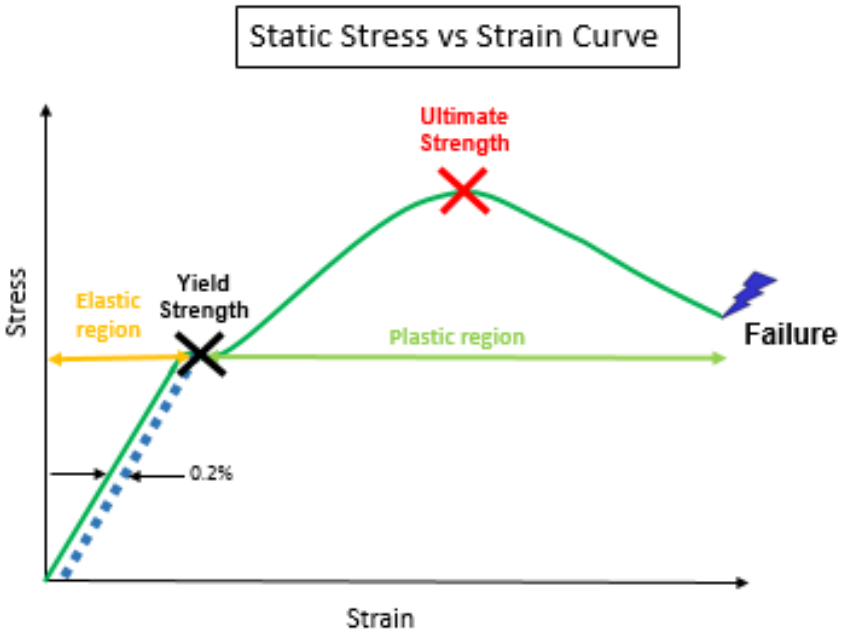

Figure 2.39: Typical stress-strain curve for a steel alloy.[7]

Every single stress cycle results in a relative amount of fatigue damage. Using the PM rule, the accumulated fatigue damage can be calculated.

2.16.5 Calculating the total fatigue damage using the Palmgren-Miner rule

The PM rule is a widely used cumulative damage model. It assumes that all different stress ranges can be summed up to calculate the total fatigue damage done to the structure or component.

$$D = \sum_{i=1}^{k} \frac{n_i}{N_i} \tag{2.38}$$

where

- D is the total accumulated damage.
- k is the total amount of bins with different stress ranges.
- n_i is the number of cycles that occur for a stress range σ_i.
- N_i is the total amount of cycles causing failure for a stress range σ_i.

Failure occurs when the damage reaches a value of 1. Usually 1 hour simulations are used.

2.16.6 Fatigue damage limit for offshore wind turbines

Nejad et al. (2017) [131] shows that fatigue damage of the INP-B bearing can cause a significant damage increase of the PLC-B bearing. Thus letting the bearings reach a fatigue

[7] https://community.sw.siemens.com/s/article/what-is-a-sn-curve[Visited on the 9th of January 2020]

damage value of 1, where failure occurs, is not desirable. ISO 20816-1 [132] shows four evaluation zones :

- Zone A : new machines.
- Zone B : acceptable zone for long-term operation.
- Zone C : unacceptable for long-term operation.
- Zone D : can cause severe damage.

Nejad et al. (2017) [131] shows that vibrations in zone A/B for the INP-B bearing do not necessarily indicate that no damage increase occurs in the PLC-B bearing. Since wind turbines run for a significant amount of time, Zone A or B should be used as threshold for a healthy wind turbine.

Igba et al. (2016) [133] has shown that RMS and peak values are good indicators of the gearbox health if used properly. They however also state that the changes in RMS vibrations are only sensitive to high shaft revolutions and can thus be used for monitoring the intermediate and high speed shaft.

ISO 10816-21 [134] recommends vibration limits for onshore WTs smaller than 3 MW, while Igba et al. (2016) [133] shows that lower limits than the ISO values in ISO 10816-21 [134] should be used.

For now a degradation level of 50% is used, which gives vibrations around zone B/C for PLC-B [131]. This degradation level value will be used for each bearing, including PLC-B.

2.17 Cost calculation on Wind Farm level

Wind Farm profit can be found by first calculating the AEP and then multiplying the AEP with the price of energy. A representative energy price can be found on `https://www.epexspot.com/en` or by looking at the power purchase agreement (PPA) the wind farm has signed. The representative wholesale market price has large annual, seasonal, weekly and daily fluctuations.

2.17.1 Wind Farm Power Calculation

Power production for a single turbine has been discussed in section 2.6. On wind farm level the power production can be found using Equation 2.39, where n represents the number of turbines each with their own inflow velocity and power coefficient.

$$P_{tot} = \sum_{i=1}^{n} C_{P,i}(\lambda_i, \beta_i) \frac{1}{2} \rho A V_i^3 \tag{2.39}$$

2.18 Model Verification

To verify the simulation results, different results from FAST.Farm, OpenFAST and the 10 MW drivetrain model will be discussed and compared to literature. Simulations are ran to compare floater results to fixed results and turbulent wind field results to uniform wind field results with relevant literature.

From FAST.Farm and OpenFAST the following results will be verified:

- Simulation transient length.
- Wind speed.
- Turbulence Intensity.
- Wake evolution.
- Atmospheric boundary layer.
- Sea state.
- Floater motions.
- Power production.
- Global loads.
- Yaw angle.
- Blade pitch angle.

From the DTU 10MW drivetrain model the following results will be verified:

- Absolute bearing damage.
- Relative bearing damage.

Further more different repair cases will be considered, which will be further elaborated in section 3.8.

2.19 Model Validation

2.19.1 Mann Turbulence Model

The Mann turbulence model is validated in Mann et al. (1994) [44] and in Chougule et al. (2018) [135]. The four main parameters, discussed in section 2.2, are compared to data acquired on hub height level of the WT (100 m) at the National Centre for wind Turbines site at Høvsøre. The model predicts coherences and phases and is then compared to the field measurements. For further elaboration on the validation of he Mann Turbulence Model, Chougule et al. (2018) can be studied.

2.19.2 FAST.Farm

FAST.Farm uses the DWM model. The DWM model, developed at DTU, is optimized using experimental data from laboratory results, mentioned in Larsen et al. (2007) [41] and validated in the EU research project TOPFARM [136]. In section 2.5 more validation regarding the DWM model can be found. FAST.Farm has calibrated 18 parameters in the "wake dynamics" and "ambient wind and array effects" modules, which can be seen in Table 2 of Doubrawa, Annoni and Jonkman (2018) [137]. In Jonkman et al. (2018) [138] FAST.Farm has been further validated against SOWFA and showed that the thrust, the power production and the wake meandering (advection, evolution and merging) behavior across different atmospheric conditions are reasonably accurately predicted.

2.19.3 Nautilus 10MW FWT model in OpenFAST

The DTU 10MW WT is designed by geometrical upscaling the NREL 5MW WT as discussed in subsection 2.10.1. The blades are also upscaled and performance is predicted using BEM. Further optimization and validatation is done using 3D CFD calculations [101]. Decay tests are done to determine the natural frequencies. Furthermore, floater responses on regular waves, step uniform wind, irregular waves, turbulent wind and ultimate and extreme conditions are determined [56].

2.19.4 DTU 10MW Drivetrain Model

The DTU 10MW drivetrain model [46, 47] is a high-fidelity model based on upscaling the NREL 5MW drivetrain model [95]. NREL laboratory has multiple dynamometers, being able to perform research validation on drivetrains ranging from 1kW to 5MW [139]. Design is based on design loads and criteria recommended by international standards and is compared with the simplified model proposed by DTU. Further verification is done with Campbell diagrams [140] and the modal energy distribution to evaluate drivetrain resonance.

2.20 Floater Effects On Wake Steering And Axial Induction Control

To verify the power production and global loads on the floater, a similar simulation is ran where the floater is fixed. All platform motions are set to zero.

3 | Methodology of a two turbine Set-Up

In the following chapter the methodology of the two turbine set-up will be discussed, starting with the FAST.Farm model setup. The same turbulent wind field is used for each simulation case, but a different arrangement is used based upon findings in literature, which has been discussed in section 2.8 and 2.9.

Figure 3.1 shows the overall methodology of the two turbine set-up in the turbulent wind field. The Nautilus 10MW FWT is used with environmental conditions, arrangement and spacing determined by previous literature.

Test cases are determined for the wake steering and wake meandering arrangement. Simulations are run resulting in the global responses. Tower top global responses are used to run the local drivetrain model, while power production results are used to determine the total power production. The local drivetrain model results in local drivetrain responses on bearings. Bearing fatigue theory is applied resulting in accumulated fatigue damage results for considered bearings.

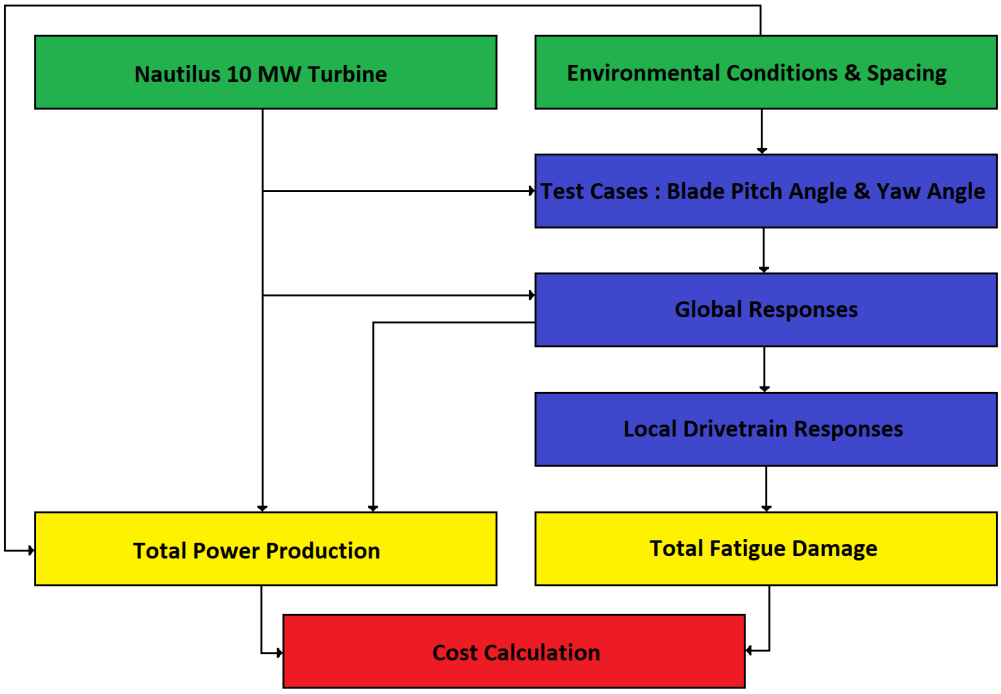

Figure 3.1: Scope and methodology for the master thesis.

In section 3.1 and 3.2 the FAST.Farm and OpenFAST model inputs are discussed.

In section 3.3 the environmental conditions are discussed and in section 3.4 the test cases are shown.

In section 3.6 the decoupled analysis method is explained and in section 3.7 and 3.8 the bearing fatigue calculation and cost methodology are discussed.

3.1 FAST.Farm model

3.1.1 Wind Field Setup

As discussed in section 2.2, the Mann turbulence model will be used to create the ambient wind field. The wind field size is based on the wind field size of a paper released by Wise et al. (2020) [110] and is X $\times$ Y $\times$ Z = 10 km $\times$ 952.5 m $\times$ 472.5 m. The low-resolution domain ΔX, ΔY and ΔZ is 1.376 m, 7.5 m and 7.5 m with a timestep of 2 s [75]. The high-resolution domain has an identical spacial resolution, but a different timestep of 0.125 s [141]. The reference height, z_{mid} is half the wind field height, Z.

The number of high resolution wind field nodes around the WT NX_{high}, NY_{high} and NZ_{high} are taken to be 102, 64 and 32 nodes, which results in a high resolution wind field of the dimensions of $X_{high} \times Y_{high} \times Z_{high}$ = 139 m $\times$ 472 m $\times$ 232.5 m where the high resolution wind field starts 80 m in upwind direction from each individual turbine. The remaining nodes of the wind field have a low resolution.

The TI of the Mann Turbulence Field is calculated using IEC61400-1(2005) and turns out to be 0.203 for a mean wind speed of 8 m/s.

$\alpha\varepsilon^{2/3}$, L and Γ are found to be 0.144 $m^{4/3}s^{-2}$, 33.6m and 3.9, respectively. The simulation time is 4000s, with a 400s transient and an output timestep of 0.025s.

3.1.2 Wake Steering Arrangement

The wake steering arrangement has been determined by the article of Stoyan Kanev [7] and the PhD thesis of Pieter Gebraad [142]. Pieter Gebraad used a spacing between the two turbine case of 7 rotor diameters. By determining the minimum distance available between the upwind and downwind Nautilus 10MW FWT due to mooring line length, a minimum rounded off spacing of 7 rotor diameters was found. From Figure 2.15 the optimal wake overlap for maximum power gain of the downwind WT is determined. Using trigonometry, a turbine arrangement is determined and can be seen in Table 3.1.

Table 3.1: Turbine hub coordinates above SWL in the turbulent wind field for the wake steering arrangement.

Turbine number [-]	X [km]	Y [m]	Z [m]
1	1	-89.15	119
2	2.2449	0	119

3.1.3 Wake Meandering Arrangement

For the wake meandering arrangement it is decided that the downwind turbine should be exactly behind the wake of the upwind turbine, which is based on literature discussed in section 2.9.

Table 3.2: Turbine hub coordinates above SWL in the generated wind field for the wake meandering arrangement.

Turbine number [-]	X [km]	Y [m]	Z [m]
1	1	0	119
2	2.2481	0	119

3.2 OpenFAST model

The WT model used in OpenFAST is the DTU 10MW reference wind turbine which is supported by the nautilus semi-submersible floater, discussed in subsection 2.10.3 and shown in Figure 2.22 and 2.24.

3.3 Environmental Conditions

A mean wind speed at hub height, u_{hub}, of 8m/s is chosen. Since turbulent wind fields are used, a part of the simulation wind speed will be higher than 8m/s. In order to avoid above rated wind speeds (11.4m/s for the DTU 10MW WT) a wind speed far below rated is chosen. Wind turbine class B is selected and the power law exponent, α, is taken as 0.14. The value of the turbulence standard deviation in the positive wind direction, σ_u, is determined from Equation 2.3.

The significant wave height, H_s, is determined using Beaufort scale linear interpolation, whereas the corresponding peak period, T_p, is found using IEC61400-3 [69], also shown in section 2.3. The resulting sea state gives H_s = 2m and T_p = 7.4s. The current is not taken into account.

3.4 Test Cases

3.4.1 Wake Steering Control

Four different yaw angles are chosen for the upwind WT. The yaw angles are chosen by first running multiple simulations with a yaw step of 5 degrees to determine the yaw angle, γ, where increased power production results are found. The resulting test cases can be found in Table 3.3. The downwind WT has ideal control settings to maximize power production, meaning no blade pitch or yaw change.

Table 3.3: Considered test cases of WT 1.

Test case	**Blade pitch angle [°]**	**Yaw angle [°]**
TC_0	0	0
TC_1	0	5
TC_2	0	7
TC_3	0	8
TC_4	0	10

3.4.2 Axial Induction Control

Similar to subsection 3.4.1, different pitch angles are chosen for the upwind WT, determined by running multiple simulations with a blade pitch step of 2 degrees, since the blade pitch is more sensitive than turbine yaw for power production. The blade pitch step size turned out to be too large and thus a blade pitch step size of 1 degree is used, which can be seen in Table 3.4. Similar to subsection 3.4.1, the downwind WT has ideal control settings to maximize power production.

Table 3.4: Considered test cases of WT 1.

Test case	Blade pitch angle [°]	Yaw angle [°]
TC_5	0	0
TC_6	1	0
TC_7	2	0
TC_8	3	0
TC_9	4	0

3.5 Power Calculation

The power production of WT_1 and WT_2 is averaged over time and summed up to find the total power production for each test case.

3.6 Decoupled Analysis Method

Each individual test case (TC_0-TC_9) is run in FAST.Farm, resulting in time series results of floater motions, global loads, the sea state (H_s,T_p), blade pitch angles, the yaw angle, rotor angular velocity and the power production.

Low speed shaft (LSS), intermediate speed shaft (ISS) and high speed shaft (HSS) axial and radial forces are calculated using the global loads. First global loads are used as input for the DTU 10MW Drivetrain model. The Drivetrain model is ran with a timestep of 0.025s. Figure 2.28 shows the gears and bearings of the drivetrain model.

To determine bearing fatigue damage, angular velocity time series results and axial and radial time series results are needed.

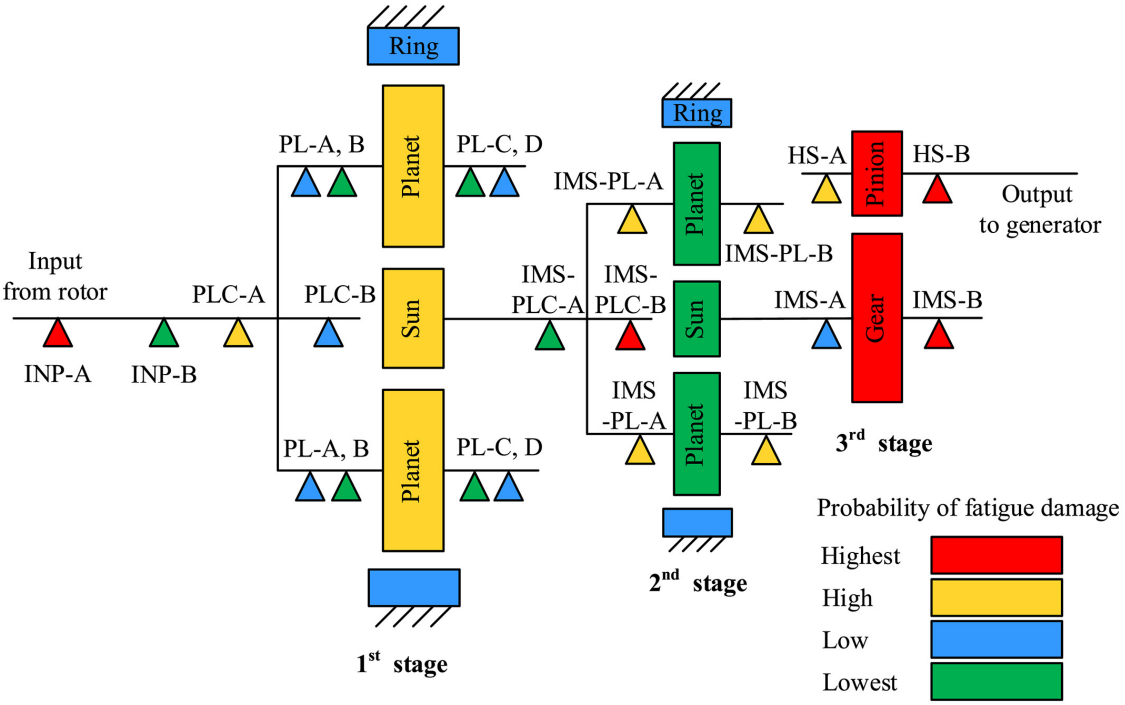

Figure 3.2: 10MW Drivetrain topology with added vulnerability map [47].

3.7 Bearing Fatigue Calculation

The bearings selected for the fatigue calculation are decided on the drivetrain vulnerability map from Wang et al. 2020 [47]. The bearings that are part of the HSS, the ISS and the LSS are selected. PL-A, B, C and D are not considered, just as IMS-PL-A and B.

The bearing fatigue is calculated using Equation 2.36, where Equation 3.1 is used to calculate the absolute radial force. Values for X and Y can be taken from Table 3.5, which are found in Wang et al. (2020) [47] and are taken from ISO 281 [127]. By then using the LDD counting method, explained in subsection 2.16.2 the damage bins are created. By rewriting Equation 2.35 to determine N_i and using the PM rule (subsection 2.16.5, Equation 2.38) total accumulated damage on the bearings stated in Table 3.5 is calculated.

$$F_r = \sqrt{F_z^2 + F_y^2} \tag{3.1}$$

Table 3.5: Fatigue parameters of considered bearings.

Stage	Bearing	X	Y	a	C
Main shaft	INP-A	1	0	10/3	5.6432E6
	INP-B	1	0	10/3	4.5774E6
First stage	PLC-A	1	1.18	10/3	3.65E6
	PLC-B	1	0	10/3	1.65E6
Second stage	IMS-PLC-A	0.4	1.804	10/3	5.6315E6
	IMS-PLC-B	0.4	1.547	10/3	5.4393E6
	IMS-A	1	0	10/3	4.1232E6
	IMS-B	1	0	10/3	2.8E6
Third stage	HS-A	1	0	10/3	2.16E6
	HS-B	1	1.24	10/3	3.79E6

Accumulated damage results for each bearing can be found in subsection 5.2.3 and 5.3.3.

3.8 Cost Calculation

The cost calculation is dependent on the power calculation, the fatigue calculation and the price of energy. The price of energy is determined from the European Power Exchange (EPEX SPOT) found on `https://www.epexspot.com/en` and `https://www.icis.com/explore/about/methodology/`. Huge fluctuations on the energy price are found, thus a list of different energy prices is used.

Wholesale market prices are taken from Great Britain (GB). Hywind Scotland, the first floating wind farm in the world, is connected to the grid of GB and thus serves as a good reference for the wholesale market price.

In Figure 3.3 the wholesale market price of energy can be found. The data is partly averaged, to reduce peaks. Further unaveraged data can be found on `https://www.ofgem.gov.uk/system/files/docs/2019/11/20191030_state_of_energy_market_revised.pdf`. Fluctuations from £35,- to £68,- GBP per MWh are found from 2010 till 2019. The GBP/euro exchange rate is 1.14 which is found on `https://www.morningstar.be/be/` (11/05/2020) resulting in an energy price range from €39,9 to €77,5. The price

of energy at 23/04/2020 was found to be €25,67/MWh on https://www.epexspot.com/en. It is assumed that this is a large deviation due the COVID19 Pandemic and is thus not taken as lower limit.

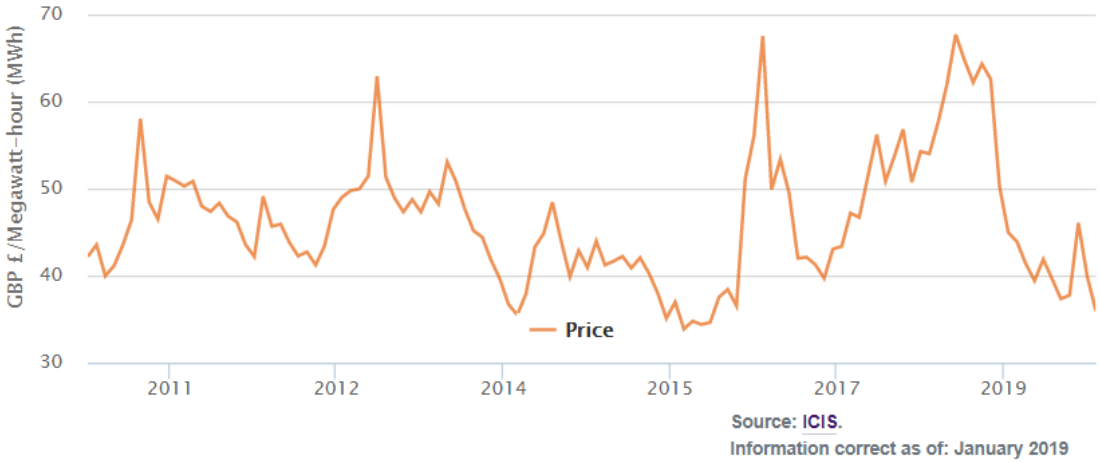

Figure 3.3: British energy price from https://www.icis.com/explore/about/methodology/.[1]

The energy price is taken to range from $40,-$ to $75,-$ with a step size of $5,-$.

Equation 3.3-3.5 are used to determine the relative profit. For this profit only power production and drivetrain failure is considered.

$$Prod = P_{tot} PoE \tag{3.2}$$

$$DT_{cost} = T_{dur} Prod + F_{cost} \tag{3.3}$$

$$DT_{cost,rel} = DT_{cost} PoF \tag{3.4}$$

$$Prod_{rel} = Prod - DT_{cost,rel} \tag{3.5}$$

Where

- $Prod$ is the total profit generated from energy in $\frac{euro}{hour}$ for a given energy price.
- P_{tot} is total power produced of the 2 turbine set-up in MWh.
- PoE is the price of energy in $euro/MWh$.
- DT_{cost} is the cost of downtime due to bearing failure in $euro$.
- T_{dur} is the downtime due to failure for either the gearbox or the main shaft bearing (INP-A and INP-B) in $hour$ found in Table 3.6.

[1] https://www.ofgem.gov.uk/data-portal/electricity-prices-day-ahead-baseload-contracts-r on the 11th of May 2020]

- F_{cost} is the cost of failure in *euro* found in Table 3.6.
- $DT_{cost,rel}$ is the cost of downtime due to bearing failure in $euro/hour$.
- PoF is the probability of failure in % of the threshold value, which results are found in section 3.7.
- $prod_{rel}$ is the generated money subtracting the loss per hour in $euro/hour$ due to failure cost per hour of the gearbox and the shaft bearings.

Limited data on offshore failure is available yet, especially regarding FWTs. Based on section 2.14 an estimation of the offshore downtime is made.

Cuong et al. (2019) [121] states in the conclusions that the criticality of subassemblies is quite consistent for different data sources : *"In terms of downtime, the gearbox, generator, blades and hub, and drivetrain are the four most critical subassemblies for both onshore and offshore WTs."*.

It is also stated that downtime per stop of an offshore WT is approximately double that of an onshore WT. This is however not the downtime per component failure.

Lead time is based on the speed of the field support vessel (FSV) and the heavy-lift vessel (HLV) from Dinwoodie et al. (2015) [124] and the distance between Aberdeen and the Hywind Scotland Pilot Park found on `https://www.equinor.com/en/news/hywindscotland.html`.

Downtime per failure for the gearbox is based on the repair time over downtime ratio found in Cuong et al. (2019) [121].

For the drivetrain, no offshore repair time was available, thus a different method is used. Cuong et al. (2019) states that downtime per stop of an offshore WT is approximately double that of an onshore WT. This and the repair time over downtime ratio are used to calculate the offshore repair time.

The failure cost is taken for Dinwoodie et al. (2015) [124].

The damage treshold for repair is set at 0.5 [131], elaborated in subsection 2.16.6.

Table 3.6: Cost estimation due to a major repair or major replacement.

	Drivetrain : INP-A, INP-B	**Gearbox**
Downtime per failure onshore [hour] [117]	137	149
Repair time offshore [hour] [121]	54.8	63
Repair time/downtime [-] [121]	20%	20%
Downtime per failure offshore [hour]	274	315
Damage threshold [-] [131]	0.5	0.5
Failure cost [euro] [124]	374640	374640

The high speed shaft can be considered as part of the gearbox or as part of the drivetrain both giving different failure cost and downtime as discussed in section 2.15. These two cases are both considered and can be seen in Table 3.7. Repair case (RC) 1 is the repair

case where the high speed shaft is considered to be part of the drivetrain, while repair case 2 is the repair case where the high speed shaft is considered to be part of the gearbox.

Wang et al. (2020) [47] states that the fatigue damage of the INP-A bearing exceeds the limited value of 1 for a lifetime of 20 years and states that a custom bearing should be manufactured. When a custom bearing is manufactured, fatigue damage results could become very different.

Another case is considered where INP-A fatigue damage is not taken into account. Four different cases are considered for wake steering and axial induction control separately. Repair case 3 and 4 both do not take INP-A damage into account, where repair case 3 considers the high speed shaft to be part of the drivetrain and repair case 4 considers the high speed shaf to be part of the gearbox.

Table 3.7: Cost estimation for the high speed shaft considering the high speed shaft as part of the drivetrain (RC_1/RC_3) or the high speed shaft as part of the gearbox (RC_2/RC_4).

	HSS (drivetrain)	**HSS (gearbox)**
Downtime per failure onshore [hour]	137	149
Repair time offshore [hour]	54.8	63
Repair time/downtime [-]	20%	20%
Downtime per failure offshore [hour]	274	315
Damage threshold [-]	0.5	0.5
Failure cost [euro]	82320	374640

Table 3.8: Considered repair cases for the cost calculation.

Repair case	**INP-A fatigue considered**	**HSS calculation**
RC_1	Yes	Gearbox
RC_2	Yes	Drivetrain
RC_3	No	Gearbox
RC_4	No	Drivetrain

4 | Wake Steering On Larger Farm Level

Various literature shows an increase in power production for induction and wake steering control in large wind farms. The increase might be significantly larger for farms with larger rows of aligned wind turbines. Thus a four wind turbine wind farm case is carried out. Both arrangements for wake steering and axial induction control are discussed in subsection 4.2.1 and subsection 4.2.2. The test cases, similar to the test cases for the two wind turbine turbulent set-up, are discussed in subsection 4.3.1 and subsection 4.3.2.

4.1 Steady Wind versus turbulent wind

Due to FAST.Farm encountering a fatal error for for farms consisting of more than 2 WTs while using a turbulent wind field, a different approach is found to increase the wind farm size where the Mann turbulence field is replaced by a steady wind field.

The main difference between the Mann turbulence field and the steady wind field, is the lack of turbulence in the steady wind field. This will result in less wake mixing . Further more, a steady wind field does not provide representative forces on the wind turbine and the gearbox, due to limited force fluctuations on the turbine, thus fatigue will not be considered for the simulations done in the steady wind field.

For the two wind turbine case, a transient of 400 seconds is considered. For the four wind turbine case, a transient of 1000 seconds is considered.

4.2 Arrangement

4.2.1 Wake Steering Arrangement

For the four wind turbine set-up a similar spacing in X and Y as the spacing used for the two wind turine set-up is considered. The set-up can be seen in Table 4.1.

Table 4.1: Turbine hub coordinates above SWL in the generated wind field for the four wind turbine wake steering arrangement.

Turbine number [-]	X [km]	Y [m]	Z [m]
1	1	-133.725	119
2	2.2449	-44.575	119
3	3.4898	44.575	119
4	4.7347	133.725	119

4.2.2 Axial Induction Control Arrangement

For the four wind turbine set-up a similar spacing in X and Y as the spacing used for the two wind turine set-up is considered. The set-up can be seen in Table 4.2.

Table 4.2: Turbine hub coordinates above SWL in the generated wind field for the four wind turbine wake meandering arrangement.

Turbine number [-]	X [km]	Y [m]	Z [m]
1	1	0	119
2	2.2481	0	119
3	3.4962	0	119
4	4.7443	0	119

4.3 Test Cases

4.3.1 Wake Steering Control

The test cases for wake steering control can be seen below in Table 4.3. Two test cases are added for $\gamma = 15^\circ$ and $\gamma = 20^\circ$.

Table 4.3: Considered test cases of turbine 1 for the two turbine set-up and turbine 1, 2 and 3 for the four turbine set-up.

Test case	Blade pitch angle [°[	Yaw angle [°]
TC_0	0	0
TC_1	0	5
TC_2	0	7
TC_3	0	8
TC_4	0	10
TC_{10}	0	15
TC_{11}	0	20

4.3.2 Axial Induction Control

The test cases for axial induction control can be seen below in Table 4.4 and 4.5. The test cases are identical to the test cases of the turbulent wind field, where for the 4 wind turbine case the baseline test case is changed to a blade pitch angle of 0.125°, since WT_3 behaviour around 0° gives unreliable results.

Table 4.4: Considered test cases of turbine 1 for the two turbine set-up.

Test case	Blade pitch angle [°[	Yaw angle [°]
TC_5	0	0
TC_6	1	0
TC_7	2	0
TC_8	3	0
TC_9	4	0

Table 4.5: Considered test cases of turbine 1,2 and 3 for the four turbine set-up.

Test case	**Blade pitch angle [°[**	**Yaw angle [°]**
TC_{12}	0.125	0
TC_6	1	0
TC_7	2	0
TC_8	3	0
TC_9	4	0

4.4 Methodology

The power production (P_{out}), thrust (F_x), torque (M_x) and overturning moment (M_y) of TC_0-TC_9 will be compared for the turbulent wind field case and steady wind case. For an energy price ranging from 40 to 75 euro per MWh, the profit relative to the baseline test case will be calculated. The wake steering and axial induction control results will be discussed and a conclusion is drawn on the effectiveness of wake steering and axial induction control in low turbulent wind fields.

5 | Results and Analysis

In the following chapter the results are presented and discussed. First the model results are verified in section 5.1. Then the wake steering and axial induction results of the turbulent and uniform wind field are discussed in section 5.2 and 5.3 respectively.

5.1 Verification

For each test case consisting of two WTs the first 400 seconds are not used, since the wake is not fully developed before $t = 400s$. For each test case consisting of four WTs the first 1000 seconds are not used, for the same reason. Visualisation toolkit (VTK) results at $t = 400s$ for the two WT case and $t = 1000s$ for the four WT case are studied and it is concluded that the wakes are fully developed for the test cases.

The TI and the wind speed of the turbulent and uniform wind field have been verified by taking the average and standard deviation of the wind speed at $z = 119m$ in the main wind direction over the full simulation length. The mean and the standard deviation of five time series were taken and the wind speed and TI results are averaged resulting in a mean wind speed and TI for the turbulent and uniform wind field of $7.92m/s$, $8.00m/s$, 0.2013 and 0 respectively, which is a 1%, 0%, 0.8% and 0% deviation respectively.

The wind speed increase in the ABL has been verified using VTK results for turbulent and uniform wind fields and results show a clear increase in wind speed with an increase in height.

The sea state has been verified with FFT results. T_p is found to be around $7.7s$, a deviation of 3.8%.

The blade pitch angle of each axial induction control case has been checked. No deviation from the specified angle is found.

5.1.1 Yaw Error For Floating Wind Turbines

For each test case, a floating wind turbine is used. A floater, unlike a bottom fixed WT, can rotate around its Z-axis (yaw axis). This can either lead to a decrease or an increase in total yaw, resulting in a change in power production.

Table 5.1 shows the control yaw, which yaws the yaw system of the wind turbine and the platform yaw. Adding both yaw angles together results in the total tower top yaw, which causes the wake to deflect. The results show that the tower top yaw angle is around 7% smaller than the control yaw angle, which increases slowly. There is however a mean deviation of 0.10° for TC_0. Taking this deviation as baseline angle, a constant yaw deviation of 8.8% is found. This can be explained by mooring stiffness and corrective torque causing the WT to yaw back to its original position.

Table 5.1: Control yaw, platform yaw, tower top yaw and the deviation of the tower top yaw from the control yaw in %.

Test case	Turbine number	Control yaw [°]	Platform yaw [°]	Tower top yaw [°]	Deviation [%]
$\mathbf{TC_0}$	$\mathbf{WT_1}$	0	0.10	0.10	-
$\mathbf{TC_1}$	$\mathbf{WT_1}$	5	-0.34	4.66	6.72
$\mathbf{TC_2}$	$\mathbf{WT_1}$	7	-0.51	6.49	7.27
$\mathbf{TC_3}$	$\mathbf{WT_1}$	8	-0.60	7.39	7.51
$\mathbf{TC_4}$	$\mathbf{WT_1}$	10	-0.77	9.22	7.70

5.1.2 2 Turbine Set-Up Results For Fixed Platform Motions

For TC_0-TC_9 the results of fixing the platform did not result in a significant change in power production, thrust force, torque or overturning moment.

For TC_0-TC_4 a shift of the yaw angle for maximum power production can be noticed. This is due to the counter rotation of the floater and is discussed in subsection 5.1.1.

The global loads for the fixed case can be found in Appendix A, Figure A.1 and A.2.

5.1.3 Spectral Analysis

The peak frequencies are analyzed to determine the influence of different wave frequencies and the influence of floater motions on the results.

A moving average filter is applied on each frequency plot, resulting in a smaller Y axis than without applying a moving average filter. The wave height can be verified, since $H_s \approx 4\sigma_\mu$. The standard deviation is found to be 0.5 resulting in a waveheight of $H_s \approx$ 2.0m, which is the same as used in HydroDyn. The peak period should be around 0.135, which could be seen in Figure 5.1. As previously stated, due to the application of the moving average filter, the peak is less noticeable.

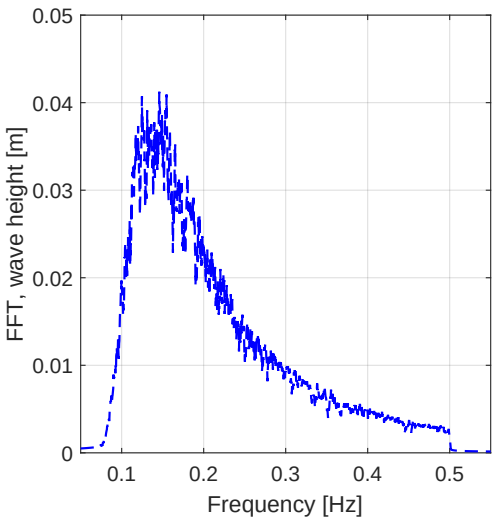

Figure 5.1: Fourier transform of the waveheight for WT_1, TC_13.

Figure 5.2 shows the fourier transform of the thrust force, F_x, for WT_1 of TC_0. The thrust force is mainly dominated by the wind, wave, 3P and 6P frequency response, where the 6P frequency response is a harmonic of the 3P frequency response. Little to no excitation is found at 1P.

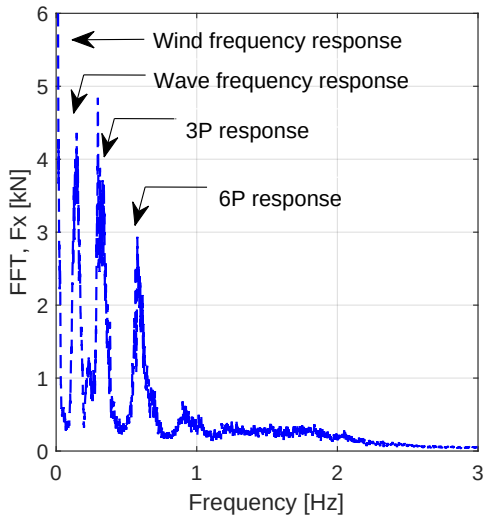

Figure 5.2: Fourier transform of the thrust force for WT_1, TC_0.

Figure 5.3 shows the fourier transform of the rotor torque, M_x, for WT_1 of TC_0. Frequencies dominating the frequency plot are the same as the frequencies in Figure 5.2.

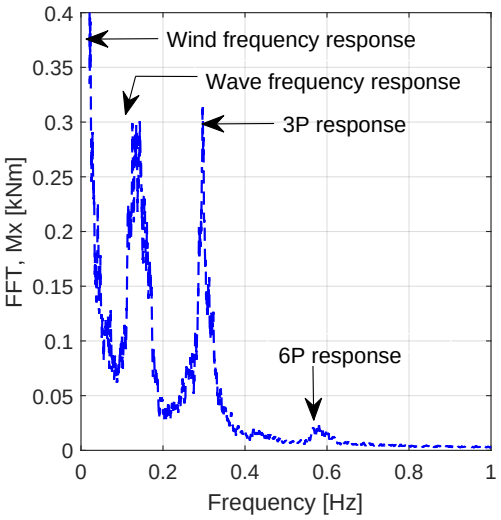

Figure 5.3: Fourier transform of the rotor torque for WT_1, TC_0.

Figure 5.4 shows the same peaks as the previous two figures and a peak at 9P, which is another harmonic frequency of the 3P frequency.

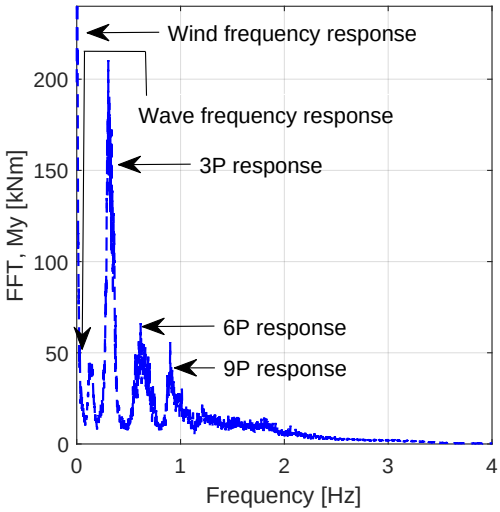

Figure 5.4: Fourier transform of the yaw bearing moment for WT_1, TC_0.

Figure 5.5 and 5.6 shows that both the surge and pitch response is close to the wind response. Further more it could be seen that the surge response can be found back in Figure 5.6, while the pitch response is not found in Figure 5.5. Both Figures show a peak occuring around the wave frequency response.

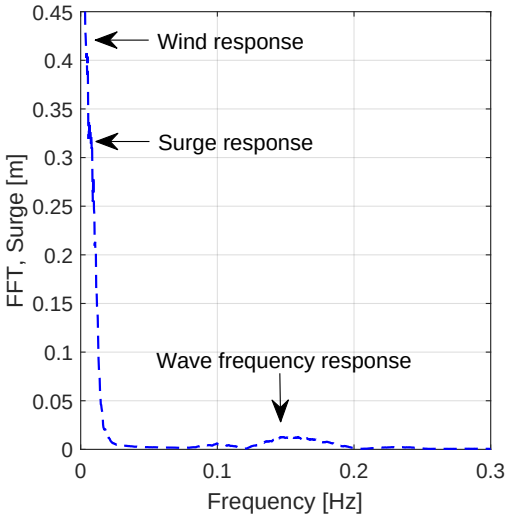

Figure 5.5: Fourier transform of the surge for WT_1, TC_0.

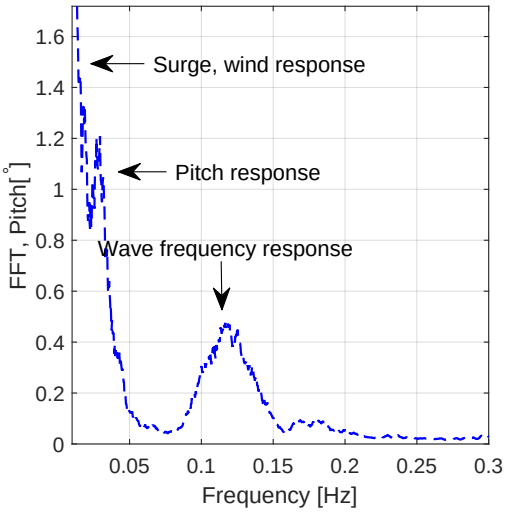

Figure 5.6: Fourier transform of the pitch for WT_1, TC_0.

The INP-A and HS-B bearing are both excited at the wind, wave, 3P and 6P frequencies. For the HS-B bearing also a small peak at 9P and $2.1Hz$ is found. The peak at $2.3Hz$ is due to the 3rd stage input shaft rotation frequency.

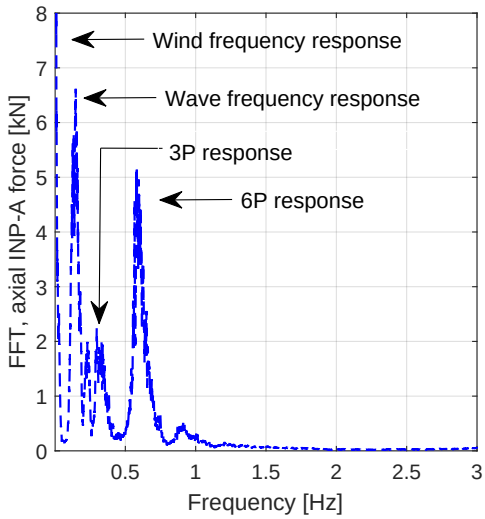

Figure 5.7: Fourier transform of the axial INP-A bearing load for WT_1, TC_0.

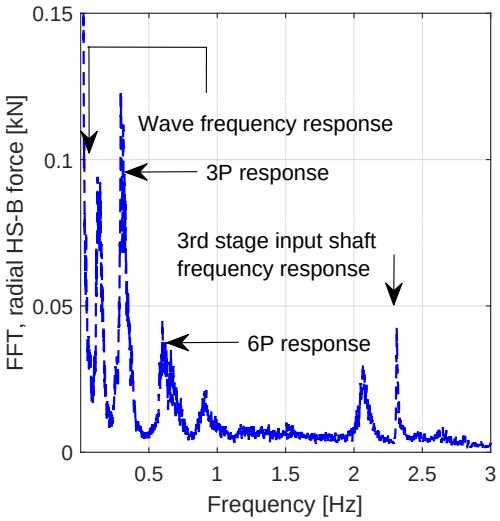

Figure 5.8: Fourier transform of the axial INP-A bearing load for WT_1, TC_0.

1P frequency responses are not found in the previous Figures. Further more, the wave frequency response is in between the 1P response and the 3P response. Looking at the FFT plots, it can be seen that the wave frequency response does not come close to the 3P response, while it can possibly come close to the 1P response. At rated, where the rotational speed of 9.6RPM is reached, which results in a 1P frequency of 0.16RPM, wave interference with 1P can occur. However, for a wind speed of $8m/s$, waves ranging from $T_P = 10s$ to $T_P = 4s$ will not cause significant interference with both the 1P and 3P. The results below are thus applicable for sea states with a T_P ranging from $4s$ to $10s$. Comparing the sea state to scatter data from DNV-RP-C205, the North Atlantic and the World Wide trade [143] and a paper released by Vikebø et al. (2003) [144] it is found that the used sea state corresponds to the lower parts of the scatter diagrams of DNV-RP-C205 and the scatter plot of Vikebø et al. (2003). For the North Sea a large part of the scatter plot consists of waves corresponding to a peak period below below $T_P \approx 10s$, while the North Atlantic scatter diagram shows that the lower 50% percentile occurs below $T_P \approx 9s$. Thus results found in the following Chapter also apply for sea states that occur in the North Sea, the North Atlantic and the rest of the world, as long as the T_P found does not interfere with the 1P frequency of the WT.

When comparing the global loads (F_x, M_x and M_y) frequency domain results to the fixed frequency domain results a small difference is found. The main difference found is that a smaller peak occurs at the 6P frequency of the thrust load for the fixed turbine case. Further more mean and standard deviation results do not show a significant difference in power production, thrust force and torque moment for the fixed wind turbine case. The results for the floating case will be discussed below, while the Figures for the fixed case can be found in Appendix A. With this it can be concluded that the global results for fixed and floating WTs agree with eachother and general conclusion made on the global loads and power production trends apply for both floating and bottom-founded WTs. Local loads and cost results on bottom-founded structures should be investigated seperately, similar to Nejad et al. (2015) [145].

5.2 Wake Steering Results

5.2.1 Turbulent Wind Field

Figure 5.9 and 5.10 show the wind speed at hub height for $t = 3000s$. For TC_0 and TC_4 the wake behind WT_1 and WT_2 can be noticed. There is not a significant wake deflection to be found for TC_4, but when comparing both Figures thoroughly, for TC_4 the wake is found to deflect in negative Y-direction. The wind speed in the wake does not seem to change significantly between TC_0 and TC_4.

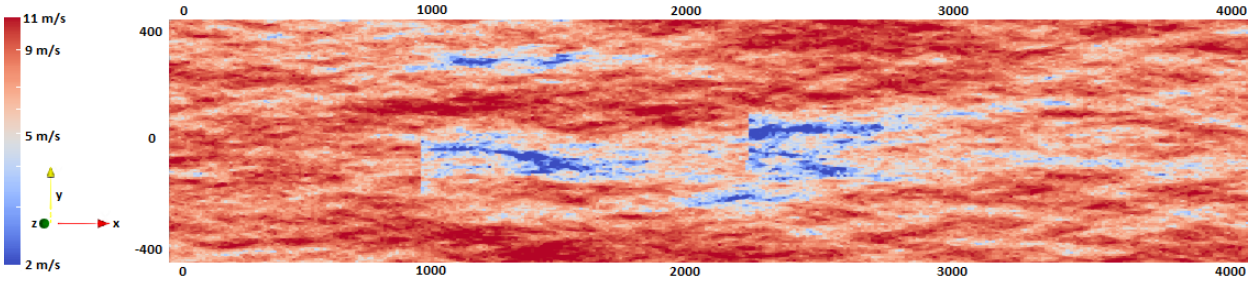

Figure 5.9: Flow visualization of the hub height wind speed for the reference yaw test case (TC_0).

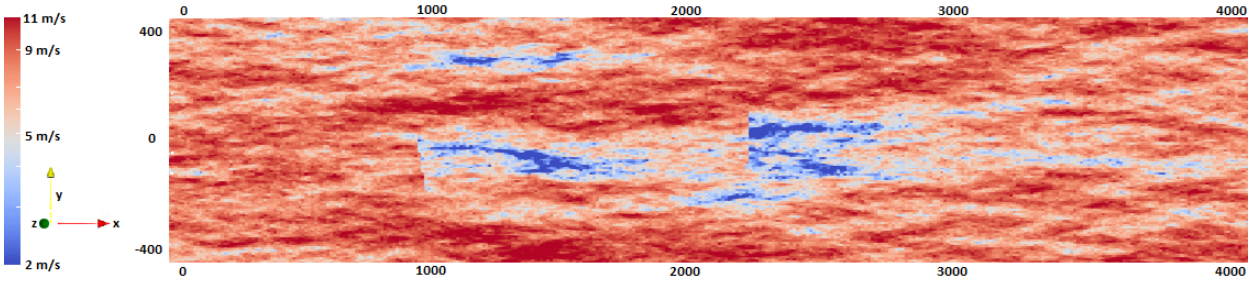

Figure 5.10: Flow visualization of the hub height wind speed for test case 4 (TC_4).

5.2.2 Power Production and global loads

In Table 5.2 and Figure 5.11 wind turbine and wind farm power production can be found. Partially having the second turbine in the wake of the first turbine results in a loss of $0.95MW$ for TC_0. For a yaw angle, γ, of 7° an increase of 0.78% is found. The power production changes approximately with the cosine of $\gamma^{2.7}$. This corresponds with literature [59] where it is stated that the power production changes with the cubed cosine of γ, as shown in Equation 2.22.

Power production verification : The maximum power production, using the C_P corresponding with the Betz limit, for 8 m/s will be $4.35MW$. The power production and C_P corresponding to Figure 2.19 are $3.75MW$ and 0.475 respectively. The power produced by WT_1 is $3.66MW$, 16% lower than the betz limit and close to the mechanical power curve. The simulation results of TC_0 give a mean C_P of 0.50 for WT_1. This would result in a power production of $3.93MW$ when using Equation 2.13, which is 7.5% higher than found for WT_1 of TC_0. This might be due to additional losses taken into account by FAST.Farm. For TC_0 the power produced by WT_2 indicates a wind speed of $V = 7.07m/s$ just before the rotor plane area of WT_2 using Equation 2.13, with a C_P of 0.51. The limited wake velocity deficit can be explained by the high TI of the ambient wind. A high TI will cause faster wake mixing with the ambient wind resulting in fast restoration of the wake.

With increasing γ for WT_1, a decrease in power production of WT_1 and an increase in power production of WT_2 is found, which corresponds with theory and literature discussed in section 2.7 and 2.8. The extent of the increase does not fully correspond with found literature. It should be noted that the TI of the turbulent wind field is higher than the TI in mentioned literature.

Comparing the results with the two turbine case carried out by Pieter Gebraad [142], which is discussed in section 2.8, the main differences found are the power production increase and the yaw angle at which the maximum power production increase occurs. For Gebraad, a power production increase of 4.6% was found for $\gamma = 25°$. This was however in low turbulent conditions.

Table 5.2: Power production in MW and power production increase in % for TC_0-TC_4 for WT_1, WT_2 and WT_1 and WT_2 together.

Test case	**Turbine number**	**Power production [MW]**		**Power production increase [%]**	
		Single WT	**WF**	**Single WT**	**WF**
TC$_0$	**WT$_1$** **WT$_2$**	3.66 2.71	6.37	0 0	0
TC$_1$	**WT$_1$** **WT$_2$**	3.63 2.78	6.41	-0.71 2.62	0.70
TC$_2$	**WT$_1$** **WT$_2$**	3.60 2.81	6.41	-1.48 3.83	0.78
TC$_3$	**WT$_1$** **WT$_2$**	3.58 2.83	6.41	-1.99 4.40	0.73
TC$_4$	**WT$_1$** **WT$_2$**	3.54 2.86	6.40	-3.19 5.72	0.60

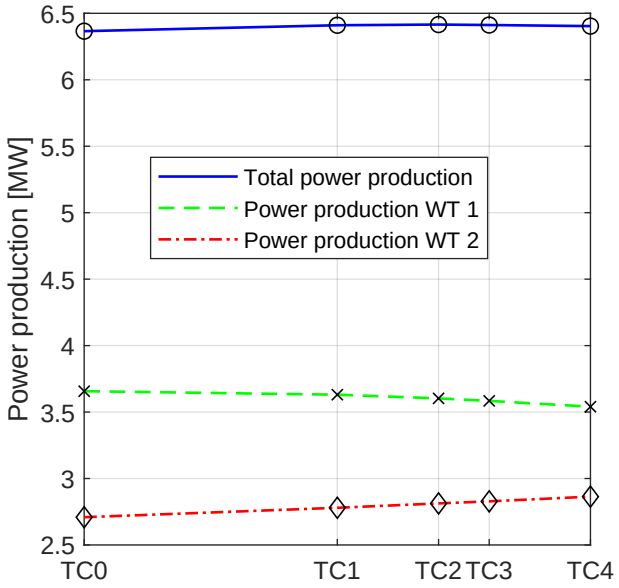

Figure 5.11: Total power production and power production of WT_1 and WT_2 for TC_0-TC_4.

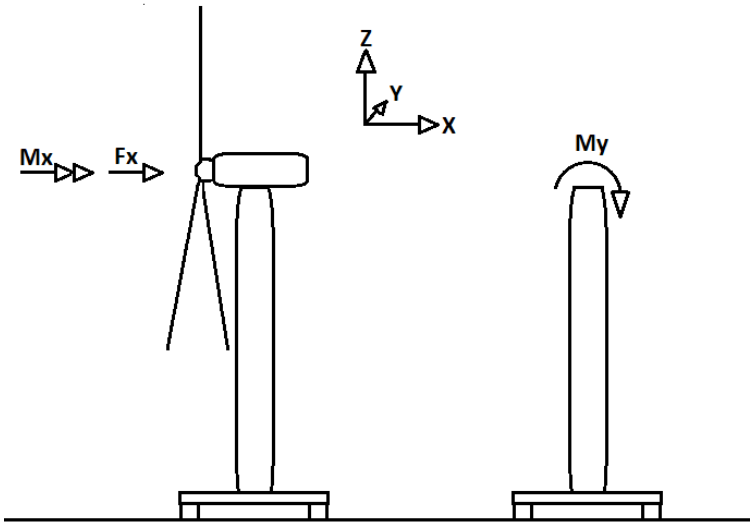

Figure 5.12: Thrust, torque and yaw bearing moment locations acting on the wind turbine.

Global loads needed for the 10MW drivetrain model are the thrust force, F_x, torque, M_x and the yaw bearing moment, M_y. The location where these forces and moments act on is shown in Figure 5.12. Further more the tower base overturning moment, $M_{y,base}$, is shown in Figure 5.13.

Figure 5.13 and Table 5.3 show that an increase in γ for WT_1 results in a decrease of F_x, M_x and $M_{y,base}$ for WT_1 and and an increase of F_x, M_x and $M_{y,base}$ for WT_2. The opposite is found for M_y.

Thrust load verification : Using Figure 2.17, Equation 2.13-2.18 and the C_P from the simulations, an approximation of the thrust for TC_0 can be found. The C_T for WT_1 and WT_2 are 0.62 and 0.63 respectively resulting in a thrust force of $0.61MN$ and $0.53MN$, smaller than the thrust force calculated by FAST.Farm. A small part of the difference can be due to FAST.Farm calculating the thrust load for each timestep with varying wind speeds. Since $T \sim V^2$, a turbulent wind field can result in higher overal thrust loads than steady wind fields. Figure 2.19 shows that the below rated C_T for the model is 0.81. This results in thrust loads of $0.79MN$ and $0.62MN$ for WT_1 and WT_2, closer to C_T results from Figure 5.13.

Yaw bearing moment verification : Figure 5.13 shows the yaw bearing moment acting on the tower, while Table 5.3 shows the yaw bearing moment acting on the nacelle. The latter is used for the 10MW drivetrain model. The yaw bearing moment, M_y, originates from the moment that is created by the thrust force and the mass of the blades and nacelle. These moments act in opposite direction, where the mass of the blades and nacelle creates a larger moment than the moment created by the thrust force. Thus with an increase in F_x a decrease in M_y should be found and visa versa, which is shown in the Figure 5.13.

Combined with the yawed wake of WT_1, the decrease in F_x will cause a decreased wake velocity deficit behind WT_1 resulting in an increase in P_{out}, F_x and M_x of the downwind turbine. F_x and M_x both scale with V^2 which results in these loads increasing with a similar relative rate for WT_2.

With an increase in γ, a decrease in power production of WT_1 is found. The TSR is close to constant to maintain maximum C_P. Thus a decrease in rotor torque for WT_1 for an increase in γ should be found. The Figure shows a slight decrease in rotor torque for an increase in γ.

For each global load, the standard deviation, σ, is higher for WT_2 than for WT_1, which can be due to added wake turbulence. Plots of F_y and M_z can be found in Appendix B, Figure B.1.

Table 5.3: Mean (μ) and standard deviation (σ) of the thrust force (F_x), yaw bearing moment (M_y) acting on the nacelle and rotor torque (M_x) for TC_0-TC_4.

Test case	**Turbine number**	$\mathbf{F}_x[MN]$		$\mathbf{M}_y[MNm]$		$\mathbf{M}_x[MNm]$	
		μ	σ	μ	σ	μ	σ
$\mathbf{TC}_0$	$\mathbf{WT}_1$	1.0	0.16	1.6	2.7	5.5	1.1
	$\mathbf{WT}_2$	0.82	0.17	2.9	2.8	4.2	1.3
$\mathbf{TC}_1$	$\mathbf{WT}_1$	1.0	0.16	1.8	2.7	5.5	1.1
	$\mathbf{WT}_2$	0.83	0.17	2.8	2.8	4.3	1.3
$\mathbf{TC}_2$	$\mathbf{WT}_1$	0.96	0.16	1.9	2.7	5.4	1.1
	$\mathbf{WT}_2$	0.83	0.17	2.8	2.8	4.4	1.3
$\mathbf{TC}_3$	$\mathbf{WT}_1$	0.96	0.16	2.0	2.7	5.4	1.1
	$\mathbf{WT}_2$	0.84	0.17	2.8	2.8	4.4	1.3
$\mathbf{TC}_4$	$\mathbf{WT}_1$	0.95	0.15	2.1	2.7	5.4	1.1
	$\mathbf{WT}_2$	0.84	0.17	2.7	2.8	4.4	1.3

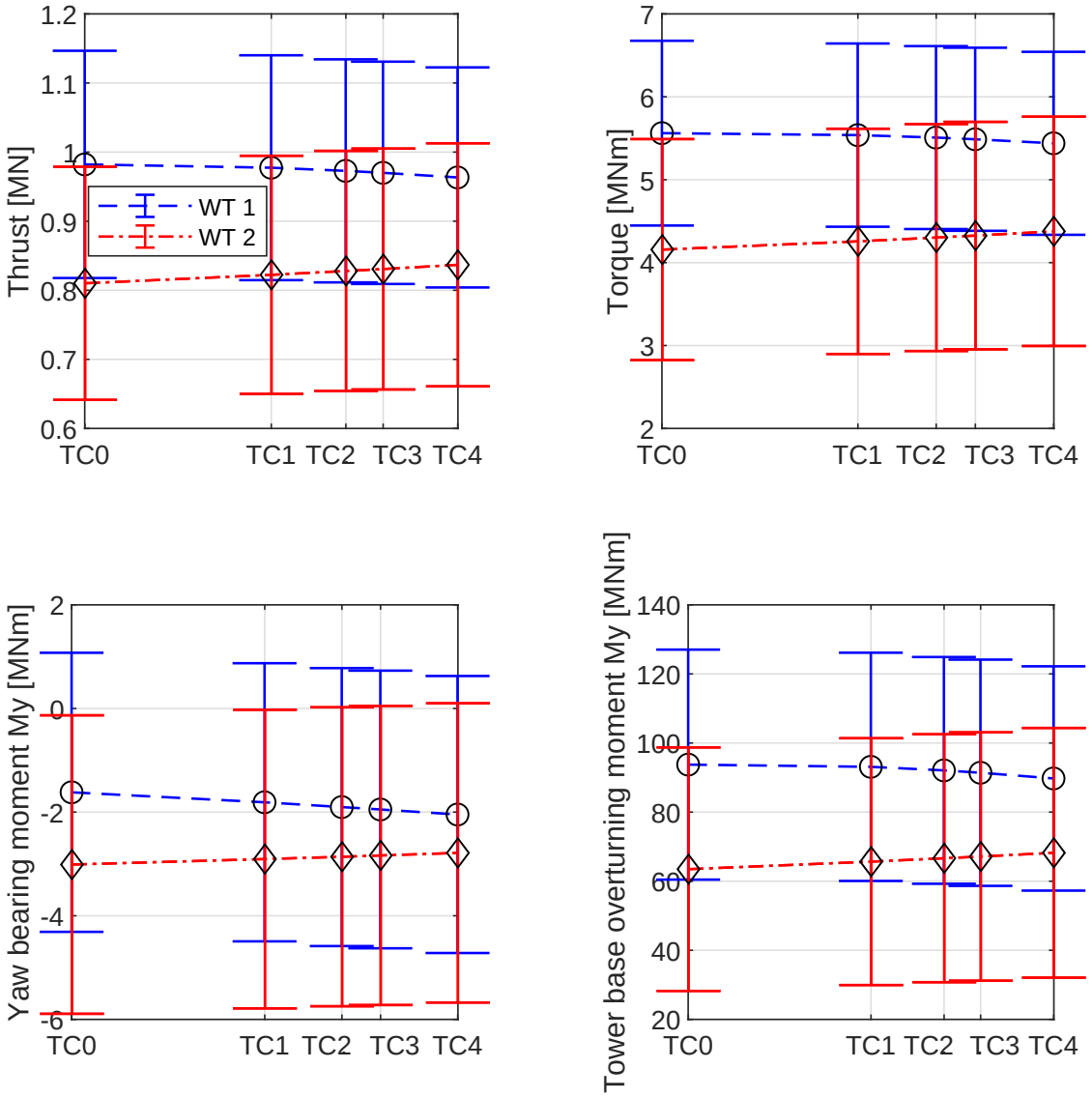

Figure 5.13: Mean (μ) and standard deviation (σ) of thrust (F_x), rotor torque (M_x), yaw bearing moment (M_y) acting on the tower and tower base overturning moment ($M_{y,base}$) for $TC_0 - TC_4$.

5.2.3 Drivetrain Fatigue Results

Figure 5.30 shows a pie chart of the fatigue damage results for the bearings of TC_0, Table 5.4 shows absolute fatigue damage of the considered bearings and Table 5.5 shows relative fatigue damage having TC_0 as baseline.

Figure 5.30 shows that the highest fatigue damage is found for the INP-A, INP-B, PLC-B and HS-A bearing. The remaining bearings are significantly less damaged. Wang et al. (2020) [47] states that the large fatigue damage on the INP-A bearing is mainly due to the large rotor thrust loads it has to sustain in combination with the weight of the rotor blades, while the damage on the HS-A bearing is mainly due to the large number of load cycles that are experienced by this bearing.

For TC_0 the damage of the INP-A, PLC-A and PLC-B bearings is significantly larger for the downwind turbine, which can be seen in Table 5.3. This can be due to wake induced turbulence, the increase in standard deviation for each global load or the increase in M_y for WT_2 compared to WT_1. Equation 2.35 and 2.36 show that the dynamic equivalent radial load scales with a, which can be found in Table 3.5. Each value of a for the considered bearings is 10/3, indicating that the damage scales with 10/3 of the equivalent radial load fluctuations.

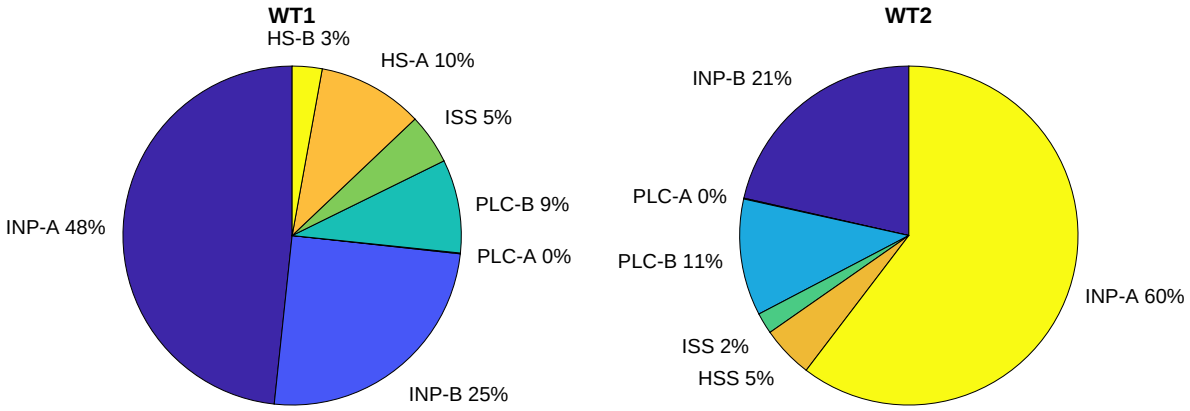

Figure 5.14: Pie chart of the fatigue damage of WT_1 and WT_2 for TC_0. For WT_1 IMS-PLC-A, IMS-PLC-B, IMS-A and IMS-B are grouped in ISS. For WT_2 HS-A and HS-B are grouped in HSS and IMS-PLC-A, IMS-PLC-B, IMS-A and IMS-B are grouped in ISS.

For an increase in γ an increase in fatigue damage for INP-A, PLC-A and PLC-B of WT_1 is found, while a decrease in fatigue damage is found for the remaining bearings of WT_1.

For WT_2 a decrease in fatigue damage for the INP-A bearing is found. This can result from a decrease in M_y, which corresponds with results found in Table 5.3, where the mean of M_y is found to decrease with an increase in γ. A similar decrease is found for the PLC-B bearing. For the remaining bearings of WT_2 an increase in fatigue damage is found, where the increase in fatigue damage of the intermediate and high speed shaft is mainly due to the increase in rotor torque. which corresponds with Figure 5.13.

In Figure 5.15 the INP-A and INP-B bearing fatigue damage is plotted for TC_0-TC_4. An increase in INP-A bearing fatigue damage for WT_1 can be seen, while a decrease for WT_2

can be seen, which is the other way around for the INP-B bearing.

Table 5.4: One hour bearing fatigue damage results for TC_0-TC_4 for the bearings mentioned in section 3.7. Red indicates a bearing where the damage exceeds 5.0×10^{-5}, orange indicates a bearing between 5.0×10^{-6} and 5.0×10^{-5} and green indicates a bearing with less than 5.0×10^{-6} damage.

One hour bearing damage [-]	**WT_1**				
	TC_0	TC_1	TC_2	TC_3	TC_4
INP-A	5.6E-05	6.1E-05	6.2E-05	6.3E-05	6.5E-05
INP-B	2.9E-05	2.8E-05	2.7E-05	2.7E-05	2.7E-05
PLC-A	8.9E-08	9.0E-08	9.1E-08	9.2E-08	9.2E-08
PLC-B	1.0E-05	1.1E-05	1.2E-05	1.2E-05	1.2E-05
IMS-PLC-A	8.5E-09	8.3E-09	8.2E-09	8.1E-09	8.0E-09
IMS-PLC-B	1.6E-06	1.6E-06	1.5E-06	1.5E-06	1.5E-06
IMS-A	1.7E-06	1.7E-06	1.6E-06	1.6E-06	1.6E-06
IMS-B	2.2E-06	2.2E-06	2.1E-06	2.1E-06	2.0E-06
HS-A	1.2E-05	1.1E-05	1.1E-05	1.1E-05	1.0E-05
HS-B	3.3E-06	3.2E-06	3.2E-06	3.1E-06	3.0E-06
One hour bearing damage [-]	**WT_2**				
	TC_0	TC_1	TC_2	TC_3	TC_4
INP-A	7.8E-05	7.6E-05	7.5E-05	7.5E-05	7.5E-05
INP-B	2.8E-05	2.8E-05	2.8E-05	2.8E-05	2.8E-05
PLC-A	1.0E-07	1.0E-07	1.0E-07	1.0E-07	1.0E-07
PLC-B	1.4E-05	1.4E-05	1.4E-05	1.4E-05	1.4E-05
IMS-PLC-A	5.1E-09	5.3E-09	5.4E-09	5.5E-09	5.6E-09
IMS-PLC-B	7.1E-07	7.7E-07	7.9E-07	8.0E-07	8.3E-07
IMS-A	8.6E-07	9.1E-07	9.4E-07	9.5E-07	9.8E-07
IMS-B	1.0E-06	1.1E-06	1.1E-06	1.1E-06	1.2E-06
HS-A	4.9E-06	5.3E-06	5.5E-06	5.6E-06	5.8E-06
HS-B	1.5E-06	1.6E-06	1.7E-06	1.7E-06	1.7E-06

Table 5.5: Relative bearing fatigue damage for TC_0-TC_4 compared to TC_0 for the bearings mentioned in section 3.7. Green indicates a bearing that decreased with more than 10%, red indicates a bearing that increased with more than 10% and orange indicates the remaining bearings.

Relative bearing damage [%]	**WT$_1$**				
	TC_0	TC_1	TC_2	TC_3	TC_4
INP-A	0	8.0	11.3	13.3	16.4
INP-B	0	-4.0	-5.7	-6.4	-8.4
PLC-A	0	1.7	2.6	3.2	3.7
PLC-B	0	7.5	10.8	12.5	15.6
IMS-PLC-A	0	-1.8	-3.3	-4.2	-6.4
IMS-PLC-B	0	-3.0	-5.3	-6.7	-10.0
IMS-A	0	-2.5	-4.5	-5.7	-8.5
IMS-B	0	-3.0	-5.2	-6.6	-9.8
HS-A	0	-3.5	-6.0	-7.5	-11.0
HS-B	0	-2.8	-4.9	-6.3	-9.5
Relative bearing damage [%]	**WT$_2$**				
	TC_0	TC_1	TC_2	TC_3	TC_4
INP-A	0	-2.1	-2.8	-3.0	-3.8
INP-B	0	1.3	1.9	2.6	3.1
PLC-A	0	-0.2	-0.2	0.1	0.1
PLC-B	0	-1.7	-2.3	-2.4	-3.0
IMS-PLC-A	0	4.7	6.9	8.0	10.5
IMS-PLC-B	0	7.6	11.1	12.8	17.1
IMS-A	0	6.0	8.9	10.3	13.6
IMS-B	0	7.3	10.6	12.3	16.4
HS-A	0	8.3	12.2	14.1	18.8
HS-B	0	7.6	11.1	12.8	17.0

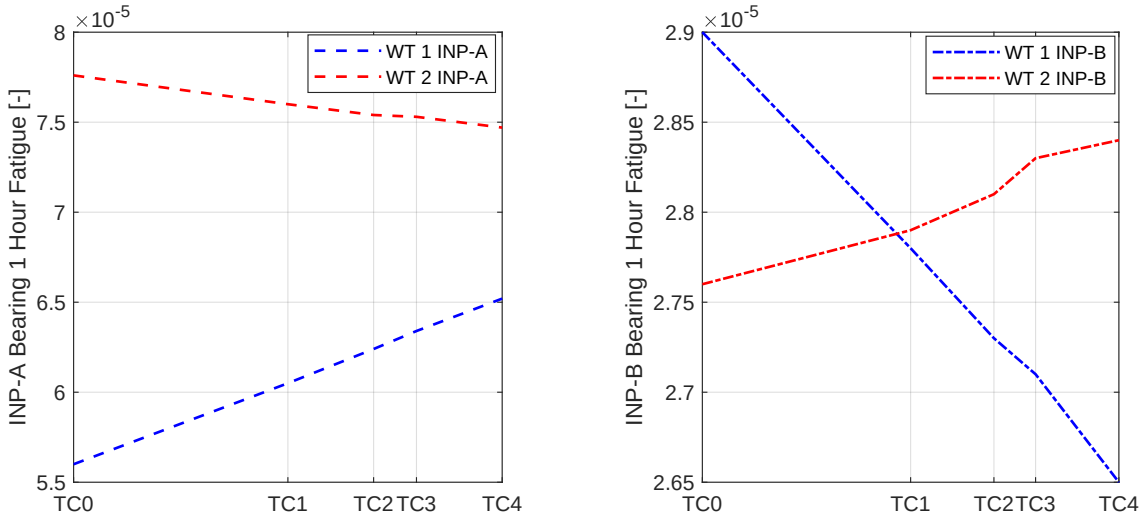

Figure 5.15: Main bearing fatigue of the INP-A and INP-B bearings for TC_0-TC_4.

5.2.4 2 Turbine Set-Up Wake Steering Results For An Uniform Wind Field

For the two turbine set-up the test cases in Table 4.3 are considered. TC_{10} and TC_{11} were added when it was found that the maximum power production was not yet reached for $\gamma < 10°$.

Figure 5.16 and 5.17 show the wake of the wind farm with similar coordinates as the two turbine set-up in the turbulent wind field, which can be found in Table 3.1. Figure 5.16 and 5.17 are visualisations of TC_0 and TC_{11}, which corresponds to $\gamma = 0°$ and $\gamma = 20°$. The visualisation shows that the wake of WT_1 for TC_{11} has a higher wind speed than the wake of WT_1 for TC_0 and shows a clear wake deflection for TC_{11} that recovers and slowly changes to the mean wind direction with increased wake distance.

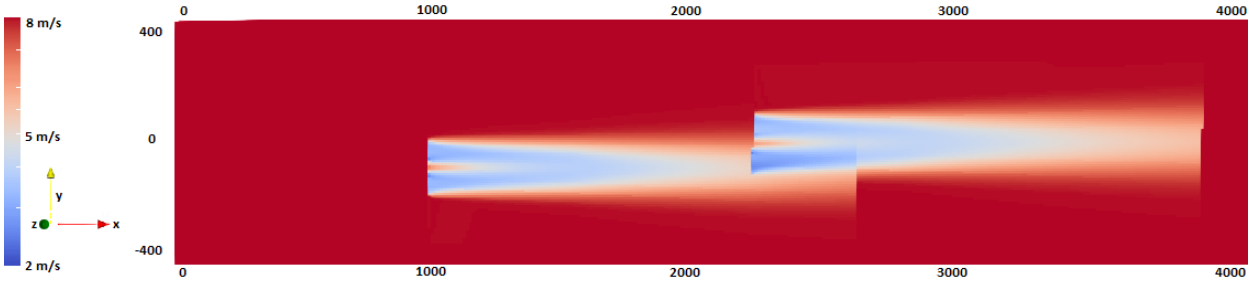

Figure 5.16: Flow visualization of the hub height wind speed for test case 0 (TC0) with a constant wind speed of 8 m/s at hub height.

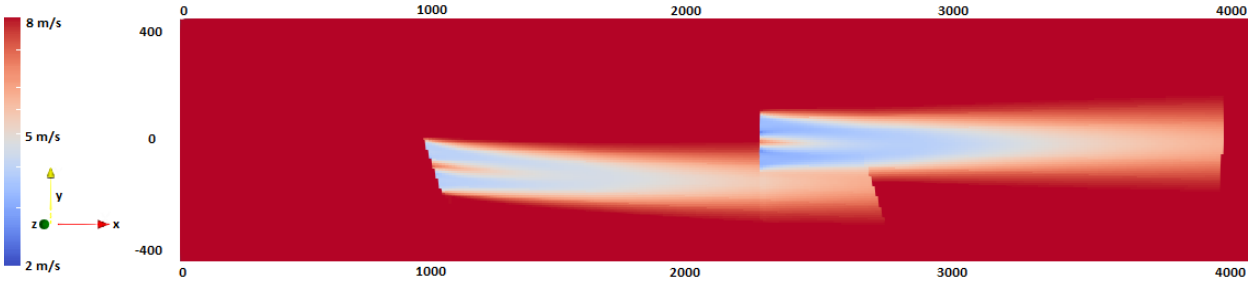

Figure 5.17: Flow visualization of the hub height wind speed for test case 11 (TC11) with a constant wind speed of 8 m/s at hub height.

The two turbine set-up in the uniform wind field resulted in a decreased power production for the downwind turbine.

From Table 5.6, WT_1 is found to have a power production which is approximately 1% lower in steady wind. This can be caused by large turbulent fluctuations, with an identical mean wind speed, causing an increased power production in turbulent wind fields, since power production scales with V^3.

Further more, the power production of WT_2 is found to be 14% lower for TC_0, increasing faster with an increase in γ in steady wind compared to turbulent wind. Since the ambient wind field has no turbulence, the wake recovers slowly due to shear between the wake and the ambient wind field.

Comparing the results in steady wind with the two turbine case carried out by Pieter Gebraad [142], which is discussed in section 2.8, a smaller deviation is found, than for the turbulent wake steering results.

For Gebraad, a power production increase of 4.6% was found for $\gamma = 25^\circ$, while in this steady wind case a power production increase of 4.8% is found for $15^\circ < \gamma < 20^\circ$. The deviation of both parameters can be due to the difference in turbine position in y-direction and the difference in the ambient wind field. Further more Gebraad used a NREL 5 MW WT, while in this test case the Nautilus 10MW FWT is used with different dynamics and a different wind turbine controller. Since FAST.Farm is optimized and validated using SOWFA, which is used by Gebraad, results should be in the same range. However, it should be noted that the control yaw angle does not indicate the total yaw angle, which is already discussed in subsection 5.1.1. This results in a larger deviation from the study of Gebraad.

In Figure 5.18 and Figure 5.19 a clear linear power production increase can be seen for $0^\circ < \gamma < 20^\circ$ of WT_2. For WT_1 a decrease in power production can be seen that is close to the cubed cosine of γ, which is similar to decrease in power production of WT_1 in the turbulent wind field case. The main difference between the turbulent wind field case and the uniform wind field case is the rate at which the power production of WT_2 increases. For the turbulent wind field case faster wake recovery occurs, resulting in a smaller rate of power production increase. If the rate of power production decrease of WT_1 exceeds the rate of power production increase of WT_2, the maximum power production $P_{out}(\gamma)$ for the wind farm is reached when two wind turbines are considered. This also means that, assuming that the power production of WT_2 is fully linear, the γ corresponding to maximum power production on wind farm level is highly dependent on the rate of power production increase of $P_{2,out}(\gamma)$, since $P_{1,out}(\gamma)$ shows a very limited difference for $0^\circ < \gamma < 10^\circ$ for the turbulent wind field case and the uniform wind field case.

This may indicate that the optimal wake steering angle can be indicated by mainly knowing the TI of the ambient wind field for a specific turbine spacing, turbine type and the wake overlap of the downwind turbine. This should however be further researched before clear conclusions can be drawn.

The global loads can be found in Appendix C, Figure C.1.

Table 5.6: Power production in MW and power production increase in % for each wake steering test case considering each turbine separately and both turbines together with a steady wind speed of 8 m/s.

Test case	Turbine number	Power production [MW]		Power production increase [%]	
		Single WT	WF	Single WT	WF
TC_0	WT_1 WT_2	3.63 2.39	6.02	0 0	0
TC_1	WT_1 WT_2	3.59 2.58	6.17	-1.02 7.75	2.46
TC_2	WT_1 WT_2	3.56 2.65	6.21	-1.95 10.9	3.18
TC_3	WT_1 WT_2	3.53 2.69	6.23	-2.51 12.6	3.48
TC_4	WT_1 WT_2	3.49 2.77	6.26	-3.85 15.9	4.00
TC_{10}	WT_1 WT_2	3.33 2.98	6.31	-8.28 24.6	4.78
TC_{11}	WT_1 WT_2	3.11 3.19	6.30	-14.2 33.5	4.77

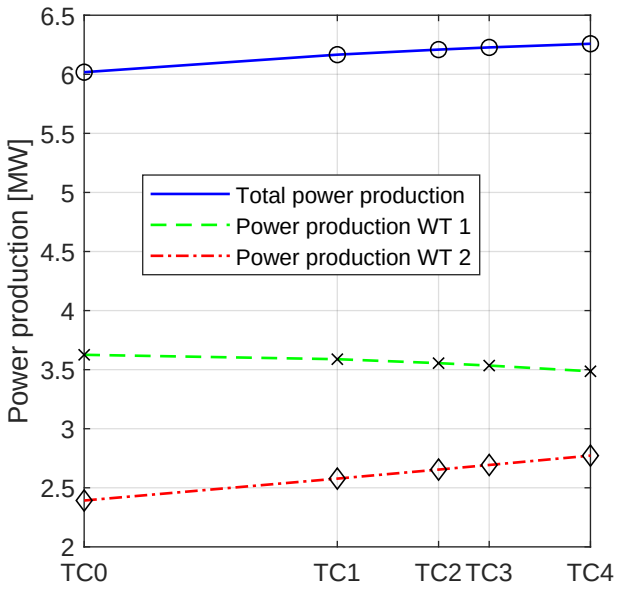

Figure 5.18: Total power production and power output of FWT 1 and FWT 2 for each wake steering control test case with a constant wind speed of 8 m/s at hub height.

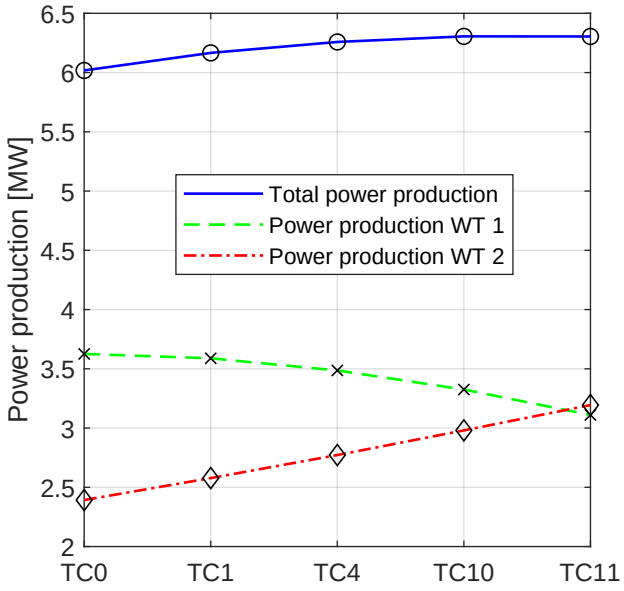

Figure 5.19: Total power output and power output of FWT 1 and FWT 2 for each wake steering control test case and $TC_{10}(\gamma = 15°)$ and $TC_{11}(\gamma = 20°)$ with a constant wind speed of 8 m/s at hub height.

5.2.5 4 Turbine Set-Up Wake Steering Results For An Uniform Wind Field

The two wind turbine set-up is extended to a four wind turbine set-up with similar spacing in X and Y direction, found in subsection 4.2.1. The same test cases as for the two turbine set-up are used, where WT_1, WT_2 and WT_3 are each yawed to the angle stated in Table 4.3. Figure 5.20 and 5.21 show the flow visualisation of the XZ-plane for TC_0 and TC_{11}.

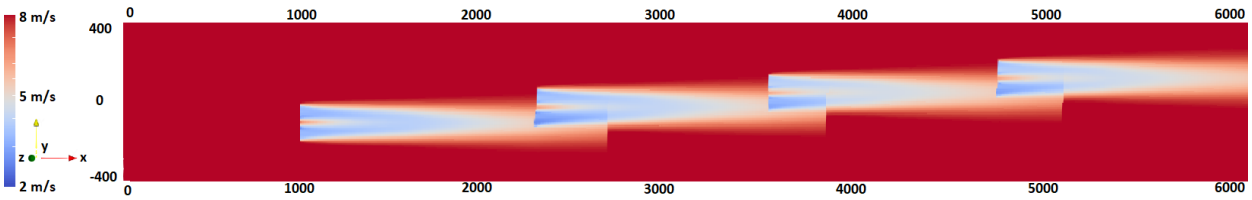

Figure 5.20: Flow visualization of the hub height wind speed for the reference pitch test case 0 (TC_0) with a constant wind speed of 8 m/s at hub height.

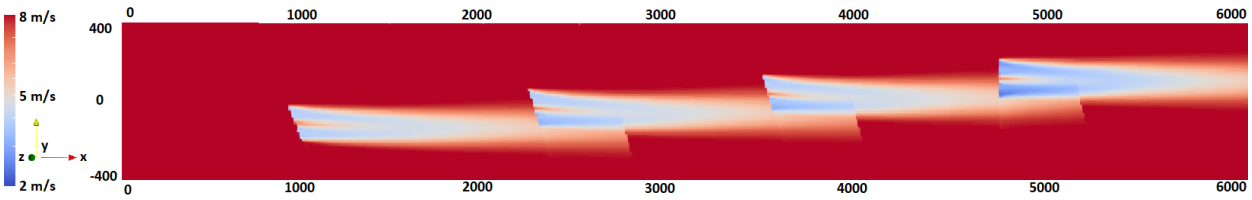

Figure 5.21: Flow visualization of the hub height wind speed for test case 11 (TC_{11}) with a constant wind speed of 8 m/s at hub height.

In Table 5.7, Figure 5.22 and Figure 5.23 the power production results can be found. For WT_1 similar power production results are found for each test case compared to the two turbine set-up. For an increase in γ, an increase in power production for WT_2, WT_3 and WT_4 is found, resulting in a 16.6% increase in wind farm power production for $\gamma = 20^\circ$, increasing the power production of WT_4 with 46%.

The power production of WT_2 is higher for TC_0-TC_3 for the four turbine case compared to the two turbine case, even though the turbine is yawed, which normally results in a decrease in power production. For the two turbine case a transient of 400s is used, while for the four turbine case a transient of 1000s is used. The turbine wakes change over time, even though the wind field is steady. Thus using different transient lengths can result in a small power production deviation for WT_2.

The power production of WT_2 is found to be higher than the power production of WT_3 for $0^\circ < \gamma < 10^\circ$ and found to be lower for $10^\circ < \gamma < 20^\circ$, which is shown in Figure 5.38. From the Figure it could also be noted that the power production of WT_4 increases more than the power production of WT_2 and WT_3, since WT_4 has optimal power production control settings, similar to previous test cases. The power production curve for WT_2 and WT_3 tend to flatten, which is due to the increase in power production caused by upwind wake deflection, while the decrease in power production is due to yaw misalignment.

The power production of WT_3 is smaller than the power production of WT_2, since the wake deficit behind WT_2 is larger than behind WT_1 for $\gamma < 10^\circ$. When the wake is deflected further from the downwind WT, it can be seen that the power production of WT_3 surpasses the power production of WT_2. It could also be seen that the power production of WT_4, which is the only WT that does not yaw, increases more and surpasses WT_2 and WT_3 at $\gamma = 10^\circ$.

Table 5.7: Power production in MW and power production increase in % for each wake steering test case considering each turbine separately and the four turbines together with a steady wind speed of 8 m/s.

Test case	**Turbine number**	**Power production [MW]**		**Power production increase [%]**	
		Single WT	**WF**	**Single WT**	**WF**
$\mathbf{TC_0}$	$\mathbf{WT_1}$	3.63	10.45	0	0
	$\mathbf{WT_2}$	2.39		0	
	$\mathbf{WT_3}$	2.19		0	
	$\mathbf{WT_4}$	2.25		0	
$\mathbf{TC_1}$	$\mathbf{WT_1}$	3.58	11.14	-1.02	6.5
	$\mathbf{WT_2}$	2.60		8.73	
	$\mathbf{WT_3}$	2.49		14.0	
	$\mathbf{WT_4}$	2.46		9.06	
$\mathbf{TC_2}$	$\mathbf{WT_1}$	3.55	11.39	-1.94	8.9
	$\mathbf{WT_2}$	2.67		11.6	
	$\mathbf{WT_3}$	2.60		18.9	
	$\mathbf{WT_4}$	2.57		14.0	
$\mathbf{TC_3}$	$\mathbf{WT_1}$	3.53	11.51	-2.51	10.1
	$\mathbf{WT_2}$	2.70		12.9	
	$\mathbf{WT_3}$	2.65		21.2	
	$\mathbf{WT_4}$	2.63		16.7	
$\mathbf{TC_4}$	$\mathbf{WT_1}$	3.49	11.74	-3.84	12.3
	$\mathbf{WT_2}$	2.75		15.1	
	$\mathbf{WT_3}$	2.74		25.4	
	$\mathbf{WT_4}$	2.76		22.4	
$\mathbf{TC_{10}}$	$\mathbf{WT_1}$	3.33	12.14	-8.27	16.1
	$\mathbf{WT_2}$	2.84		18.8	
	$\mathbf{WT_3}$	2.90		32.8	
	$\mathbf{WT_4}$	3.07		36.3	
$\mathbf{TC_{11}}$	$\mathbf{WT_1}$	3.11	12.19	-14.2	16.6
	$\mathbf{WT_2}$	2.85		19.2	
	$\mathbf{WT_3}$	2.93		34.2	
	$\mathbf{WT_4}$	3.29		46.3	

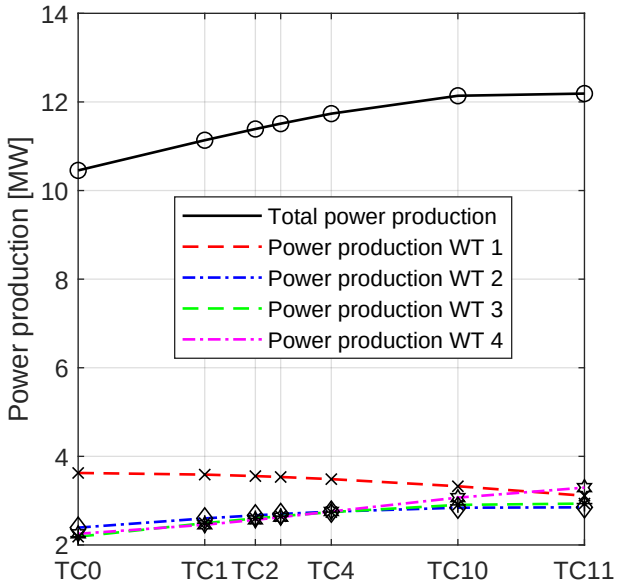

Figure 5.22: Total power production and power production of each turbine for TC_0-TC_4, $\mathrm{TC}_{10}(\gamma = 15°)$ and $\mathrm{TC}_{11}(\gamma = 20°)$ with a steady wind speed of 8 m/s at hub height.

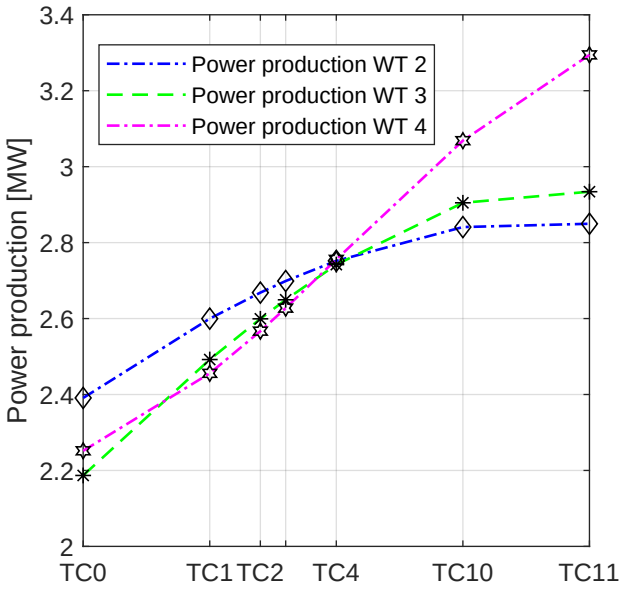

Figure 5.23: Power production of WT_2, WT_3 and WT_4 for TC_0-TC_4, $\mathrm{TC}_{10}(\gamma = 15°)$ and $\mathrm{TC}_{11}(\gamma = 20°)$ with a steady wind speed of 8 m/s at hub height.

5.3 Axial Induction Results

5.3.1 Turbulent Wind Field

Figure 5.24 and 5.25 show the wind speed at hub height for $t = 3000s$. For TC_5 and TC_9 the wake behind WT_1 and WT_2 can be noticed. The wake of TC_9 shows a smaller velocity deficit compared to TC_5, which should result in an increased wind speed at the rotor plane of WT_2 for TC_9 compared to TC_5.

For the induction cases, a flow visualisation of the $XZ - plane$ has been made, which can be seen in Figure 5.26 and 5.27, to further investigate the wind turbine wake for TC_5 and TC_9. It shows, just as for the $XY - plane$, a significant smaller velocity deficit behind WT_1.

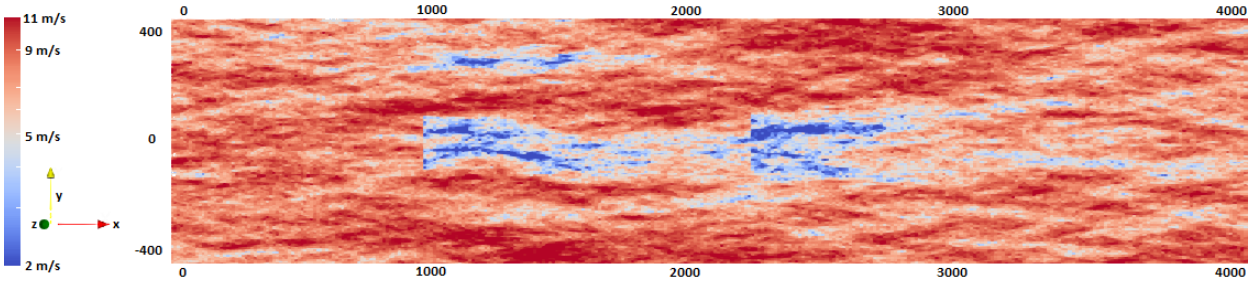

Figure 5.24: Flow visualization of the hub height wind speed for the reference pitch test case 5 (TC_5).

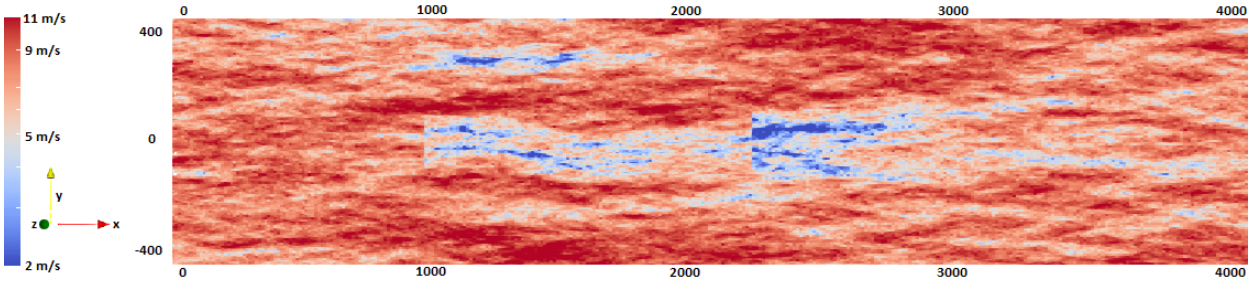

Figure 5.25: Flow visualization of the hub height wind speed for test case 9 (TC_9).

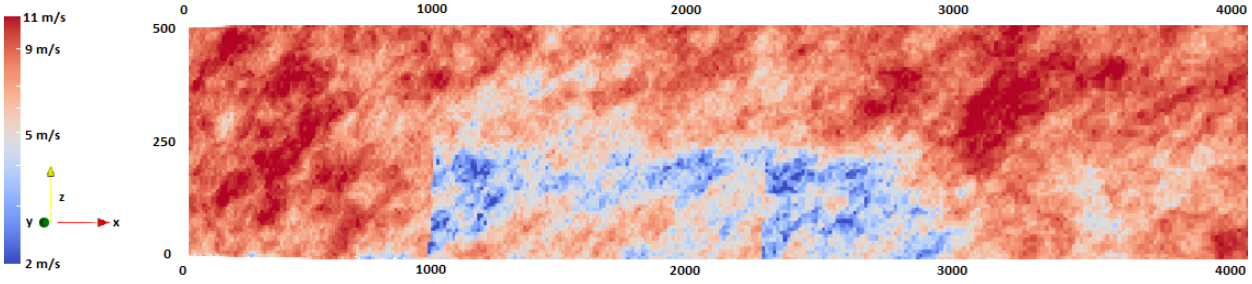

Figure 5.26: Flow visualization at y = 0 for test case 5 (TC_5).

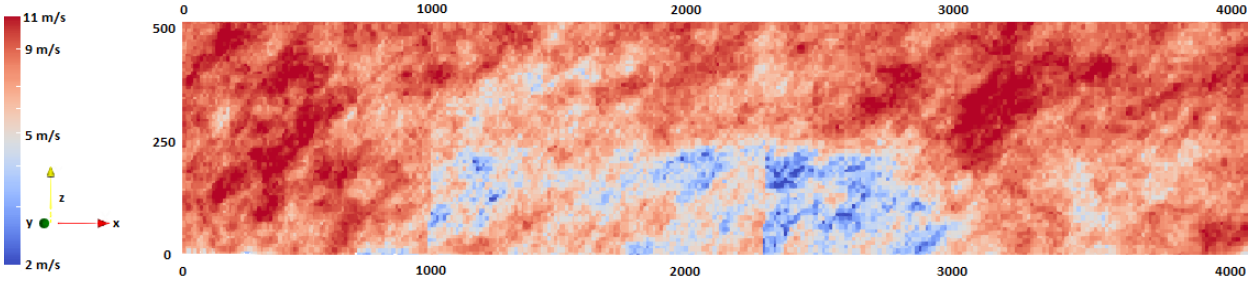

Figure 5.27: Flow visualization at y = 0 for test case 9 (TC_9).

5.3.2 Power Production And Global Loads

In Table 5.8 and Figure 5.28 wind turbine and wind farm power production can be found. Having the downwind turbine fully in the wake of the upwind turbine results in a loss of $1.40MW$ for TC_5, which is a decrease of 37% compared to WT_1. For a blade pitch angle, β, of 1° an increase of 0.17% is found.

Power production verification : The maximum power production, using the C_P corresponding with the Betz limit, for 8 m/s will be $4.35MW$. The power production and C_P corresponding to Figure 2.19 are $3.75MW$ and 0.475 respectively. The power produced by WT_1 for TC_5 is 13% lower than the betz limit. the simulation results give a mean C_P of 0.5 for WT_1, which would result in a power production of $3.91MW$ when using Equation 2.13, 4% higher than found for WT_1 of TC_5. For TC_5 the power produced for WT_2 indicates a wind speed of $V = 6.74m/s$ just before the rotor plane area of WT_2, which is calculated in the same way as in subsection 5.2.2.

With increasing β for WT_1, a decrease in power production for WT_1 and an increase in power production for WT_2 is found, which corresponds with section 2.9.

Table 5.8: Power production in MW and power production increase in % for each wake induction test case for each turbine separately and both turbines together.

Test case	Turbine number	Power production [MW]		Power production increase[%]	
		Single WT	WF	Single WT	WF
TC_5	WT_1 WT_2	3.79 2.39	6.18	0 0	0
TC_6	WT_1 WT_2	3.76 2.43	6.19	-0.80 1.72	0.17
TC_7	WT_1 WT_2	3.67 2.50	6.18	-3.05 4.89	0.02
TC_8	WT_1 WT_2	3.53 2.59	6.12	-6.71 8.43	-0.86
TC_9	WT_1 WT_2	3.35 2.69	6.04	-11.6 12.6	-2.24

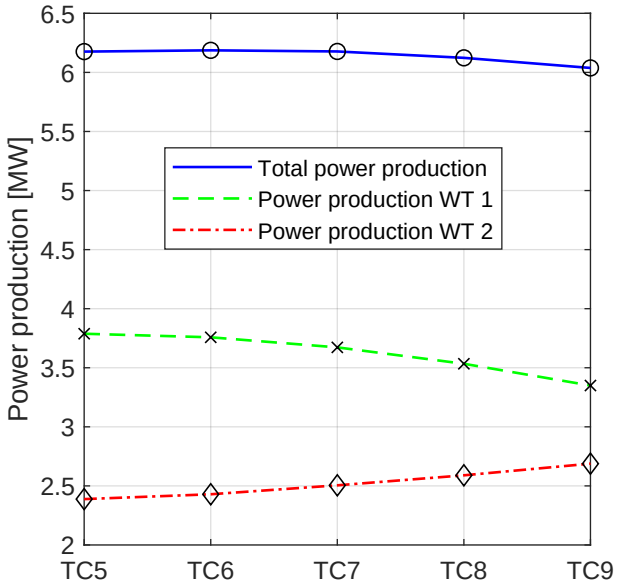

Figure 5.28: Total power production and power production of WT_1 and WT_2 for TC_5-TC_9.

Figure 5.29 and Table 5.9 show that an increase in β for WT_1 results in a decrease of F_x, M_x and $M_{y,base}$ for WT_1 and and an increase of F_x, M_x and $M_{y,base}$ for WT_2. The opposite is found for M_y. The decrease in F_x and $M_{y,base}$ for WT_1 is larger than the increase of F_x and $M_{y,base}$ for WT_2, while the change in M_x is smaller for the considered test cases.

Thrust load verification : C_T found from C_P for WT_1 and WT_2 of TC_5 are 0.62 and 0.64 resulting in a thrust force of $0.60MN$ and $0.53MN$, which is smaller than the thrust force calculated by FAST.Farm and is already discussed in subsection 5.2.2. Figure 2.19 shows a below rated C_T of 0.81. This will result in thrust loads of $0.79MN$ and $0.62MN$ for WT_1 and WT_2, closer to C_T results from Figure 5.29. The thrust load of TC_9 can be verified by determining C_P of WT_1 for TC_5 and TC_9. TC_9 has a C_P of 0.44 resulting in a power production of $3.46MW$ by using Equation 2.13. This C_P corresponds to a C_T of 0.52 resulting in a thrust of $0.46MN$. A decrease in C_P of 12% results in a decrease in C_T of 23%. Comparing the thrust of WT_1 for TC_5 and TC_9, a decrease in thrust of 23% is found, which corresponds to the theory of section 2.9.

From the Figure it can be seen that F_x decreases faster for WT_1 than the power production of WT_1, which is due to the decrease in C_T, which decreases faster than C_P discussed in section 2.9. The overall decrease in F_x for an increase in β can indicate a decrease in fatigue loads.

Figure 5.29 shows the yaw bearing moment acting on the tower, while Table 5.9 shows the yaw bearing moment acting on the nacelle. The yaw bearing moment, M_y, decreases with an increase in F_x.

Table 5.9 shows that the standard deviation, σ, for F_x and M_x of WT_1 decreases with an increase in β, while the remaining values tend to stay around the same value.

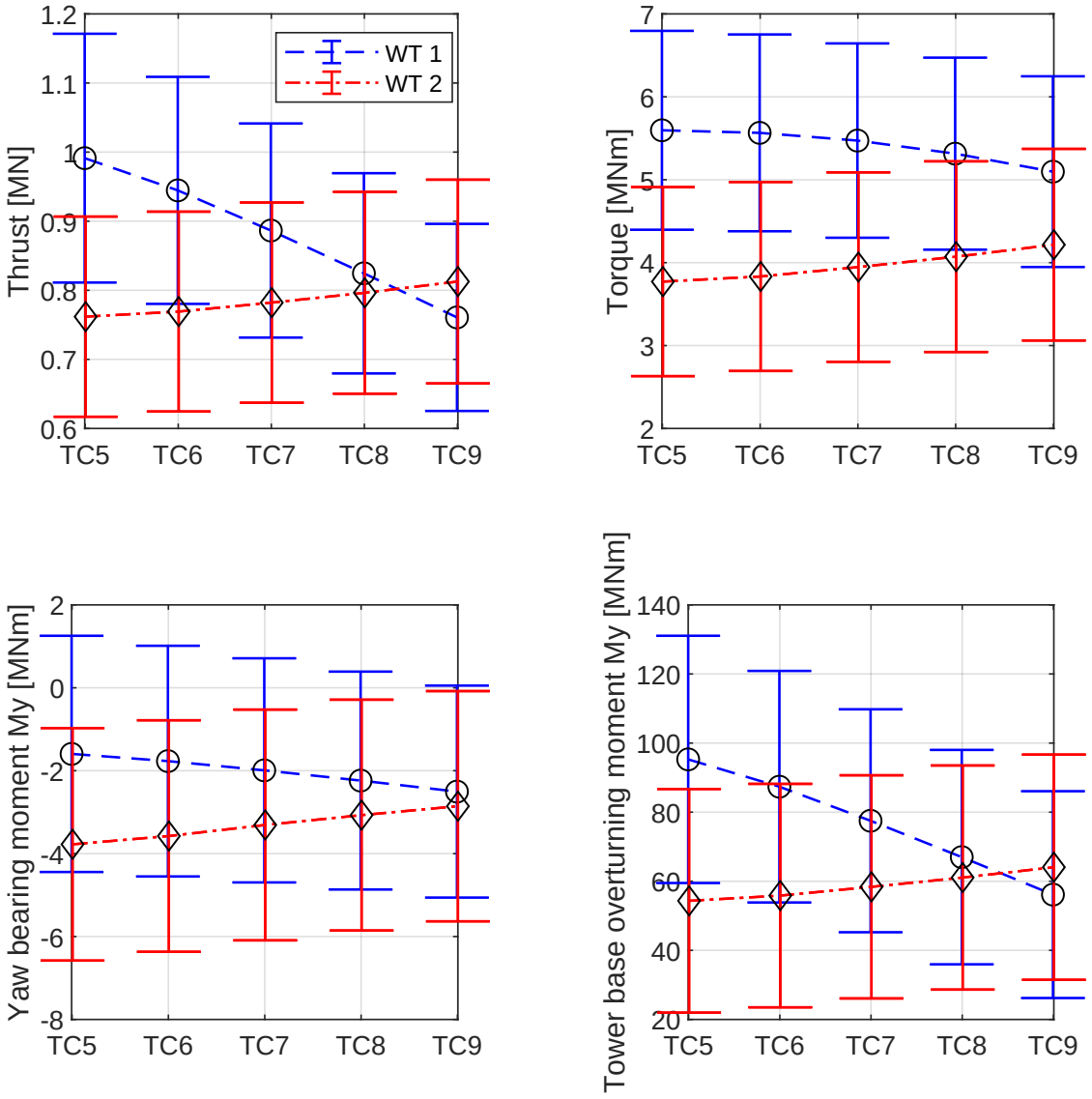

Figure 5.29: Mean (μ) and standard deviation (σ) of thrust (F_x), rotor torque (M_x), yaw bearing moment (M_y) acting on the tower and tower base overturning moment ($M_{y,base}$) for $TC_5 - TC_9$.

Table 5.9: Mean (μ) and standard deviation (σ) of the thrust force (F_x), yaw bearing moment (M_y) acting on the nacelle and rotor torque (M_x) for TC_5-TC_9.

Test case	Turbine number	$\mathbf{F}_x[MN]$		$\mathbf{M}_y[MNm]$		$\mathbf{M}_x[MNm]$	
		μ	σ	μ	σ	μ	σ
$\mathbf{TC}_5$	$\mathbf{WT}_1$	0.99	0.18	1.6	2.8	5.6	1.2
	$\mathbf{WT}_2$	0.76	0.14	3.8	2.8	3.8	1.1
$\mathbf{TC}_6$	$\mathbf{WT}_1$	0.94	0.16	1.8	2.8	5.6	1.2
	$\mathbf{WT}_2$	0.77	0.14	3.6	2.8	3.8	1.1
$\mathbf{TC}_7$	$\mathbf{WT}_1$	0.89	0.15	2.0	2.7	5.5	1.2
	$\mathbf{WT}_2$	0.78	0.14	3.3	2.8	3.9	1.1
$\mathbf{TC}_8$	$\mathbf{WT}_1$	0.82	0.14	2.2	2.6	5.3	1.2
	$\mathbf{WT}_2$	0.80	0.15	3.1	2.8	4.1	1.1
$\mathbf{TC}_9$	$\mathbf{WT}_1$	0.76	0.14	2.5	2.6	5.1	1.2
	$\mathbf{WT}_2$	0.81	0.15	2.9	2.8	4.2	1.2

5.3.3 Drivetrain Fatigue Results

Figure 5.30 shows the a pie chart of the fatigue damage for the bearings of TC_5, Table 5.10 shows absolute fatigue damage of the considered bearings and Table 5.11 shows relative fatigue damage having TC_5 as baseline.

Similar to subsection 5.2.3, the highest fatigue is found for the INP-A, INP-B, PLC-B and HS-A bearing.

For TC_5 the damage of the INP-A and PLC-B bearings is significantly larger for the downwind turbine.

The damage results of WT_1 for TC_0 and TC_5 are compared. It can be seen that the fatigue damage of TC_5 is larger than the fatigue damage of TC_0. Further more it can be seen that the standard deviation values of the global loads of TC_5 are also higher than these of TC_0. This deviation is probably due to the different coordinates of WT_1 in the turbulent wind field for wake steering and axial induction control.

The fatigue damage of the INP-A bearing of WT_2 for TC_5 is larger than the fatigue damage of the INP-A bearing of WT_2 for TC_0. This can be compared to M_y of both test cases, where it can be seen that M_y for TC_0 is lower than M_y for TC_5. M_y decreases in magnitude for an increase in β, while a similar decrease in INP-A fatigue is found for the corresponding test cases.

For an increase in β a decrease in fatigue damage for each bearing of WT_1 is found.

For WT_2 a significant decrease in fatigue damage for the INP-A bearing is found. Further more, a decrease for the PLC-A and the PLC-B bearing is found. The remaining bearings all increase in fatigue damage. This is similar to the results found for WT_2 of TC_0-TC_4.

The combined absolute fatigue damage decreases for larger blade pitch angles. Even when no power production increase is found, like TC_7, an overall decrease in fatigue damage is found which can lead to a reduction in cost by itself.

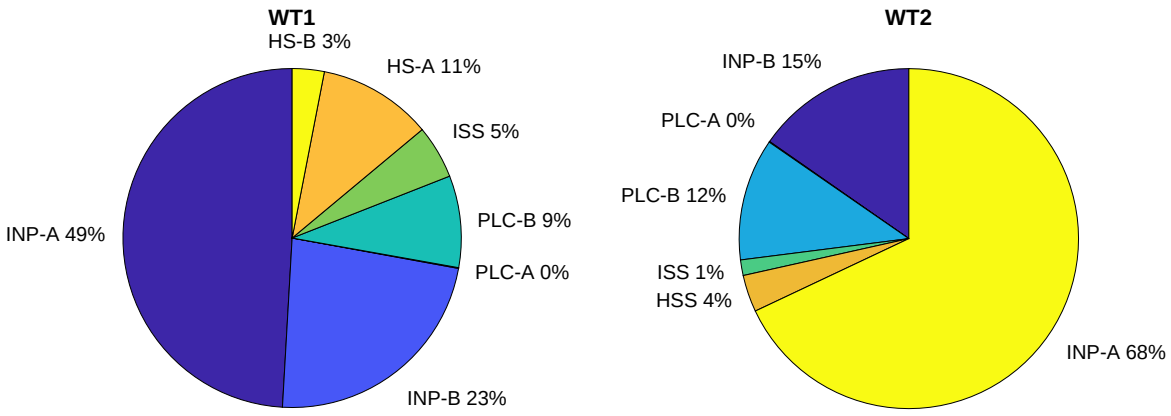

Figure 5.30: Pie chart of the fatigue damage of WT_1 and WT_2 for TC_5. For WT_1 IMS-PLC-A, IMS-PLC-B, IMS-A and IMS-B are grouped in ISS. For WT_2 HS-A and HS-B are grouped in HSS and IMS-PLC-A, IMS-PLC-B, IMS-A and IMS-B are grouped in ISS.

Table 5.10: One hour bearing fatigue damage results for TC_5-TC_9 for the bearings mentioned in section 3.7. Red indicates a bearing where the damage exceeds 5.0×10^{-5}, orange indicates a bearing between 5.0×10^{-6} and 5.0×10^{-5} and green indicates a bearing with less than 5.0×10^{-6} damage.

One hour bearing damage [-]	**WT$_1$**				
	TC_5	TC_6	TC_7	TC_8	TC_9
INP-A	6.2E-05	5.9E-05	5.6E-05	5.3E-05	5.0E-05
INP-B	2.9E-05	2.8E-05	2.6E-05	2.4E-05	2.2E-05
PLC-A	9.0E-08	8.5E-08	7.8E-08	7.2E-08	6.6E-08
PLC-B	1.1E-05	1.05E-05	9.8E-06	9.3E-06	8.8E-06
IMS-PLC-A	9.2E-09	9.1E-09	8.7E-09	8.2E-09	7.5E-09
IMS-PLC-B	1.9E-06	1.8E-06	1.7E-06	1.5E-06	1.3E-06
IMS-A	1.9E-06	1.9E-06	1.8E-06	1.6E-06	1.5E-06
IMS-B	2.6E-06	2.5E-06	2.4E-06	2.2E-06	1.9E-06
HS-A	1.4E-05	1.3E-05	1.3E-05	1.1E-05	9.7E-06
HS-B	3.8E-06	3.8E-06	3.5E-06	3.2E-06	2.8E-06
One hour bearing damage [-]	**WT$_2$**				
	TC_5	TC_6	TC_7	TC_8	TC_9
INP-A	9.2E-05	8.6E-05	7.9E-05	7.3E-05	6.9E-05
INP-B	2.1E-05	2.1E-05	2.2E-05	2.2E-05	2.3E-05
PLC-A	9.2E-08	8.9E-08	8.6E-08	8.4E-08	8.1E-08
PLC-B	1.6E-05	1.5E-05	1.4E-05	1.3E-05	1.2E-05
IMS-PLC-A	4.0E-09	4.1E-09	4.4E-09	4.7E-09	5.0E-09
IMS-PLC-B	5.5E-07	5.7E-07	6.2E-07	6.8E-07	7.5E-07
IMS-A	6.9E-07	7.1E-07	7.6E-07	8.2E-07	8.9E-07
IMS-B	7.6E-07	8.2E-07	8.9E-07	9.7E-07	1.1E-06
HS-A	3.6E-06	3.8E-06	4.2E-06	4.6E-06	5.1E-06
HS-B	1.1E-06	1.2E-06	1.3E-06	1.4E-06	1.5E-06

Table 5.11: Relative bearing fatigue damage for TC_5-TC_9 compared to TC_5 for the bearings mentioned in section 3.7. Green indicates a bearing that decreased with more than 10%, red indicates a bearing that increased with more than 10% and orange indicates the remaining bearings.

Relative bearing damage [%]	**WT$_1$**				
	TC_5	TC_6	TC_7	TC_8	TC_9
INP-A	0	-4.4	-9.8	-14.6	-18.6
INP-B	0	-4.8	-11.2	-17.2	-23.0
PLC-A	0	-5.5	-13.2	-20.0	-26.4
PLC-B	0	-4.8	-10.5	-15.8	-20.3
IMS-PLC-A	0	-1.4	-5.3	-11.3	-18.9
IMS-PLC-B	0	-2.5	-8.4	-17.3	-28.0
IMS-A	0	-2.1	-7.3	-15.1	-24.6
IMS-B	0	-2.5	-8.3	-17.0	-27.6
HS-A	0	-2.6	-8.9	-18.3	-29.5
HS-B	0	-2.5	-8.4	-17.3	-28.0
Relative bearing damage [%]	**WT$_2$**				
	TC_5	TC_6	TC_7	TC_8	TC_9
INP-A	0	-6.7	-14.5	-20.2	-25.1
INP-B	0	2.0	5.0	8.5	11.6
PLC-A	0	-3.1	-6.6	-8.8	-11.5
PLC-B	0	-5.9	-13.2	-18.7	-23.3
IMS-PLC-A	0	3.4	9.9	17.1	25.3
IMS-PLC-B	0	4.1	13.1	23.8	36.7
IMS-A	0	3.4	10.6	19.1	29.3
IMS-B	0	7.5	16.5	27.1	40.2
HS-A	0	4.7	14.7	26.8	41.8
HS-B	0	4.0	12.9	23.4	36.6

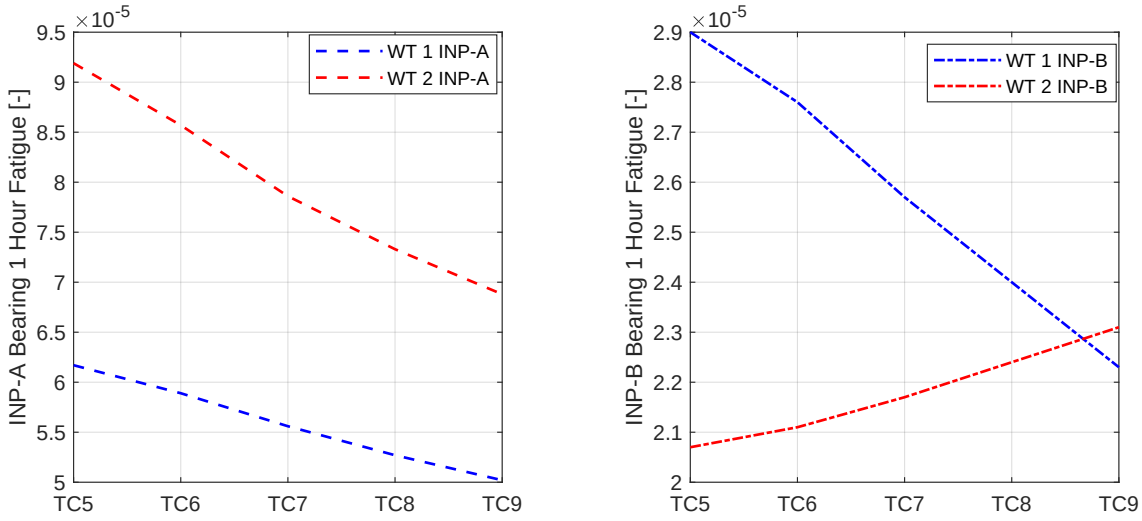

Figure 5.31: Main bearing fatigue of the INP-A and INP-B bearings for TC_5-TC_9.

5.3.4 2 Turbine Set-Up Induction Results For An Uniform Wind Field

For the two turbine set-up the test cases in Table 3.4 are considered.

Similar to subsection 5.2.4, an uniform wind field of with a wind speed of $8m/s$ at hub height is considered.

Figure 5.32 and 5.33 show the wake of the wind farm with the same coordinates as the two turbine set-up in the turbulent wind field, which can be found in Table 4.2. Figure 5.32 and 5.33 are visualisations of TC_5 and TC_9, which correspond to $\beta = 0°$ and $\beta = 4°$. The visualisation shows that the wake of WT_1 for TC_9 has a higher wind speed than the wake of WT_1 for TC_5.

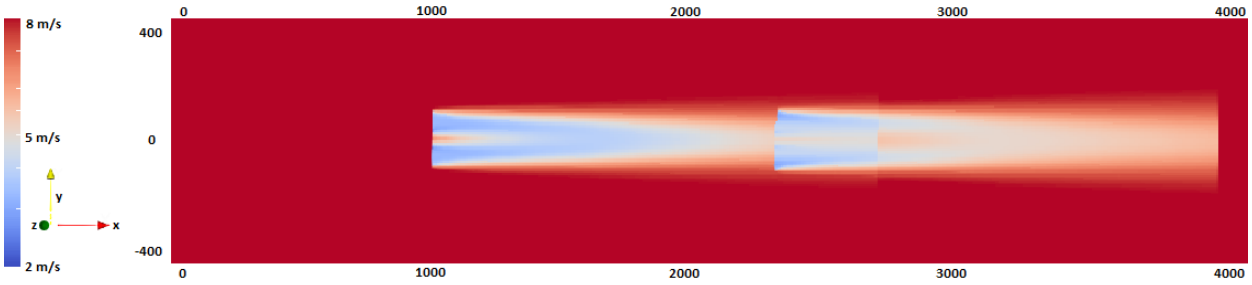

Figure 5.32: Flow visualization of the hub height wind speed for the reference pitch test case (TC_5) with a constant wind speed of 8 m/s at hub height.

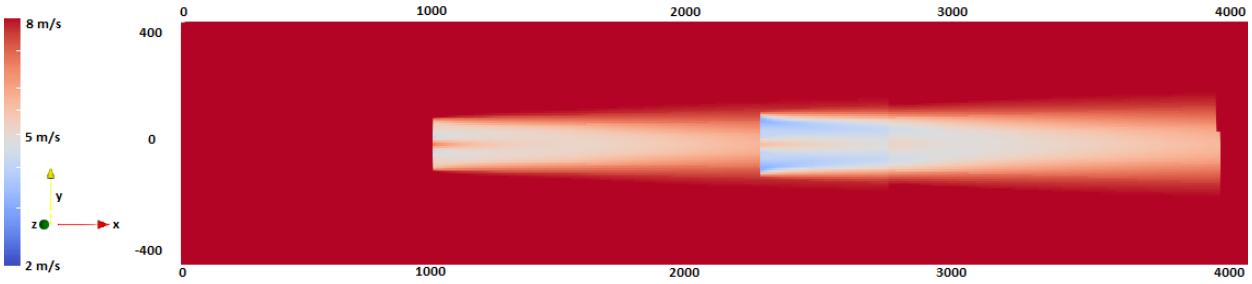

Figure 5.33: Flow visualization of the hub height wind speed for test case 9 (TC_9) with a constant wind speed of 8 m/s at hub height.

WT_1 is found to have a power production that is approximately 4% lower in steady wind for TC_5. The power production of WT_2 is 44% lower for TC_5, increasing faster with an increase in β in steady wind compared to the turbulent wind field.

The power production results for the uniform wind field and the turbulent wind field do not seem to differ significantly. Wind farm power production only increases with 0.19% for $\beta = 1°$, which is similar to the turbulent wind field case, meaning that power production is not significantly affected by turbulence intensity in this case and does not result in a significant power production increase.

The global loads can be found in Appendix C, Figure C.2.

Table 5.12: Power production in MW and power production increase in % for each wake induction test case considering each turbine separately and both turbines together with a steady wind speed of 8 m/s.

Test case	Turbine number	Power production [MW]		Power production increase[%]	
		Single WT	WF	Single WT	WF
TC_5	WT_1 WT_2	3.63 1.58	5.21	0 0	0
TC_6	WT_1 WT_2	3.57 1.65	5.22	-1.57 4.22	0.19
TC_7	WT_1 WT_2	3.47 1.73	5.20	-4.37 9.51	-0.15
TC_8	WT_1 WT_2	3.33 1.84	5.17	-8.13 16.6	-0.61
TC_9	WT_1 WT_2	3.16 1.96	5.12	-12.8 24.2	-1.56

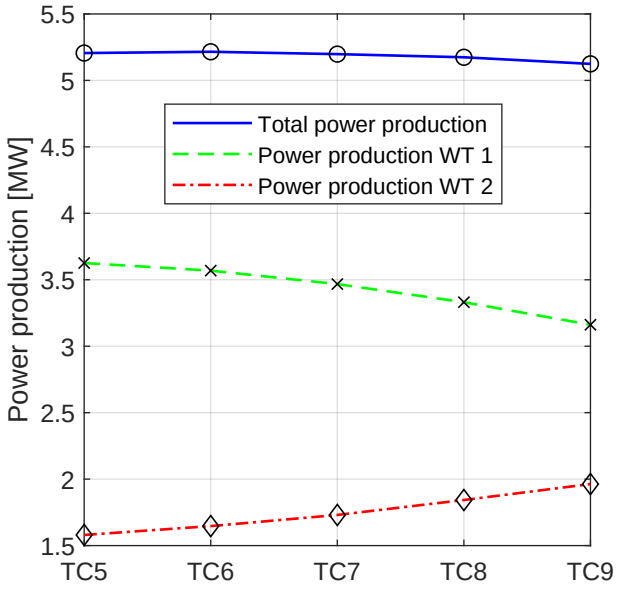

Figure 5.34: Total power production and power production of WT_1 and WT_2 for each induction control test case under constant inflow wind.

5.3.5 4 Turbine Set-Up Induction Results For An Uniform Wind Field

The two wind turbine set-up is extended to a four wind turbine set-up with similar spacing in X and Y direction, which can be found in subsection 4.2.2. The same test cases as for the two turbine set-up are used, where the blades of WT_1, WT_2 and WT_3 are each

pitched to the angle stated in Table 4.4. Figure 5.35 and 5.36 show the flow visualisation of the $XZ-plane$ for TC_5 and TC_9.

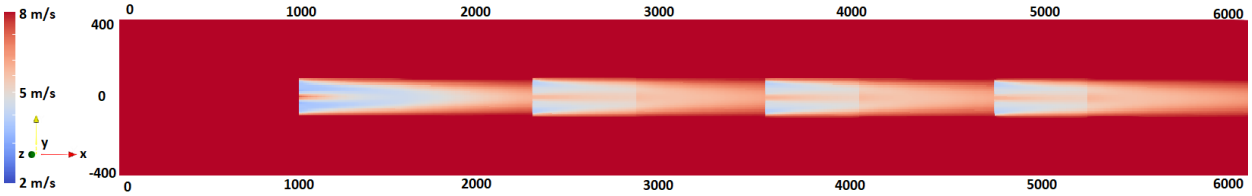

Figure 5.35: Flow visualization of the hub height wind speed for the reference pitch test case (TC_{12}) with a constant wind speed of 8 m/s at hub height.

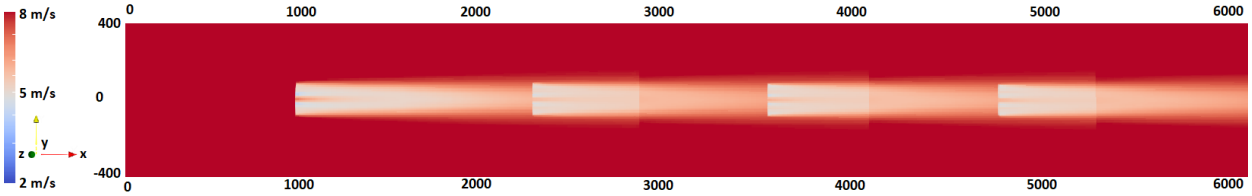

Figure 5.36: Flow visualization of the hub height wind speed for test case 9 (TC_9) with a constant wind speed of 8 m/s at hub height.

In Table 5.13, Figure 5.37 and Figure 5.38 the power production of WT_1, WT_2 and WT_1 and WT_2 together can be found. For WT_1 similar power production results are found for each test case compared to the two turbine set-up. For an increase in β, an increase in power production for WT_2, WT_3 and WT_4 is found, resulting in a 10.3% increase in wind farm power production for $\beta = 3°$, increasing the power production of WT_3 with 56.9%.

In Figure 5.38 it can be seen that due to wake overlap of WT_1 and WT_2 the power production of WT_3 around $\beta = 0°$ is significantly lower increasing with increased blade pitch angles. The power production of WT_4 is similar to the power production of WT_2. With an increase in β, the power production of WT_3 increases and surpasses WT_2 and WT_4 around TC_7. Power production of WT_4 is higher than WT_2 for TC_8 and TC_9, which can be explained since WT_4 is not pitching its blades, while WT_1, WT_2 and WT_3 are. After TC_8, the increase in power production of WT_2-WT_4 does not exceed the decrease in power production of WT_1, thus the maximum power production for the four wind turbine case is reached at $\beta = 3°$.

Table 5.13: Power production in MW and power production increase in % for each induction test case at hub height considering each turbine separately and the four turbines together with a steady wind speed of 8 m/s.

Test case	**Turbine number**	**Power production [MW]**		**Power production increase [%]**	
		Single WT	**WF**	**Single WT**	**WF**
TC_{12}	**WT_1**	3.62	7.89	0	0
	WT_2	1.53		0	
	WT_3	1.16		0	
	WT_4	1.58		0	
TC_6	**WT_1**	3.57	8.26	-1.47	4.74
	WT_2	1.63		6.80	
	WT_3	1.44		23.6	
	WT_4	1.63		3.08	
TC_7	**WT_1**	3.47	8.57	-4.26	8.67
	WT_2	1.72		12.1	
	WT_3	1.69		45.6	
	WT_4	1.70		7.84	
TC_8	**WT_1**	3.33	8.71	-8.03	10.3
	WT_2	1.76		15.3	
	WT_3	1.82		56.9	
	WT_4	1.79		13.3	
TC_9	**WT_1**	3.16	8.62	-12.7	9.22
	WT_2	1.77		15.4	
	WT_3	1.87		60.8	
	WT_4	1.82		15.5	

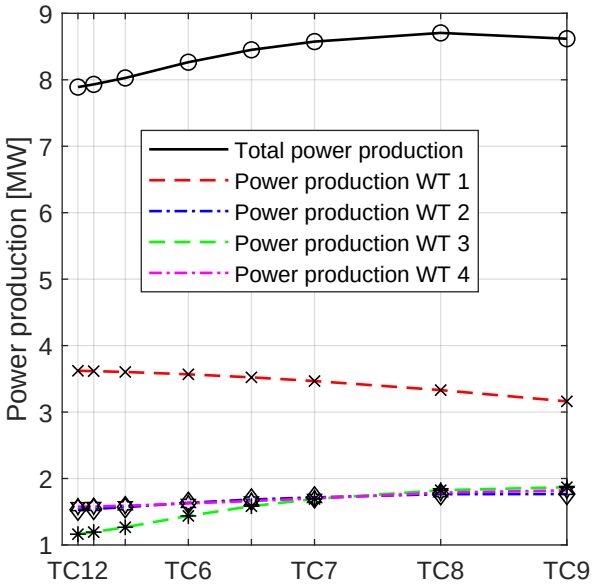

Figure 5.37: Power production for TC_{12} and TC_6-TC_9 with a constant wind speed of 8 m/s at hub height.

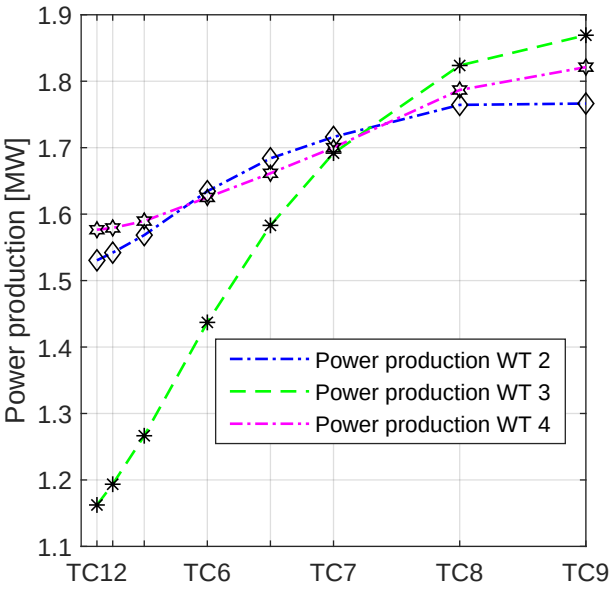

Figure 5.38: Power production of WT_2, WT_3 and WT_4 for TC_{12} and TC_6-TC_9 with a constant wind speed of 8 m/s at hub height.

6 | Cost Results

For the cost calculation the relative increase in profit is considered. Figure 6.1 and 6.2 show the profit increase in euros for each test and repair case for the cost calculation discussed in section 3.8. Four different repair cases are considered. Each Figure represents one repair case. Starting with RC_1 at the top left, RC_2 at the top right, RC_3 at the bottom left and RC_4 at the bottom right.

First the results for wake steering control are discussed in section 6.1 and then the results for induction control are discussed in section 6.2.

Finally, the profit for the four turbine case is shown in section 6.3 and 6.4.

The four considered repair cases can be found in section 3.8.

6.1 Wake Steering Control

Figure 6.1 shows the increase in profit for TC_1-TC_4 taking TC_0 as baseline profit. For RC_1 and RC_2 a decrease in profit is found. This is due to the significant increase in fatigue damage of the INP-A bearing for an increase in γ. The same can be seen for RC_2, where the decrease in profit is found to be less significant than for RC_1. The repair of HS-A and HS-B is less expensive for RC_2, while for increased γ, the fatigue on these two bearings increases significantly. This results in a larger profit for RC_2 compared to RC_1.

For RC_3 and RC_4 the INP-A bearing fatigue damage is not considered. The results show an increase in profit for an energy price ranging from €40,- to €75,-. TC_2 shows the largest increase, while TC_1 shows the smallest increase in profit. For both repair cases TC_4 starts with an increased profit over TC_3, but decreases when the price of energy increases. For a price of energy around €40/MWh decreased fatigue damage for TC_4 results in a higher increase in profit.

When the price of energy increases, the influence of fatigue damage on the profit results becomes less noticeable. Instead the profit due to increased power production found for TC_3 exceeds the profit due to fatigue damage decrease for TC_4. This occurs for both RC_3 and RC_4.

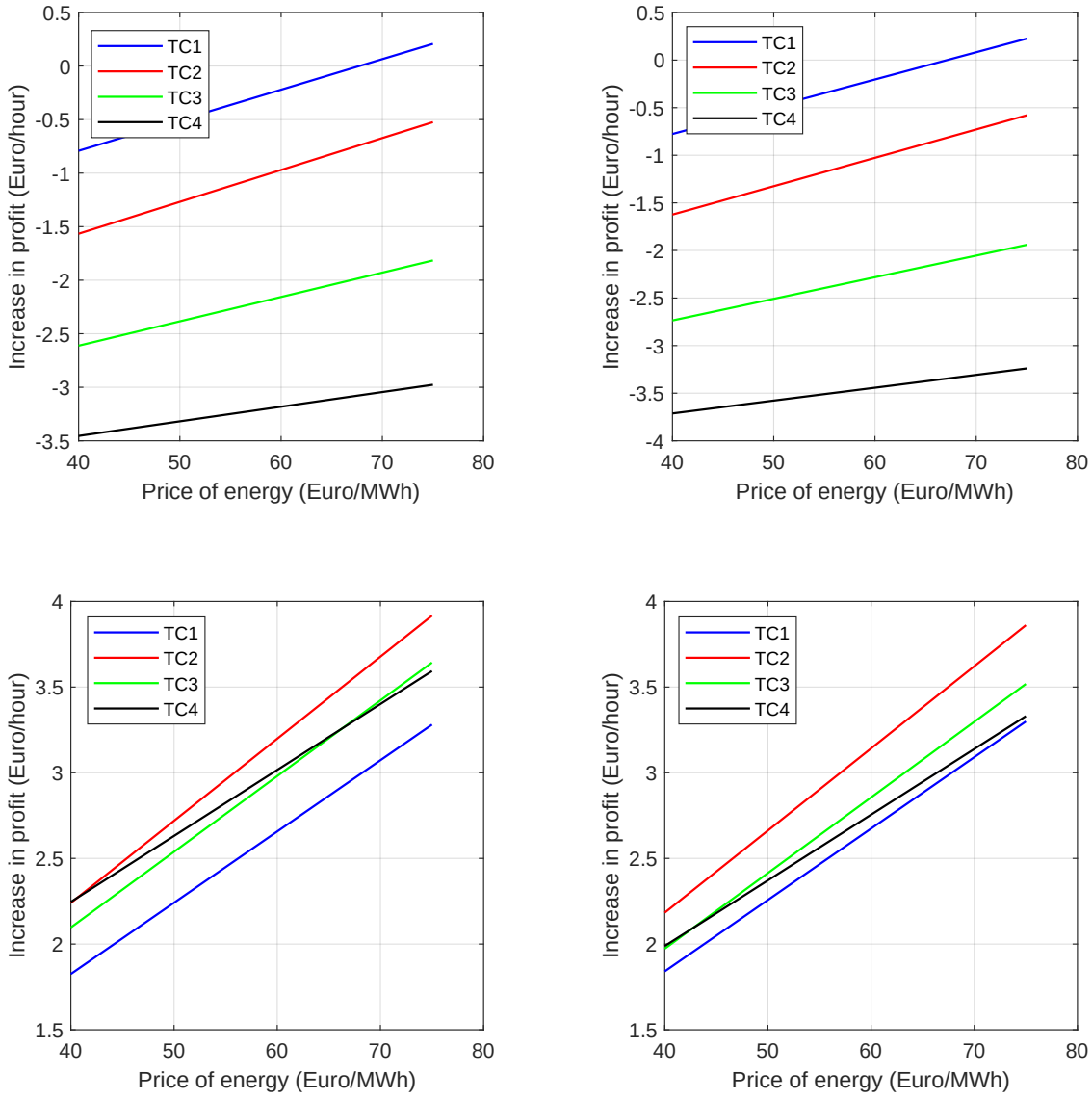

Figure 6.1: Increase in profit for TC_0-TC_4 of RC_1 (top left), RC_2 (top right), RC_3 (bottom left) and RC_4 (bottom right).

6.2 Induction Control

Figure 6.2 shows the increase in profit for TC_6-TC_9 taking TC_5 as baseline profit. For each repair case an increase in profit is found. This is due to the total decrease in fatigue damage of the drivetrain for an increase in β, where RC_1 and RC_2 result in the largest increase in profit, caused by the decrease in fatigue damage of the INP-A bearing for WT_1 and WT_2.

Dependent on the price of energy, different optimal test cases are found. TC_9 gives the largest increase in profit for RC_1 and RC_2, while giving a decrease in power production of 2.24% compared to TC_5. TC_7 and TC_8 result in the highest increase in profit for the largest price range of RC_3 and RC_4, where TC_7 produces the largest amount of power and TC_8 results in less fatigue damage.

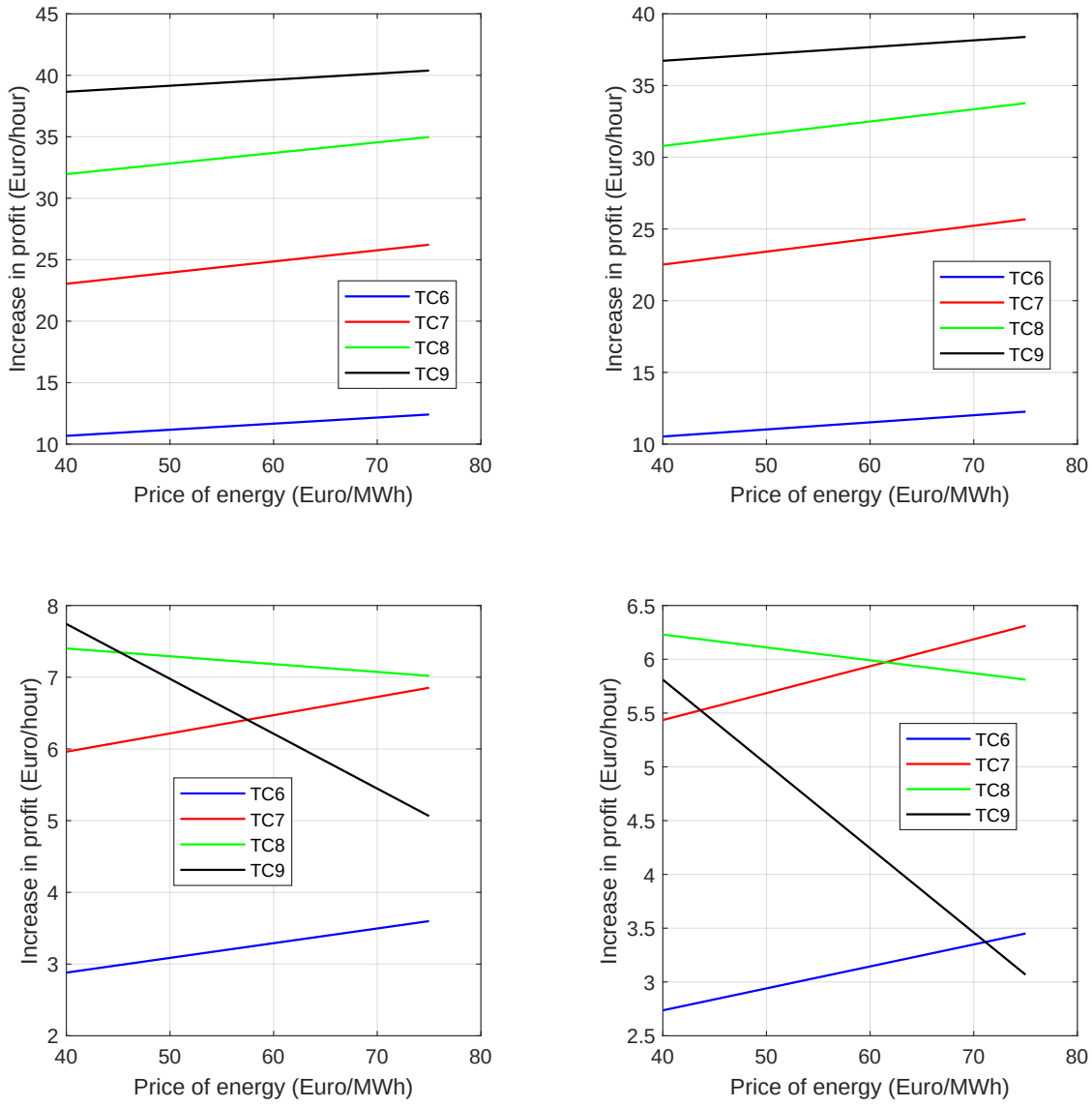

Figure 6.2: Increase in profit for TC_5-TC_9 for RC_1 (top left), RC_2 (top right), RC_3 (bottom left) and RC_4 (bottom right).

6.3 4 turbine Set-Up : Wake Steering Control

Figure 6.3 shows the increase in profit for TC_1, TC_4, TC_{10} and TC_{11} having TC_0 as baseline profit. The increase in profit is significant, ranging from €30,- to €130,- per hour, due to the large increase in power production.

From Figure 6.1 it can be seen that due to wake steering the profit decreases with only €3.50 per hour for TC_4, which will result in a decrease of $\sim$ €7,- per hour for four turbines. Even when the cost of fatigue is found to be significantly higher for this case, the amount of profit due to the power production increase still results in a significant profit increase.

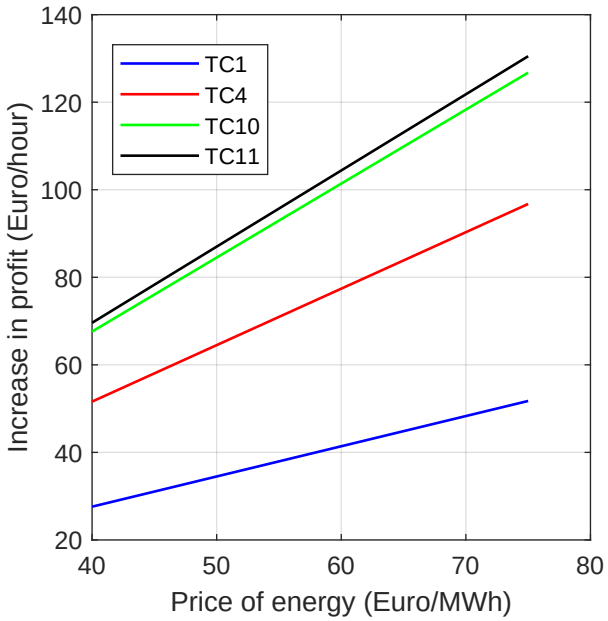

Figure 6.3: Increase in profit for TC_1-TC_4 for the 4 turbine set-up without considered fatigue loads.

6.4 4 turbine Set-Up : Axial Induction Control

Figure 6.4 shows the increase in profit for TC_6-TC_9 having TC_5 as baseline profit. The increase in profit is again significant.

In section 6.2 the increase in profit is mainly due to decrease in fatigue damage, while the increase in profit in section 6.4 is due to the increase in power production. It cannot be assumed that a similar decrease in fatigue damage occurs for the four turbine case in low turbulent wind, but when assuming no damage increase or at least a small damage decrease occurs for this case, a significant increase in profit can be found ranging from €15,- to €60,- per hour.

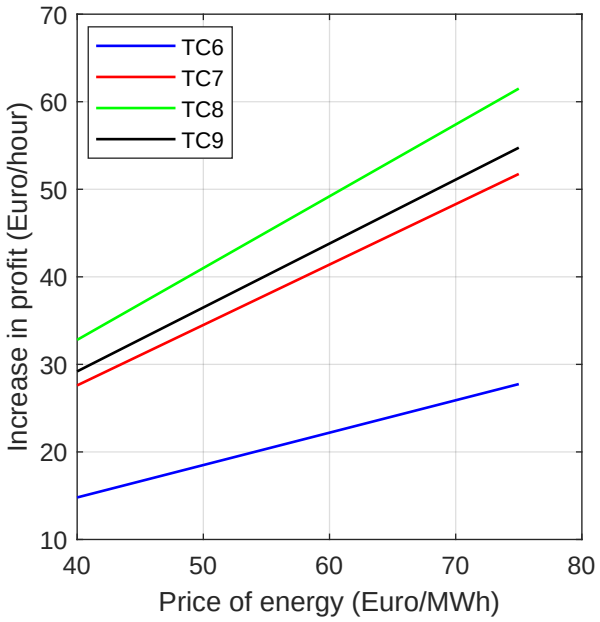

Figure 6.4: Increase in profit for TC_6-TC_9 for the 4 turbine set-up without considered fatigue loads.

7 | Conclusion

In this thesis the research objective is adressed:

To create and apply a methodology to determine hourly profit taking into account wind farm power production and drivetrain bearing damage.

Below, the main research question will be answered as well as the sub-questions formulated in section 1.3. The main research question is answered by first calculating the power production and global loads for individual wind turbines in a wind farm layout. Different test cases with varying angles in yaw and blade pitch are considered. The global loads are used as input for the DTU10MW drivetrain model developed by NTNU. Main bearing fatigue damage is calculated and profit is calculated for varying prices of energy, where the profit consists of profit due to power production and a decrease in profit due to fatigue damage.

As a general conclusion, both wake steering and axial induction control can result in an increase in profit when power production and bearing fatigue is considered. This applies for high turbulent and low turbulent wind fields, where low turbulent wind fields cause a larger increase in power production.

Wake steering control results in a larger increase in power production than axial induction control, but also results in larger fatigue loads than axial induction control. Both control manoeuvres are effective under different conditions, where for wake steering partial wake shading is considered, while for axial induction control full wake shading is considered.

For a wind speed of $8m/s$ waves having a peak period ranging from $4s$ to $10s$ will not conflict with eigenfrequencies and rotor frequencies of the wind turbine.

Also, fixing the turbine results in comparable global loads, power production results and frequency domain spectra, thus general conclusions made that depend on global loads and power production of the specific nautilus 10MW wind turbine also apply for 10MW bottom-founded wind turbines.

Decreasing the turbulence intensity of the ambient wind results in a significant increase in power production for wake steering control, since a lower turbulence intensity results in less wake recovery due to shear with the ambient wind, resulting in a larger potential to increase power production. Increasing the size of the wind farm from 2 to 4 wind turbines results in an increase in power production for both wake steering control and axial induction control, since more downwind turbines will profit from upwind control manoeuvres when a larger wind farm is considered.

Wind turbine wakes will cause a significant increase in fatigue damage on the downwind turbine for the bearings that take the thrust loads, like the INP-A bearing, while it has a limited effect on the fatigue damage of the intermediate and high speed shaft of the downwind turbine.

Wake steering control

Global loads : With an increase in yaw for the upwind turbine, a decrease in thrust and torque is found for WT_1, while an increase in thrust and torque is found for WT_2. A significant increase is found for the yaw bearing moment of WT_1, while a small decrease is found for the yaw bearing moment of WT_2.

Drivetrain damage : For WT_1 the low speed shaft damage increases, while both the intermediate and high speed shaft damage decreases. For WT_2 the INP-A and PLC-B bearing fatigue damage decreases slightly while the fatigue damage on the remaining bearings increases.

Power production and profit results : For the high turbulent wind field an increase in power production of 0.78% is found for $\gamma = 7^\circ$. Depending on the energy price this would cause either a small increase or a small decrease in profit due to the increase in fatigue damage of the drivetrain main bearings, which can make wake steering arguably not worth the effort in highly turbulent wind fields.

For the uniform wind field for both the two and four turbine set-up a significant increase in power production of 4.78% for $\gamma = 15^\circ$ and 16.6% for $\gamma = 20^\circ$ is found respectively. Depending on the energy price considered, the increase in profit ranges from €70,- to €130,- per hour for $\gamma = 20^\circ$ of the four turbine set-up. It should be noted that in reality uniform wind fields do not exist, thus this increase in power production and profit serves as limit to the increase that could be reached for this set-up. However, even when a portion of the stated profit can be realized in low turbulent wind fields, wake steering control can function as a very cost effective control manoeuvre.

Further more it is found that wake steering on floating wind turbines will cause a counter yaw of the floater which is around 8.8% of the yaw angle for $0 < \beta < 10$.

Axial induction control

Global loads : With an increase in blade pitch for the upwind turbine, a significant decrease in thrust, a decrease in torque and an increase in yaw bearing moment for WT_1 is found, while an increase in thrust and torque and a decrease in yaw bearing moment for WT_2 is found.

Drivetrain damage : For WT_1 a significant decrease in fatigue damage for each bearing is found, since pitching the blades will result in a decrease in thrust and rotor torque. For WT_2 a decrease in fatigue damage of the low speed shaft is found, while an increase in fatigue damage for the intermediate and high speed shaft is found.

Power production and profit results : For the high turbulent wind field an increase in power production of 0.17% for $\beta = 1^\circ$ is found. Due to an overall decrease in fatigue damage over both wind turbines, an increase in profit can be found ranging from €3,- to €37.50 per hour dependent on both the price of energy considered and the repair case used.

In the uniform wind field for both the two and four turbine set-up an increase in power production of 0.19% for $\beta = 1^\circ$ and 10.9% for $\beta = 3^\circ$ is found. Depending on the energy price considered, the increase in profit ranges from €30,- to €60,- per hour for $\beta = 3^\circ$ of the four turbine set-up.

8 | Challenges and Recommendations

A high TI was chosen for the simulation cases. Running the simulation cases with a TI that occurs very often in the north sea might result in results that can be used in more occasions. A study is done where the Mann turbulence model parameters are calculated for the north sea in Cheynet et al. [67], where a good agreement was found for wind speeds ranging from 14 $\frac{m}{s}$ to 28 $\frac{m}{s}$, which is above rated. The effectiveness of wake steering and axial induction control occurs below rated, since below rated power production is maximized resulting in the largest velocity deficits behind the rotor. In the future it might be of use to use parameters found in this article.

Bearing fatigue damage is based on pitting. This is not the only cause of failure for bearings. In the future more failure mechanisms could be considered.

The gearbox gears are not taken into account. Taking those into account, especially the high speed parallel stage gear, will result in more complete results. Further more, taking tower fatigue, blade fatigue and mooring line fatigue into account, could result in a good representative model for fatigue damage.

In order to determine downtime due to failure and cost of failure, assumptions were made based on literature found. This literature was mainly applied on small wind turbines. Due to limited knowledge available on cost of failure for large offshore wind turbines, upscaling assumptions had to be made, which makes the cost and downtime results not highly verifiable. Also, stop time was not taken into account in the downtime calculations.

Further more, specific bearing prices are not considered. Considering a different bearing price for each bearing could result in different profit results.

Bibliography

[1] Wind explained, history of wind power, April 2019. URL : https://www.eia.gov/energyexplained/wind/history-of-wind-power.php (accessed: 15/01/2020).

[2] Zachary Shahan. History of wind turbines, November 2011. URL : https://www.renewableenergyworld.com/2014/11/21/history-of-wind-turbines/ (accessed: 15/01/2020).

[3] IRENA (2019). *Renewable power generation cost in 2018*. International Renewable Energy Agency, Abu Dhabi. ISBN 978-92-9260-126-3.

[4] Europe powered by green energy, 2017. URL : https://orsted.com/-/media/WWW/Docs/Corp/COM/About-us/North-seas/rsted-Paper-01---Europe-Powered-by-Green-Energy_UK.ashx (accessed: 12/02/2020).

[5] M. Díaz, R. Cardenas, B. Mauricio Espinoza, A. Mora, and F. Rojas. A novel lvrt control strategy for modular multilevel matrix converter based high-power wind energy conversion systems. In *2015 Tenth International Conference on Ecological Vehicles and Renewable Energies (EVER)*, pages 1–11, March 2015.

[6] Öztürk E. *Wake induced power deficit analysis on wind turbines in forested moderately complex terrain using SCADA data [dissertation on the Internet]*. University of Uppsala, 2018. http://urn.kb.se/resolve?urn=urn:nbn:se:uu:diva-346639.

[7] Stoyan Kanev. Dynamic wake steering and its impact on wind farm power production and yaw actuator duty. *Renewable Energy*, 146:9 – 15, 2020.

[8] Michael F. Howland, Sanjiva K. Lele, and John O. Dabiri. Wind farm power optimization through wake steering. *Proceedings of the National Academy of Sciences*, 116(29):14495–14500, 2019.

[9] M.S. Adaramola and P.-Å. Krogstad. Experimental investigation of wake effects on wind turbine performance. *Renewable Energy*, 36(8):2078 – 2086, 2011.

[10] Medici D. Dahlberg. *Potential improvement of wind turbine array efficiency by active wake control*. 2003. In Proceedings of European Wind Energy Conference, Madrid, Spain.

[11] Jan Wagenaar, L Machielse, and J Schepers. Controlling wind in ecn's scaled wind farm. *Proc. Europe Premier Wind Energy Event*, 1, 01 2012.

[12] Maryam Soleimanzadeh, Rafael Wisniewski, and Kathryn Johnson. A distributed optimization framework for wind farms. *Journal of Wind Engineering and Industrial Aerodynamics*, 123:88 – 98, 2013.

[13] Angel Jimenez, Antonio Crespo, and Emilio Migoya. Application of a les technique to characterize the wake deflection of a wind turbine in yaw. *Wind Energy*, 13:559 – 572, 09 2009.

[14] P.M.O. Gebraad. *Data-Driven Wind Plant Control*. PhD thesis, TU Delft, 2014.

[15] Paul Fleming, Andrew Ning, Pieter Gebraad, and Katherine Dykes. Wind plant system engineering through optimization of layout and yaw control. *Wind Energy*, 19, 03 2015.

[16] Pieter Gebraad, Jared J. Thomas, Andrew Ning, Paul Fleming, and Katherine Dykes. Maximization of the annual energy production of wind power plants by optimization of layout and yaw-based wake control. *Wind Energy*, 20(1):97–107, 2017.

[17] Søren Juhl Andersen & Jens N. Sørensen. *Aerodynamics for Offshore Wind Farms*. DTU, 2018. Part of the Offshore Wind Energy course offered by DTU, URL : `https://wem.dtu.dk/courses/offshore-wind-energy`.

[18] J Bartl and L Sætran. Experimental testing of axial induction based control strategies for wake control and wind farm optimization. *Journal of Physics: Conference Series*, 753:032035, sep 2016.

[19] Karl Nilsson, Stefan Ivanell, Kurt Schaldemose Hansen, Robert Flemming Mikkelsen, Jens Nørkær Sørensen, Simon-Philippe Breton, and Dan Henningson. Large-eddy simulations of the lillgrund wind farm. *Wind Energy*, 18(3):449–467, 2015.

[20] T. Horvat, V. Spudić, and M. Baotić. Quasi-stationary optimal control for wind farm with closely spaced turbines. pages 829–834, 2012.

[21] Kathryn E. Johnson and Geraldine Fritsch. Assessment of extremum seeking control for wind farm energy production. *Wind Engineering*, 36(6):701–715, 2012.

[22] J. R. Marden, S. D. Ruben, and L. Y. Pao. A model-free approach to wind farm control using game theoretic methods. *IEEE Transactions on Control Systems Technology*, 21(4):1207–1214, 2013.

[23] J G Schepers and S P van der Pijl. Improved modelling of wake aerodynamics and assessment of new farm control strategies. *Journal of Physics: Conference Series*, 75:012039, jul 2007.

[24] Jennifer Annoni, Peter J Seiler Jr, Kathryn Johnson, Paul Fleming, and Pieter Gebraad. Evaluating wake models for wind farm control. January 2014.

[25] Jay Goit and Johan Meyers. Analysis of turbulent flow properties and energy fluxes in optimally controlled wind-farm boundary layers. *Journal of Physics: Conference Series*, 524:012178, 06 2014.

[26] E. Bot H. Hendriks L. Machielse, S. Barth and G. Schepers. Evaluation of "heat and flux" farm control. 2007. final report. Technical Report ECN-E–07-105, Energy Centre of the Netherlands.

[27] Ervin Bossanyi. Combining induction control and wake steering for wind farm energy and fatigue loads optimisation. *Journal of Physics: Conference Series*, 1037:032011, jun 2018.

[28] Kenneth Thomsen and Poul Sørensen. Fatigue loads for wind turbines operating in wakes. *Journal of Wind Engineering and Industrial Aerodynamics*, 80(1):121 – 136, 1999.

[29] Soo-Hyun Kim, Hyung-Ki Shin, Young-Chul Joo, and Keon-Hoon Kim. A study of the wake effects on the wind characteristics and fatigue loads for the turbines in a wind farm. *Renewable Energy*, 74:536 – 543, 2015.

[30] D. S. Zalkind and L. Y. Pao. The fatigue loading effects of yaw control for wind plants. In *2016 American Control Conference (ACC)*, pages 537–542, 2016.

[31] A Bustamante, L Vera-Tudela, and M Kühn. Evaluation of wind farm effects on fatigue loads of an individual wind turbine at the EnBW baltic 1 offshore wind farm. *Journal of Physics: Conference Series*, 625:012020, jun 2015.

[32] Björn Schmidt, John King, Graeme Mccann, and Kimon Argyriadis. Wake loads and fatigue load certification in offshore wind farms. 11 2011.

[33] Hang Meng, Fue-Sang Lien, Gregory Glinka, Li Li, and Jinhua Zhang. Study on wake-induced fatigue on wind turbine blade based on elastic actuator line model and two-dimensional finite element model. *Wind Engineering*, 43(1):64–82, 2019.

[34] Tana Tjhung Yung-Li Lee. *Metal Fatigue Analysis Handbook*. Elsevier, 2012. `https://www.sciencedirect.com/topics/engineering/rainflow-counting/pdf` (accessed: 29/04/2020).

[35] Shuangwen Shawn Sheng. *Report on Wind Turbine Subsystem Reliability - A survey of Various Databases*. National Renewable Energy Laboratory (NREL), June 2013. NREL/PR-5000-5911.

[36] Sten Tronæs Frandsen and M.L. Thøgersen. Integrated fatigue loading for wind turbines in wind farms by combining ambient turbulence and wakes. *Wind Engineering*, 23:327–339, 1999.

[37] Crespo A. Vermeer Nord-Jan, Sørensen J. *Wind turbine wake aerodynamics.* Progress in Aerospace Sciences - PROG AEROSP SCI. 39. 467-510., 2003. 10.1016/S0376-0421(03)00078-2.

[38] Sowfa. URL : `https://nwtc.nrel.gov/SOWFA` (accessed: 19/02/2020).

[39] Fast.farm. URL : `https://nwtc.nrel.gov/FASTFarm` (accessed: 19/02/2020).

[40] Openfast. URL : `https://nwtc.nrel.gov/OpenFAST` (accessed: 19/02/2020).

[41] Madsen Aagaard H. Bingöl F. Mann J. Ott S. Sørensen J. N. ... Mikkelsen R. Larsen, G. C. *Dynamic wake meandering modeling*. 2007, Roskilde, Denmark : Risø National Laboratory. orskningscenter Risoe. Risoe-R, No. 1607(EN).

[42] International Electrotechnical Commision (IEC) 2005. *Wind turbines- Part 1: Deign Requirements*. Tech. Rep. IEC61400-1.

[43] Izumi Y Coté OR. (1972) Kaimal JC, Wyngaard JC. *Spectral characteristics of sur face-layer turbulence.* Q.J.R. Meteorol. Soc., 98: 563-589. https://doi.org/10.1002/qj.49709841707.

[44] J. Mann. *The spatial structure of neutral atmospheric surface-layer turbulence.* Journal of Fluid Mechanics, 273, 141-168., 1994.

[45] J. Mann. *Wind field simulation.* Probabilistic Eng Mech. 1998;13(4):269-282., 1998.

[46] Shuaishuai Wang et al. *On Initial Design and Modelling of a 10 MW Medium Speed Drivetrain for Offshore Wind Turbines*. 2019 *J. Phys.: Conf. Ser.* **1356** 012024.

[47] Nejad A R Wang S and Moan T. *On design, modelling, and analysis of a 10-MW medium-speed drivetrain for offshore wind turbines*. *Wind Energy*. 2020; 23: 1099– 1117. https://doi.org/10.1002/we.2476.

[48] Simpack. multi body system software. URL : http://www.simpack.com(accessed: 19/02/2020).

[49] Wei-Liang Wei-Liang Jin Yong Bai. *Marine Structural Design (Second Edition)*. Elsevier, 2015. https://www.sciencedirect.com/topics/engineering/s-n-curve/pdf (accessed: 29/04/2020).

[50] Teresa L.M. Morgado. *Handbook of Materials Failure Analysis with Case Studies from the Aerospace and Automotive Industries*. Elsevier, 2016. https://www.sciencedirect.com/topics/engineering/palmgren-miner-rule/pdf (accessed: 29/04/2020).

[51] J. J. Barradas-Berglind and Rafael Wisniewski. Representation of fatigue for wind turbine control. *Wind Energy*, 19(12):2189–2203, 2016.

[52] Amir Rasekhi Nejad, Zhen Gao, and Torgeir Moan. On long-term fatigue damage and reliability analysis of gears under wind loads in offshore wind turbine drivetrains. *International Journal of Fatigue*, 61:116 – 128, 2014.

[53] DTU 10 MW RWT FAST model URL : https://rwt.windenergy.dtu.dk/dtu10mw/dtu-10mw-rwt (accessed: 18/01/2020).

[54] Christian Bak et al. *Description of the DTU 10 MW Reference Wind Turbine*. DTU Wind Energy, June 2013. DTU Wind Energy Report-I-0092.

[55] Jesús M. Busturi. *Nautilus Floating Solutions*. Spain Offshore Wind Power, February 28th, 2017. http://jwpa.jp/pdf/NAUTILUS_Presentation.pdf (accessed: 08/02/2020).

[56] Pegalajar-Jurado A et al. *State-of-the-art models for the two LIFES50+ 10 MW floater concepts*. 2018. Tech. Rep. D4.5, LIFES50+.

[57] Kelly M Berg J. *Atmospheric turbulence modelling, synthesis, and simulation*. Institution of Engineering and Technology, 2019. pp. 183-216 https://doi.org/10.1049/PBPO125F.

[58] G. Batchelor. *Introduction to Fluid Mechanics*. 2000. URL : https://doi.org/10.1017/CBO9780511800955.

[59] David Sharpe Ervin Bossanyi Tony Burton, Nick Jenkins. *Wind Energy Handbook, Second Edition*. John Wiley Sons, 2011. ISBN: 978-0-470-69975-1.

[60] Honnery D. Soria J. O'Neill P. L., Nicolaides D. *Autocorrelation Functions and the Determination of Integral Length with Reference to Experimental and Numerical Data*. 15th Australasian Fluid Mechanics Conference, 13–17 December 2004.

[61] K. Kimura. *Innovative Bridge Design Handbook*. Butterworth Heinemann, 2016. Chapter 3 - Wind loads, pp. 37-48, https://doi.org/10.1016/B978-0-12-800058-8.00003-7.

[62] Von Karman T. *Progress in the statistical theory of turbulence*. 1948. Proceedings of The National Academy of Sciences. Vol. 34, pp. 530–539.

[63] Landberg L. Højstrup J. Frank H.P. Petersen E.L., Mortensen N.G. *Wind power meteorology Part I: Climate and turbulence*. 1998. Wind Energy **1**, 1, 2–22.

[64] Wasp. URL : https://www.wasp.dk/ (accessed: 23/03/2020).

[65] Hawc2. URL : http://www.hawc2.dk/ (accessed: 23/03/2020).

[66] Turbsim. URL : https://nwtc.nrel.gov/TurbSim (accessed: 23/03/2020).

[67] Etienne Cheynet, Jasna Bogunović Jakobsen, and Charlotte Obhrai. Spectral characteristics of surface-layer turbulence in the north sea. *Energy Procedia*, 137:414 – 427, 2017. 14th Deep Sea Offshore Wind RD Conference, EERA DeepWind'2017.

[68] Beaufort wind force scale. URL : https://www.metoffice.gov.uk/weather/guides/coast-and-sea/beaufort-scale (accessed: 19/05/2020).

[69] International Electrotechnical Commision (IEC) 2009. *Wind turbines — Part 3: Design requirements for fixed offshore wind turbines*. Tech. Rep. IEC61400-3.

[70] Klaus Hasselmann, T. Barnett, E. Bouws, H. Carlson, D. Cartwright, K Enke, J Ewing, H Gienapp, D. Hasselmann, P. Kruseman, A Meerburg, Peter Muller, Dirk Olbers, K Richter, W. Sell, and H. Walden. Measurements of wind-wave growth and swell decay during the joint north sea wave project (jonswap). *Deut. Hydrogr. Z.*, 8:1–95, 01 1973.

[71] Joint north sea wave observation project. https://www.codecogs.com/library/engineering/fluid_mechanics/waves/spectra/jonswap.php (accessed: 30/03/2020).

[72] Pim van der Male. *OE44135 Offshore Wind Support Structures*, 2019.

[73] Alexander Boukhanovsky, Leonid Lopatoukhin, and Carlos Guedes Soares. Spectral wave climate of the north sea. *Applied Ocean Research*, 29:146–154, 07 2007.

[74] E. Machefaux et al. *Single Wake Meandering, Advection and Expansion - An analysis using an adapted Pulsed Lidar and CFD LES-ACL simulations*. DTU, 2013.

[75] Jonkman J.M. *FAST.Farm User's Guide and Theory Manual*. Tech. Rep. NREL/TP-xxxx-xxxxx, National Renewable Energy Laboratory.

[76] L.J. Vermeer, J.N. Sørensen, and A. Crespo. Wind turbine wake aerodynamics. *Progress in Aerospace Sciences*, 39(6):467 – 510, 2003.

[77] Hui Hu, Zifeng Yang, and P. Sarkar. Dynamic wind loads and wake characteristics of a wind turbine model in an atmospheric boundary layer wind. *Experiments in Fluids*, 52, 05 2011.

[78] L. J. Clancy. *Aerodynamics, section 5.14*. Pearson higher education, 1986.

[79] L. J. Clancy. *Aerodynamics, section 5.17 and 8.9*. Pearson higher education, 1986.

[80] E. A. Bossanyi. 1983. SERI/TR-635–1280, Solar Energy Research Institute, Golden, Colorado.

[81] David Sharpe Ervin Bossanyi Tony Burton, Nick Jenkins. *Wind Energy Handbook, Second Edition, section 2.10*. John Wiley Sons, 2011. ISBN: 978-0-470-69975-1.

[82] J. Berg et al. *Micro meteorology for Wind Energy*. DTU, October 2017.

[83] Donelan Mark Young Ian. *On the determination of global ocean wind and wave climate from satellite observations*. 2018. Remote Sensing of Environment. 215. pp. 228-241. 10.1016/j.rse.2018.06.006.

[84] Rolf-Erik Keck, Martin de Maré, Matthew J. Churchfield, Sang Lee, Gunner Larsen, and Helge Aagaard Madsen. Two improvements to the dynamic wake meandering model: including the effects of atmospheric shear on wake turbulence and incorporating turbulence build-up in a row of wind turbines. *Wind Energy*, 18(1):111–132, 2015.

[85] B.L. Ennis, C.L. Kelley, and D.C. Maniaci. Dynamic wake meandering model comparison with varying fidelity models for wind turbine wake prediction. 4:2885–2894, 01 2015.

[86] Massachusetts Institute of Technology. Thin shear layer approximation. URL : `http://web.mit.edu/16.110/www/tsl_equations.html` (accessed: 28/04/2020).

[87] Mann 64bit turbulence generator. URL : `http://www.hawc2.dk/Download/Pre-processing-tools/Mann-64bit-turbulence-generator` (accessed: 19/02/2020).

[88] Betz & Albert & Grissmer & David W. (David Waltz). *Introduction to the theory of flow machines*. Pergamon Press, 1966.

[89] Erin Bachynski. Basic aerodynamics for wind turbines, September 2019.

[90] Betz Prandtl. *Vier Abhandlungen zur Hydrodynamik und Aerodynamik*. 1927. `https://doi.org/10.1002/zamm.19280080126`.

[91] David Sharpe Ervin Bossanyi Tony Burton, Nick Jenkins. *Wind Energy Handbook, Second Edition, section 3.8.3 - 3.8.6*. John Wiley Sons, 2011. ISBN: 978-0-470-69975-1.

[92] David Sharpe Ervin Bossanyi Tony Burton, Nick Jenkins. *Wind Energy Handbook, Second Edition, Figure 4.2*. John Wiley Sons, 2011. ISBN: 978-0-470-69975-1.

[93] David Sharpe Ervin Bossanyi Tony Burton, Nick Jenkins. *Wind Energy Handbook, Second Edition, Figure 4.3*. John Wiley Sons, 2011. ISBN: 978-0-470-69975-1.

[94] Peters. D.A. Pitt D.M. *Theoretical Prediction of Dynamic Inflow Derivatives*. John Wiley Sons, 1981. Vertica, **5**, 21-34.

[95] Jonkman JM, S. Butterfield, W. Musial, and G. Scott. Definition of a 5mw reference wind turbine for offshore system development. *National Renewable Energy Laboratory (NREL)*, 01 2009.

[96] *FLORIS*. URL : `https://github.com/nrel/floris` (accessed: 18/04/2020).

[97] *WindFarmer*. `www.dnvgl.com/services/wind-resource-assessment-software-win` (accessed: 18/04/2020).

[98] P.M.O. Gebraad. *Data-Driven Wind Plant Control, figure 2.4*. PhD thesis, TU Delft, 2014.

[99] Biadgo Mulugeta and Aynekulu Gerawork. Aerodynamic design of horizontal axis wind turbine blades. *FME Transaction*, 45:647–660, 01 2017.

[100] P.M.O. Gebraad. *Data-Driven Wind Plant Control, chapter 2.3*. PhD thesis, TU Delft, 2014.

[101] F. (Author) & Bitsche R. (Author) & Kim T. (Author) & Yde A. (Author) & Henriksen L. C. (Author) & ... Natarajan A. (Author). Bak, C. (Author) & Zahle. *The DTU 10-MW Reference Wind Turbine*. Sound/Visual production (digital), June 2013.

[102] P.K. Chaviaropoulos. *Similarity rules for wind turbine up-scalingl*. Online Documentation, 2006.

[103] Kolja Müller, Ricardo Faerron Guzmán, Po Wen Cheng, Josean Galván, M. J. Sanchez, Raúl Rodríguez, and Andreas Manjock. Load sensitivity analysis for a floating wind turbine on a steel semi-submersible substructure. 2018. Figure 1.

[104] Antonio Pegalajar-Jurado, Henrik Bredmose, Michael Borg, Jonas G. Straume, Trond Landbø, Håkon S. Andersen, Wei Yu, Kolja Müller, and Frank Lemmer. State-of-the-art model for the LIFES50 OO-star wind floater semi 10mw floating wind turbine. *Journal of Physics: Conference Series*, 1104:012024, oct 2018.

[105] Yu W & Muller K & Lemmer F. *LIFES50+ D4.2: Public definition of the two LIFES50+ 10MW floater concepts*. concepts Tech. rep. University of Stuttgart, 2018.

[106] Josean Galvan, M Sánchez-Lara, Iñigo Mendikoa, G Pérez-Morán, Vincenzo Nava, and Raul Rodriguez Arias. Nautilus-dtu10 mw floating offshore wind turbine at gulf of maine: Public numerical models of an actively ballasted semisubmersible. *Journal of Physics: Conference Series*, 1102:012015, 10 2018.

[107] Matthew Hall. *MoorDyn*. Matt Hall, 2017. `http://www.matt-hall.ca/moordyn.html` (accessed: 21/02/2020).

[108] J. R. Morison & M. P. O'Brien & J. W. Johnson & S. A. Schaaf. *The force exerted by surface waves on piles*. 1950.

[109] Example of application of morrison equation. URL : homepages.ucl.ac.uk/~uceseug/Fluids2/Wind_Turbines/Morrison_Example.pdf (accessed: 20/01/2020).

[110] Adam S. Wise and Erin E. Bachynski. Wake meandering effects on floating wind turbines. *Wind Energy*, 23(5):1266–1285, 2020.

[111] C. Lee & J. Newman, 2016. https://www.wamit.com (accessed: 18/04/2020).

[112] Galvan et al. *Definition and analysis of NAUTILUSDTU10 MW floating offshore wind turbine at Gulf of Maine, experiments at Sintef Ocean and Polimi*. 2018. Tecnalia RI, Derio, Basque Country, Spain.

[113] T J Larsen & T D Hanson. *A method to avoid negative damped low frequent tower vibrations for a floating, pitch controlled wind turbine*. J. Phys.: Conf. Ser. 75 012073, 2007.

[114] Jonkman B J Jonkman J M, Hayman G J and Damiani R R. *AeroDyn v15 User's Guide and Theory Manual*. Techn. Rep. NREL/TP-xxxx-xxxxx, National Renewable Energy Laboratory.

[115] Amir Nejad. Wind turbine drivetrains, October 2019.

[116] Wichtert Kooloos. Limiting mechanisms for the torque density of wind turbine drivetrains. Master's thesis, NTNU, 2019.

[117] S. Faulstich, Berthold Hahn, and P.J. Tavner. Wind turbine downtime and its importance for offshore deployment. *Wind Energy*, 14, 04 2011.

[118] Klinger Friedrich and Müller Lukas. State-of-the-art and new technologies of direct drive wind turbines. In Tanay Sidki Uyar, editor, *Towards 100% Renewable Energy*, pages 33–50, Cham, 2017. Springer International Publishing.

[119] J.D. Sørensen and J.N. Sørensen. *Wind energy systems: Optimising design and construction for safe and reliable operation*. 12 2010.

[120] Sebastian Schreier. *OE44100 Floating Structures Offshore Mooring*. TU Delft, 2019.

[121] Cuong Dao, Behzad Kazemtabrizi, and Christopher Crabtree. Wind turbine reliability data review and impacts on levelised cost of energy. *Wind Energy*, 22(12):1848–1871, 2019.

[122] K. Fischer, F. Besnard, and L. Bertling. Reliability-centered maintenance for wind turbines based on statistical analysis and practical experience. *IEEE Transactions on Energy Conversion*, 27(1):184–195, March 2012.

[123] Joel Igba, Kazem Alemzadeh, Keld Henningsen, and Christopher Durugbo. Effect of preventive maintenance intervals on reliability and maintenance costs of wind turbine gearboxes. *Wind Energy*, 18(11):2013–2024, 2015.

[124] Iain Dinwoodie, Ole-Erik V. Endrerud, Matthias Hofmann, Rebecca Martin, and Iver Bakken Sperstad. Reference cases for verification of operation and maintenance simulation models for offshore wind farms. *Wind Engineering*, 39(1):1–14, 2015.

[125] G. Lundberg, A. Palmgren, and A. Palmgren. *Dynamic Capacity of Rolling Bearings*. (Acta polytechnica). Generalstabens Litografiska Anstalts Förl., 1947.

[126] Amir R. Nejad, Zhen Gao, and Torgeir Moan. Fatigue reliability-based inspection and maintenance planning of gearbox components in wind turbine drivetrains. *Energy Procedia*, 53:248–257, 12 2014.

[127] International Organization for Standardization (ISO). *Rolling bearings — Dynamic load ratings and rating life*. ISO281:2007 https://www.iso.org/ics/21.100.20/x/.

[128] International Electrotechnical Commision (IEC) 2012. *Wind turbines — Part 4: Design requirements for wind turbine gearboxes*. Tech. Rep. IEC61400-4.

[129] Dalhoff P Grzybowski R Niederstucke B, Anders A. Load data analysis for windturbine gearboxes. in "Final Report, ELA – Enhanced Life Analysis of WindPower Systems, 2003". Germanischer Lloyd Wind Energie GmbH.

[130] I. Rychlik. A new definition of the rainflow cycle counting method. *International Journal of Fatigue*, 9(2):119 – 121, 1987.

[131] Amir R. Nejad and Torgeir Moan. On model-based system approach for health monitoring of drivetrains in floating wind turbines. *Procedia Engineering*, 199:2202 – 2207, 2017. X International Conference on Structural Dynamics, EURODYN 2017.

[132] International Organization for Standardization (ISO). *Mechanical vibration - measurement and evaluation of machine vibration - part 1: general guidlines*. ISO 20816–1, 2016 https://www.iso.org/standard/63180.html.

[133] Joel Igba, Kazem Alemzadeh, C.M Durugbo, and Egill Eiriksson. Analysing rms and peak values of vibration signals for condition monitoring of wind turbine gearboxes. *Renewable Energy*, 91, 06 2016.

[134] International Organization for Standardization (ISO). *Mechanical vibration - evaluation of machine vibration by measurements on non-rotating parts - horizontal axis wind turbines with gearbox*.

[135] Kelly M. Chougule A., Mann J. Simplification and validation of a spectral-tensor model for turbulence including atmospheric stability. *Boundary-Layer Meteorol*, 167:371–397, 2018.

[136] Pierre-Elouan Réthoré, Peter Fuglsang, Gunner Chr. Larsen, Thomas Buhl, Torben J. Larsen, and Helge Aagaard Madsen. Topfarm: Multi-fidelity optimization of wind farms. *Wind Energy*, 17(12):1797–1816, 2014.

[137] Jennifer Annoni Paula Doubrawa and Jason Jonkman. Optimization-based calibration of fast.farm parameters against sowfa. *NREL*.

[138] J Jonkman, P Doubrawa, N Hamilton, J Annoni, and P Fleming. Validation of FAST.farm against large-eddy simulations. *Journal of Physics: Conference Series*, 1037:062005, jun 2018.

[139] Dynamometer research facilities. URL : https://www.nrel.gov/wind/facilities-dynamometer.html (accessed: 19/05/2020).

[140] Meherwan P. Boyce. *Gas Turbine Engineering Handbook (Fourth Edition)*. 2012. `://www.sciencedirect.com/topics/engineering/campbell-diagram` (accessed: 27/05/2020).

[141] K. Shaler, J. Jonkman, and N. Hamilton. Effects of inflow spatiotemporal discretization on wake meandering and turbine structural response using FAST.farm. *Journal of Physics: Conference Series*, 1256:012023, jul 2019.

[142] P.M.O. Gebraad. *Data-Driven Wind Plant Control, chapter 2.4*. PhD thesis, TU Delft, 2014.

[143] Det Norkse Veritas. *Recommended Practice DNV-RP-C205*. URL `https://rules.dnvgl.com/docs/pdf/dnv/codes/docs/2010-10/rp-c205.pdf`.

[144] Frode Vikebø, Tore Furevik, Gunnar Furnes, Nils Kvamstø, and Magnar Reistad. Wave height variations in the north sea and on the norwegian continental shelf, 1881–1999. *Continental Shelf Research - CONT SHELF RES*, 23:251–263, 02 2003.

[145] Amir R. Nejad, Erin Bachynski, Zhen Gao, and Torgeir Moan. Fatigue damage comparison of mechanical components in a land-based and a spar floating wind turbine. *Procedia Engineering*, 101, 12 2015.

A | Appendix A

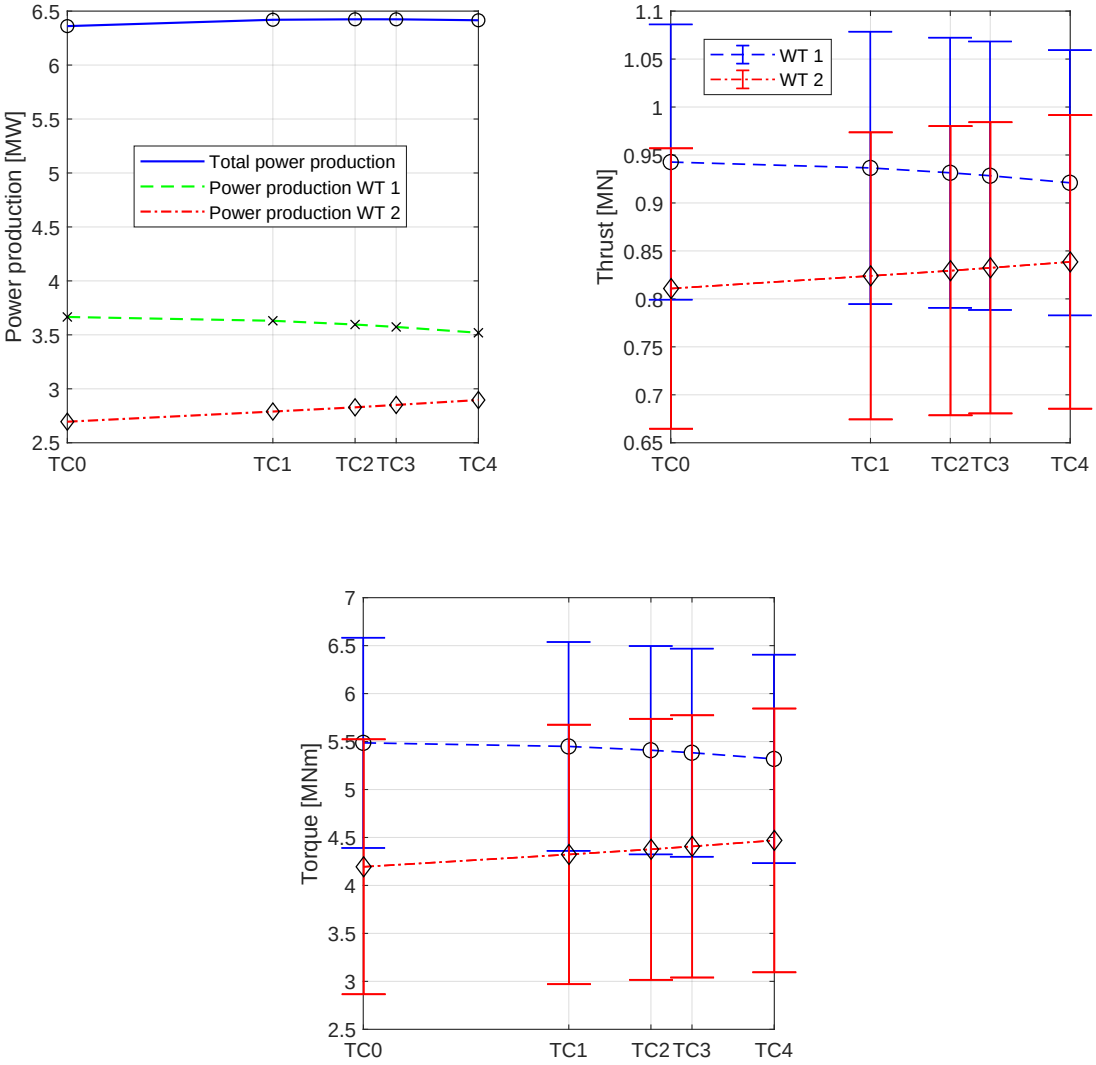

Figure A.1: Fixed: Power production of WT_1 and WT_2 and total power production (top left) and the mean (μ) and standard deviation (σ) results of the thrust, F_x, (top right) and rotor torque, M_x(bottom) for $TC_0 - TC_4$.

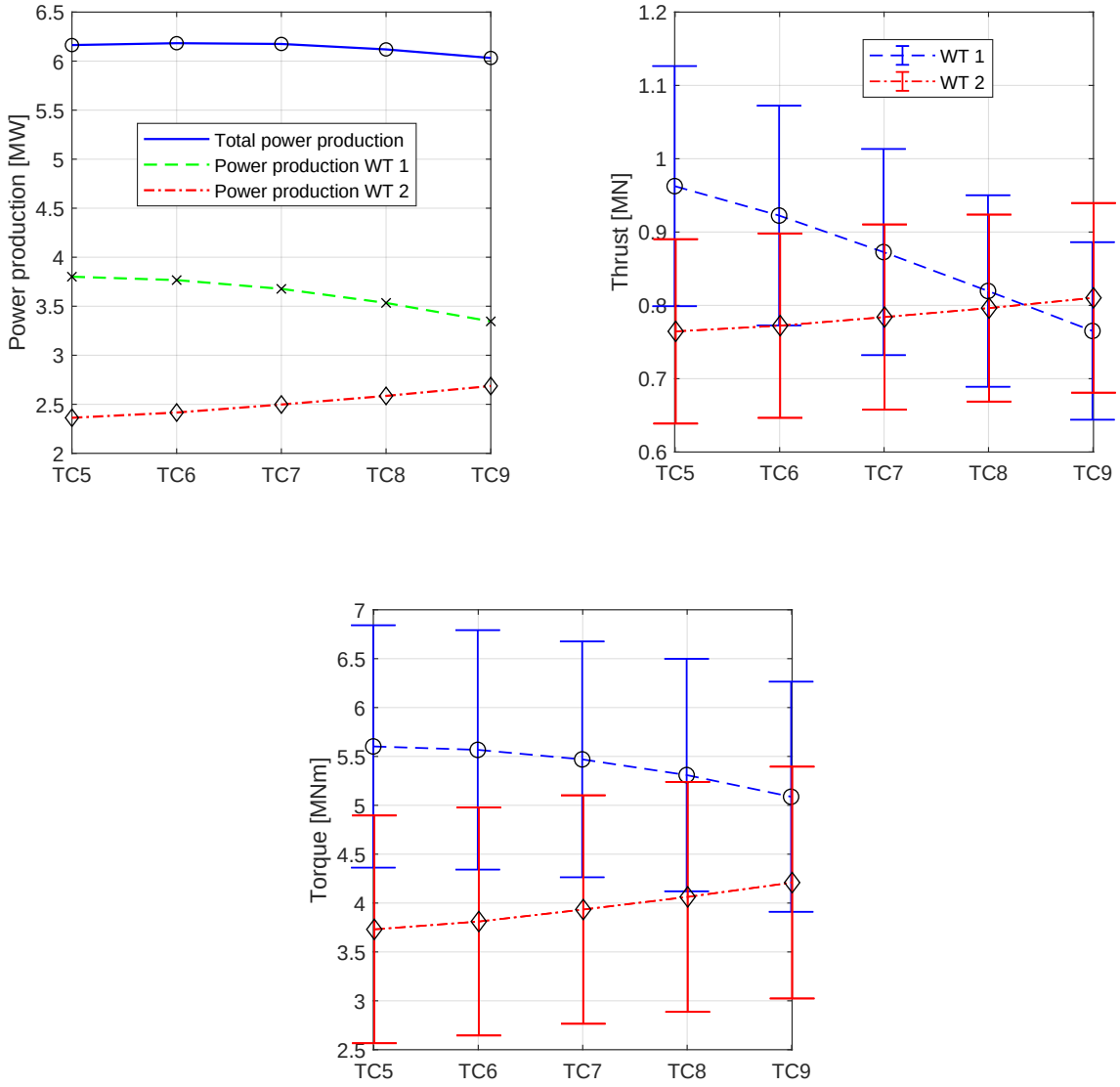

Figure A.2: Fixed: Power production of WT_1 and WT_2 and total power production (top left) and the mean (μ) and standard deviation (σ) results of the thrust, F_x, (top right) and rotor torque, M_x(bottom) for $TC_5 - TC_9$.

B | Appendix B

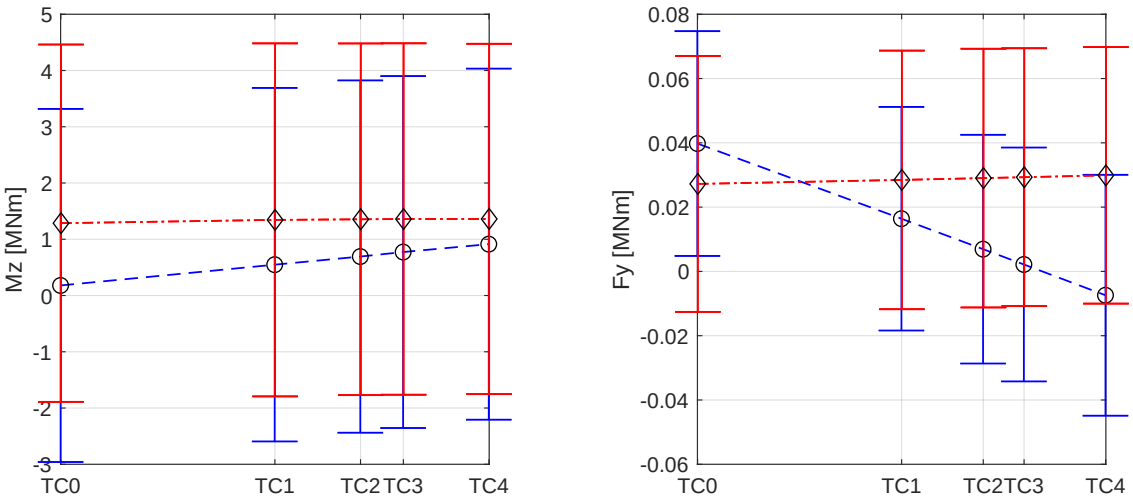

Figure B.1: Mean (μ) and standard deviation (σ) of M_z and F_y at the yaw bearing acting on the tower for $TC_0 - TC_4$.

C | Appendix C

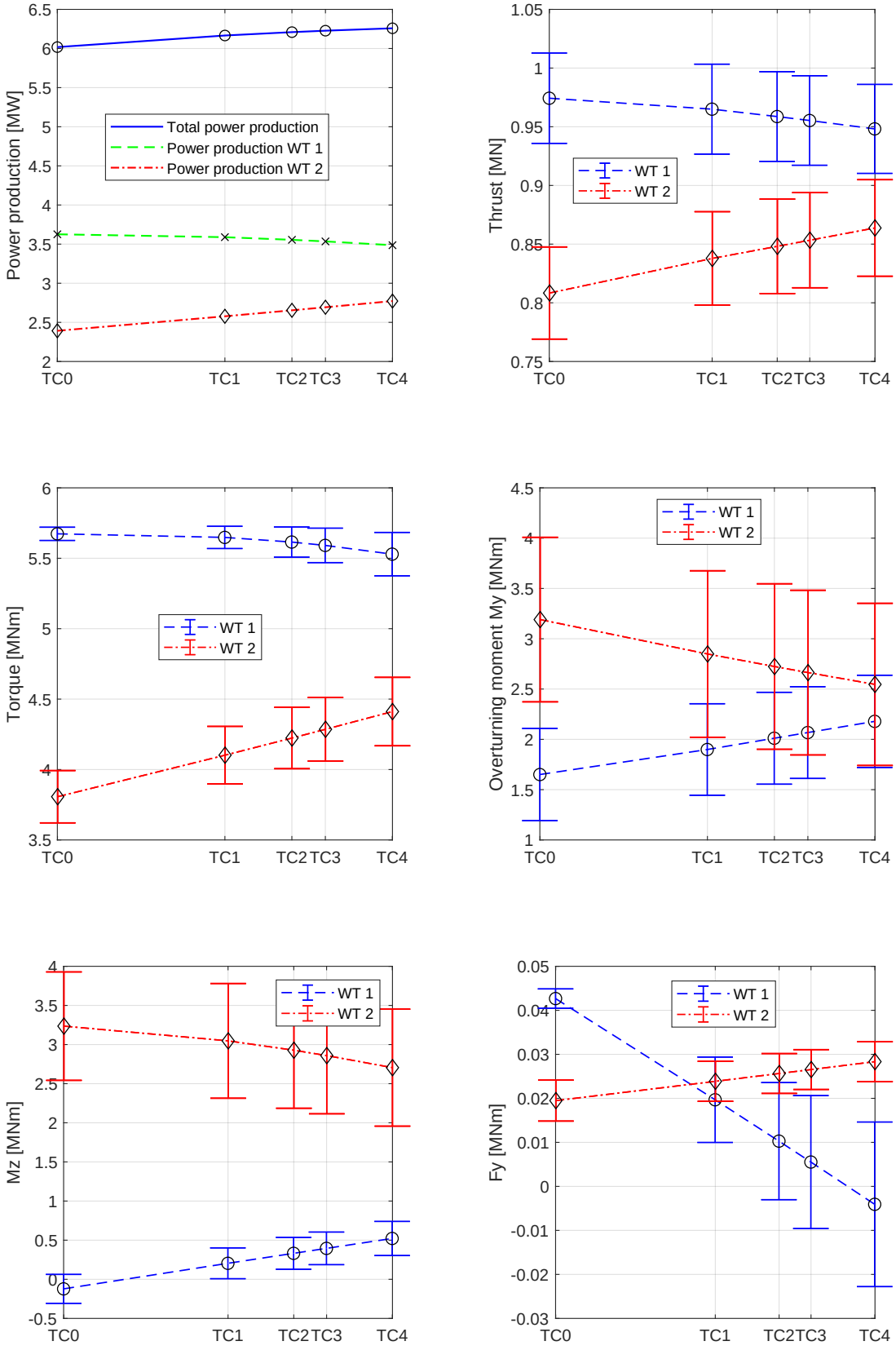

Figure C.1: Uniform wind field: Power production of WT_1 and WT_2 and total power production (top left) and the mean (μ) and standard deviation (σ) results of the thrust, F_x, (top right), rotor torque, M_x, (left), overturning moment at the yaw bearing acting on the nacelle, M_y, (right), M_z acting on the tower (bottom left) and F_y (bottom right) for $TC_0 - TC_4$.

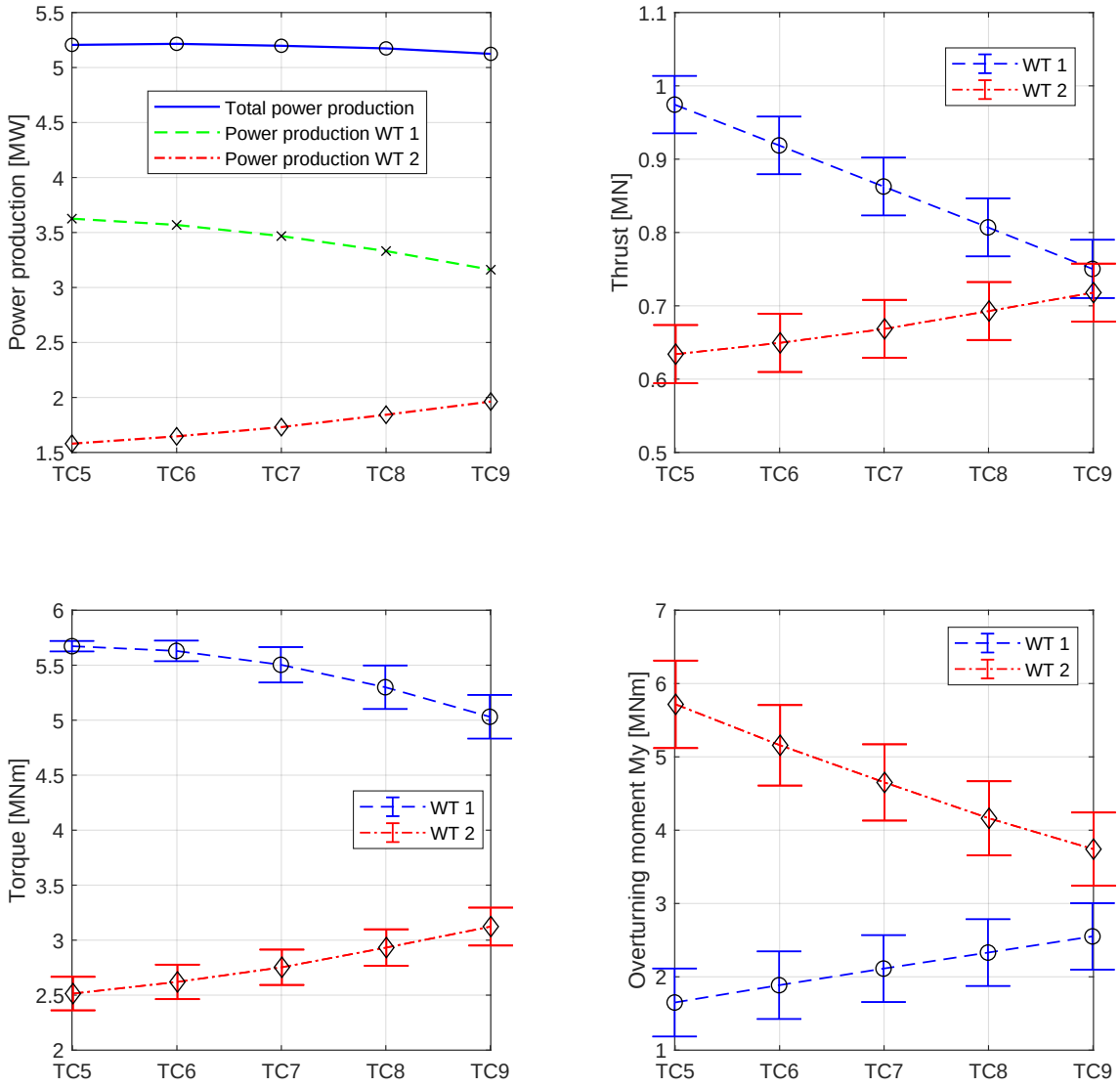

Figure C.2: Uniform wind field: Power production of WT_1 and WT_2 and total power production (top left) and the mean (μ) and standard deviation (σ) results of the thrust, F_x, (top right), rotor torque, M_x, (bottom left) and overturning moment at the yaw bearing, M_y, (bottom left) for $TC_5 - TC_9$. M_y acts on the WT nacelle.